Scanning near-field optical microscopy with new probes and feedback modes

Thèse N° 9504

Présentée le 6 juin 2019

à la Faculté des sciences de base
Laboratoire de physique de la matière vivante
Programme doctoral en physique

pour l'obtention du grade de Docteur ès Sciences

par

Anton SMIRNOV

Acceptée sur proposition du jury

Prof. F. Courbin, président du jury
Prof. G. Dietler, Dr. S. Sekatski, directeurs de thèse
Prof. S. Popov, rapporteur
Prof. A. Zayats, rapporteur
Prof. O. Martin, rapporteur

2019

ÉCOLE POLYTECHNIQUE
FÉDÉRALE DE LAUSANNE

Scanning near-field optical microscopy with new probes and feedback modes

Abstract

Scanning near-field optical microscope (SNOM) technique enables to overcome Abbe diffraction limit of far-field optics as well as to obtain simultaneously optical and topographical images. While the optical resolution of the method is limited by the aperture size and is typically $50-100nm$, an excellent spatial resolution in a topography channel, quite comparable with atomic force microscope (AFM), can be realized. Naturally, we need a convenient and precise method to control the distance between the tip and sample for the successful operation of any SNOM device. Nowadays, by far the most popular method of the SNOM tip-sample distance control is the shear force – based feedback employing a glass fiber attached to the quartz tuning fork (TF). However, the shear-force distance control method is far from the ideal one. The crosstalk between optical and topographical image can warp the results. The forces between the tip and sample are high and in many cases might be destructive. We report the realization of a new approach to the problem: bent sharpened glass optical

fibers with carefully controlled sizes of the bent part and the radius of the curvature of the bending were prepared and experimentally exploited as SNOM probes. Detailed analysis of fiber vibration modes shows that realization of truly tapping mode of the probe dithering requires extreme caution. In case of using the second resonance mode, simply "bent", or "curved", probes vibrate mostly in the shear-force mode unless the bending radius is rather small ($\sim\ 0.3mm$) and the probe's tip is short. The probes having these characteristics were prepared and attached to the TF in the double resonance conditions, which enables to achieve a significant quality factor of the sensor.

Another common problem of most aperture SNOMs is the fragility of the tip. We proposed and realized the use of different plastic fibers to solve this problem. These fibers look very promising for the use as SNOM probes, and are characterized by much less fragility (compare glass and plastic) and greater ease of the tip preparation. For such preparation, hazardous treating with hydrofluoric acid, which remains the most popular approach to prepare SNOM probes from the glass fibers, can be entirely avoided.

Fluorescence resonance energy transfer (FRET) is one of the most promising ways to improve the spatial resolution of the SNOM, and the main part of the Thesis is devoted to the elaboration of FRET SNOM. The idea is to use a donor (acceptor) nanoparticle/molecule as local fluorescence center attached to the tip and measure the fluorescence induced by it in the sample (or vice versa) due to the FRET. Ca. ten years ago, this idea has been realized at the single molecule level with $CdSe$ nanocrystals

and appropriate dye molecules. Despite the high spatial resolution (better than $20nm$) attained in this experiment, it remains an isolated one, and this is for a valid reason: albeit rather large, the photostability of dye molecules and semiconductor nanocrystals still enables to use a single fluorescence center exploiting for imaging only a few minutes at best. Fluorescent centers with high photostability should be used to overcome this problem. Earlier, claimed to be very photostable and bright nitrogen-vacancy (NV) color centers in nano-diamond (ND) crystals were proposed, and the corresponding researches started in LPMV EPFL almost ten years ago. In the Thesis at hand, we finalize this work showing that such system is not suitable to realize single fluorescent center FRET SNOM method. We propose to use certain rare-earth ions in crystals to achive the goal, in particular $LuBO_3 : (Tb)$ micro- and nanocrystals.

Keywords: SNOM, FRET, NV, ND, POF, PC, LRSPP, scanning near-field optical microscopy, fluorescence resonance energy transfer, tapping mode, plastic optical fibers, bent fibers, double resonance, photonic crystal, long-range surface plasmon-polaritons, silver nanofilm.

Scanning near-field optical microscopy with new probes and feedback modes

RÉSUMÉ

La technique SNOM est capable de dépasser la limite de diffraction d'Abbe ainsi que d'obtenir simultanément des images optiques et topographiques. Bien que la résolution optique de la méthode est limitée par la taille de l'ouverture (compris entre 50 et $100nm$, une bonne résolution spatiale est obtenue en topographie, comparable à celle obtenue avec l'AFM. La distance entre la point et l'échantillon doit être contrôlée de manière précise lors de l'utilisation d'un appareil SNOM. De nos jours, la technique la plus souvent utilisée pour contrôler la distance entre la pointe de SNOM et l'échantillon est le feedback lié à la force de cisaillement en utilisant une fibre de verre connectée a un diapason en quartz. Cependant, la méthode de contrôle par force de cisaillement est loin d'être la meilleure. Les interférences entre image optique et topographique peuvent déformer les résultats. Les forces entre l'échantillon et la pointe sont forte et peuvent être facilement destructrices. Nous reportons une nouvelle approche pour résoudre ce problème : les fibres optiques en verre pointues et incurvées/pliées, avec un contrôle

précis de la taille ainsi que du rayon de courbure du pli, ont été préparées et testées en tant que sondes pour SNOM. Des analyses détaillées du mode de vibration de la fibre montrent que la réalisation en mode intermittent du tremblotement de la sonde nécessite une grande précaution. Dans le cas où le second mode de résonnance est utilisé, les sondes simplement «pliées» ou «incurvées» vibrent principalement en mode force de cisaillement à moins que le rayon de courbure soit petit ($0.3mm$) et que la pointe de la sonde soit courte. Les sondes possédant ces caractéristiques ont été préparées et attachées au TF dans des conditions de double résonnances ce qui permet d'obtenir un facteur de qualité du capteur significatif.

Un autre problème fréquent chez la plupart des sondes de SNOM est la fragilité de la pointe. Nous proposons l'utilisation de fibre en plastique pour résoudre ce problème. Ces fibres semblent très prometteuses en tant que sonde pour SNOM car elles sont moins fragiles et plus simples à préparer. En effet la préparation des fibres optiques en verre requiert l'utilisation d'acide hydrofluorique, qui est extrêmement dangereux à utiliser, et cela peut être éviter en remplaçant la fibre en verre par une en plastique.

FRET est une des techniques qui pourrait indure la compatibilité entre les données optiques et topographiques. Le principe est d'utiliser une molécule ou nanoparticule comme centre de fluorescence, (donneuse/accepteuse), attachée à la pointe et de mesurer la fluorescence induite par ces molécules dans l'échantillon ou vice versa. Cette méthode a été réalisée au stade molécule unique avec des nanocristaux de $CdSe$ et des colorants fluorescents appropriés. Malgré la bonne résolution spatiale

obtenue lors de cette expérience (supérieure à $20nm$), cela reste un cas isolé pour une raison: bien que large, la photostabilité des molécules fluorescentes et des nanocristaux semi-conducteurs permet l'utilisation d'un fluorochrome unique pendant quelques minutes uniquement. Les centres fluorescents à haute photostabilité devraient être utilisés pour résoudre ce problème. Auparavant, des centres de couleurs NV prétendument très photostables et brillants dans des cristaux de nanodiamants avaient été proposés, et les recherches correspondantes ont commencé à LPMV EPFL il y a près de dix ans. Dans la Thèse à l'étude, nous finalisons ce travail en montrant qu'un tel système n'est pas adapté à la réalisation de la méthode FRET SNOM à centre fluorescent unique. Nous proposons deux solutions : l'excitation alternative des centres d'azote vacant dans les nanodiamants et l'utilisation de nanocristaux composés de $LuBO_3$: (Tb).

Mots-clés: MOCP, SNOM, FRET, NV, ND, POF, PC, LRSPP, le microscope optique en champ proche, le transfert d'énergie entre molécules fluorescentes, le mode tapping, le fibres pliées, fibre optique plastique, double résonnances, cristaux photoniques, plasmon-polariton de surface longue-portée, nanofilm d'argent.

Acknowledgments

It is nearly impossible to express all my gratitude to the people who support me during my PhD.

First and foremost, I would like to thank Sergey, for tremendous social support and being ”godfather” in science. Always feeling his relief I was never afraid of the future. I learned a lot from him about the academic environment.

I am also very grateful to Giovanni. He was always supportive and ready to help. I gained a lot from our discussions, regardless of the topic. What is more critical, he created a charming and warm atmosphere in the group.

During the work, I have spent a wonderful time with my friends and colleagues. I acknowledge Katya, who helped me a lot in the beggining. I thank all the past and present members of our group: Petar, Wojciech, Jiangtao, Zeno, Anne, Kamilla, Anton M., Leonardo, Philippe, Ula, Raphael, Ines, Sandro, Carine, Caroline.

Many thanks to Michel, Aubry, Florent, Christine and Mireille. They made my life much, and with their help, I never had any computer or administrative problem.

I appreciate the support coming from my friends Gulnaz, Nastya and Dasha here in Lausanne.

And the special thanks goes to my eternal friends Tanya and Vladimir for their infinite patience and answering of my countless questions.

Needless to say, thanks to my family for their constant support.

Contents

Listing of figures

Abbreviations

a-SNOM	apertured scanning near-Field optical microscope.
AFM	atomic force microscope.
CCD	charge-coupled device.
CVD	chemical vapor deposition.
CW	continuous wave.
DCM	dichlormethane.
EA	ethyl acetate.
FRET	fluorescence resonance energy transfer.
IR	infrared.
IRF	instrument response function.
LRSPP	long-range surface plasmon polaritons.
MF	multi-frequency.
ND	nano-diamond.
NV	nitrogen-vacancy.

PALM	photo activated localization microscopy.
PC	photonic crystal.
PMMA	poly(methyl methacrylate).
POF	plastic optical fiber.
PSD	position-sensitive diode.
s-SNOM	scattering scanning near-field optical microscope.
SEM	scanning electron microscope.
SNOM	scanning near-field optical microscope.
SPP	surface plasmon polaritons.
STED	stimulated emission depletion microscopy.
STM	scanning tunneling microscope.
STORM	stochastic optical reconstruction microscopy.
TF	tuning fork.
UV	ultraviolet.

0

Introduction

Light or in general electromagnetic radiation is probably the best information carrier known of today. As a result, on the par with nanoelectronics, nano-optics has emerged. Naturally, it requires the existence of proper tools and techniques to support this evolution and SNOM is definitely one of such tools.

0.1 HISTORICAL OVERVIEW

A human eye can distinguish objects down to $200\mu m$ in average. However, magnification systems can help to see more. Naturally, people were always looking for a way to do it.

More than 3 thousand years ago ancient scientists developed first microscopes. It was primitive bead-like magnifiers which could provide magnification ten times roughly. The situation lasted until $XVII$ century when Antoni van Leeuwenhoek ($1632 - 1723$) designed a lens with very high magnifying power - 500 times. It was very tiny lenses which allowed to see bacteria for the first time. Meanwhile, the astronomer Galileo ($1564 - 1642$) announced his two-lens microscope. These inventions led to the genesis of modern microscopes which now have a practical limit of magnification around 2500 times.

Alike all optical systems confining beams of light, the microscope has a limit of resolution due to diffraction. Back in 1873, Ernst Abbe figured out that light with wavelength λ, traveling in a medium with refractive index n and converging to a spot with half-angle θ will have a minimum resolvable distance:

$$d = \frac{\lambda}{2nsin\theta}. \tag{0.1.1}$$

Thus the Abbe limit is $d \approx \frac{\lambda}{3}$ for modern optics

However, super-resolution techniques can surpass such a limit using fluorescent dyes. In 1994, Stefan W. Hell and Jan Wichmann developed stimulated emission depletion microscopy (STED); capable of overcoming the diffraction barrier using non-linear characteristics of the fluorescence with two-step excitation [1]. The idea itself was patented in 1986 by V.A. Okhonin [2], however Hell was not aware of this judging from the lack of the reference. STED microscopy allows reaching of a $10nm$ lateral resolution. However, such an approach requires an expensive, sophisticated setup. At the same time, photo activated localization microscopy (PALM) [3, 4] and stochastic optical reconstruction microscopy (STORM) [5] utilizing sequential stochastic fluorophores activation can be realized via commercially available microscope capable of single molecule image registration. The central principle behind these methods is stochastic photoswitching, where most of the molecules are in the dark state. The low-intensity excitation light activates a small fraction of molecules, which are bleaching after their localization.

All far-field techniques have their advantages and drawbacks but only SNOM can give excellent resolution and link topography with optical features.

The first ever published idea of near-field imaging [6] arise from the discussion between Synge and Einstein and proposes a concept of an apparatus which is very close to modern SNOMs. Synge suggested putting a very bright light source behind a metal screen with a tiny pinhole (order of $100nm$) and a sample in front of the screen at a distance comparable with pinhole size. In such a system the image of a sample should be obtained via scanning of the sample. In the end, Synge was ahead of his time with his idea.

The next serious attempt to realize near-field imaging was undertaken in 1972 by Ash and Nichols [7]. They demonstrated sub-wavelength imaging capabilities in the microwave range. They succeeded to achieve $\frac{\lambda}{60}$ resolution in one dimension.

Synge's idea was finally realized starting from 1984 by two groups independently: Lewis, Isaacson, Harootunian, and Betzig from Cornell University [8] with $\lambda/16$ resolution and Pohl, Denk, and Lanz [9] from IBM (Rüschlikon, Switzerland) with

$\lambda/20$ resolution. As a result, nowadays, we have advanced SNOM exploiting very sharp light sources ($R << \lambda$) kept close to the sample ($d << \lambda$) using AFM, scanning tunneling microscope (STM) techniques.

Combining the distance control method from AFM/STM with the optical channel, a resolution up to $30nm$ could be reached for such a microscope: this fits somewhat in between AFM and classical optical microscope. In this case, the size of the light source limits the resolution. Attempts to increase the resolution more than $30nm$ by decreasing the size of an aperture are not practical due to a strong dependence of the light intensity coming through the hole on the aperture size.

0.2 CLASSICAL OPTICAL MICROSCOPY

At the end of the $XVII$ century, Ernst Abbe found that the resolution of an optical microscope is strongly dependent on its aperture. In several experiments with the objects having a periodic structure, he showed that this aperture factor is due to the diffraction of light.

According to Abbe's theory, even the most perfect lens build the image with a certain error. Since any lens has a finite aperture, it can collect a limited amount of spatial frequencies from the object's light field. Light beams corresponding to high spatial frequencies do not participate in the formation of the image. Thus, an image formed by a lens cannot be a copy of the object, because of these missing tiny structure features.

Ultimately, the studied object can be expressed as a collection of point sources, where each point source is imaged as an Airy disc ("circle of confusion," an optical spot caused by a cone of light rays from a lens not coming to a perfect point focus when imaging a point source). The image of the object will be an overlay of such discs. In case of a microscope, the Airy disc in the image plane have a radius equal to $1.22\lambda L/D$ and is formed on a relatively large distance L by an objective with a diameter D. Thus, according to the Rayleigh criterion, a microscope can resolve two neighboring points separated by a distance l if a span between their Airy discs l' is larger than the diffraction spot radius:

$$l' \geqslant 1.22\frac{\lambda L}{D} = 0.61\frac{\lambda}{u'}. \tag{0.2.1}$$

Where $2u' = \frac{D}{2L}$ is an aperture angle from the image side and the formula is valid for a circular aperture.

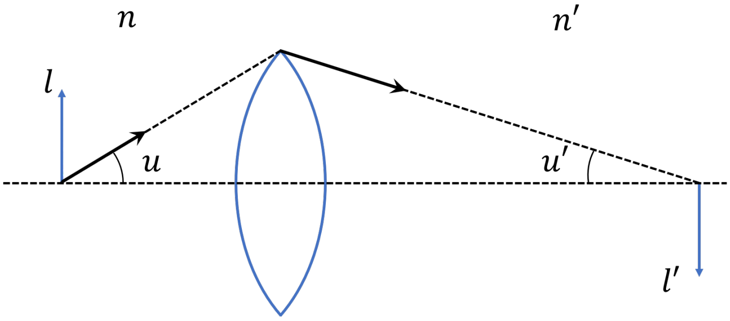

Figure 1: To the illustration of Abbe sine condition

We can go to the linear size of the object itself using Abbe sine condition which is correct for any microscope objective. Thus, when the u' is small, the condition can be written as $l \cdot n \cdot sinu = l' \cdot n' \cdot sinu' = n' \cdot l' \cdot u'$, where $2u$ is an aperture angle from the side of the object. Therefore, we have:

$$l \geqslant 0.61\frac{\lambda}{n \cdot sinu} = 0.61\frac{\lambda}{NA} = l_{min}. \tag{0.2.2}$$

NA here is a numerical aperture, which is equal to $1.4 - 1.6$ for good micro-objectives. Thus, diffraction is the limiting factor for the microscope resolution.

However, in theory, there is no limitation to get more detailed information about the object structure. The near-field techniques can circumvent these limitations.

We know[10] that in $2D$ model complex amplitude of a plane monochromatic wave is:

$$f(\overrightarrow{r}) = a_0 e^{i(\overrightarrow{k}\overrightarrow{r}+\varphi_0)}. \qquad (0.2.3)$$

The wave vector $\overrightarrow{k}$ is in the plane (x, z) see Figure 2.

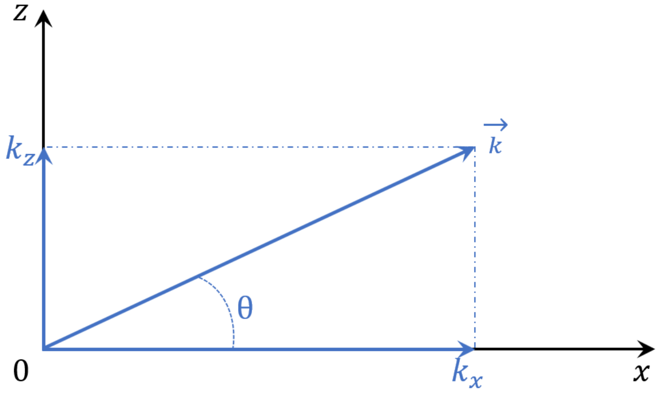

Figure 2: The wave vector k is in the plane (x, z)

For this case, the complex amplitude will be

$$f(x, z) = f_0 e^{i(k_x x + k_z z + \varphi_0)}. \qquad (0.2.4)$$

The projections of wave vector k are not independent:

$$k_x^2 + k_z^2 = k^2. \qquad (0.2.5)$$

Thus, $k_z = \sqrt{k^2 - k_x^2}$. Therefore, the complex amplitude of a plane wave can be expressed as follows:

$$f(x, z) = f(x, 0) e^{i\sqrt{k^2 - k_x^2} z}; \qquad (0.2.6)$$

Where complex amplitude of the plane wave in plane $z = 0$ is:

$$f(x, 0) = a_0 e^{i\varphi_0} e^{ik_x x} = c e^{ik_x x}. \tag{0.2.7}$$

Let's put in the $z = 0$ plane a sine amplitude grating with the transfer function:

$$T(x) = 1 + mcos(\Omega x). \tag{0.2.8}$$

Thus, right behind the grating, the complex amplitude of the wave will be:

$$f(x) = a_0(1 + mcos(\Omega x)) = a_0(1 + \frac{m}{2} e^{i\Omega x} + \frac{m}{2} e^{-i\Omega x}). \tag{0.2.9}$$

By multiplying amplitude of plane wave on a 1-dimensional transfer function we can get an expression for the complex amplitude in any point of (x, z) plane where $z = const \neq 0$. To do this we transform Equation 0.2.9 using Equation 0.2.6:

$$\begin{aligned} f(x, z) &= a_0(1 + mcos(\Omega x))e^{i\sqrt{k^2 - k_x^2}z} \\ &= a_0 e^{i\sqrt{k^2 - k_x^2}z}(1 + \frac{m}{2} e^{i(\Omega x + \sqrt{k^2 - \Omega^2}z} + \frac{m}{2} e^{-i(\Omega x + \sqrt{k^2 - \Omega^2}z)}) \end{aligned} \tag{0.2.10}$$

Thereby, the diffraction at an amplitude sine grating results in three plane waves. One of them propagates straight in z direction and two others - in directions determined by the grating period: $sin\theta = \pm\frac{\Omega}{k}$.

Moreover, the Equation 0.2.10 implies that if grating period is smaller than the wavelength, in other words, $\Omega > k$, $i\sqrt{k^2 - \Omega^2} \cdot z$ becomes real and the field amplitude will decay exponentially. Such a field called evanescent or near-field. These results confirm Abbe's theory.

The diffraction of the initial wave on a more fine structure forces the secondary waves to have a more significant divergence angle. Thus to see more detailed structure one needs to use lenses with a bigger NA value.

If the object is smaller than the wavelength, diffracted waves are evanescent and cannot be detected with a classical microscope setup (detector placed on a distance much larger than the wavelength). Here is the limit of traditional optical microscopy. However one can immediately see a way to overcome this limitation: the detector must be placed close to the sample - in the near-field. At the same time, the sizes of the sensor must be comparable with the size of the object features. Since the detector will observe only local intensity, it should be scanned along the XY plane to get information about the whole structure. Or due to the reciprocity of electromagnetic field, a reversed scheme can be used: the detector should be placed in far-field, and the sample should be scanned via fine light source (smaller than the wavelength). The latter method is much widespread nowadays.

0.3 SCANNING NEAR-FIELD OPTICAL MICROSCOPE

As it was said before, the sample should be scanned via a small probe, regardless if it is a detector or a light source. That classifies SNOM as a scanning probe microscope.

There are two main types of SNOM: apertured scanning near-Field optical microscope (a-SNOM) and scattering scanning near-field optical microscope (s-SNOM). In s-SNOM, near-field originates from coupled optical/electronic oscillations caused by the light focused on the sharp metal/dielectric tip. Although the resolution of such a microscope is determined by the apex radius (typically $10-20nm$), strong background signal coming from laser light exposure results in difficulties for the interpretation of an image and leads to a channels crosstalk.

A-SNOM uses sub-wavelength aperture for the light confinement (since this work is devoted to a-SNOM, only this type will be discussed). The probe can be used as a light source or light harvester. In any case, the tip should be placed in the near-field zone of a test object. Due to the exponential decay of the near-field [11], it is essential to keep the probe on a constant distance from the sample surface ($10nm$ typically). This feature allows extracting additional information about the sample's topography. An a-SNOM have five primary modes: illumination, collection, illumination collection, reflection and reflection collection. However, illumination mode remains the most popular. In this regime, the sample is illuminated through the sub-wavelength aperture which is kept close to the surface. During this process, only a small part of the sample is irradiated leading to longer sample life. Also, the much larger efficiency collection of light can be realized.

The typical SNOM setup is represented below, see Figure 3.

The laser light is guided through the optical fiber which has a small subwavelength size aperture at the end. Since the apex opening must be kept close to the surface, there should be a distance control system.

The first invented SNOM used tunneling current as a feedback mechanism [12]. To realize it according to the procedure described above, the prepared tip must be coated additionally with indium tin oxide to provide proper electron properties. Since the tunneling current is exponentially dependent on the distance, it can provide outstanding resolution in topography channel and give additional information about surface properties, but greatly reduces field of applications - only conductive samples can be studied

Later on, Betzig used scattering-based method utilizing shear-force mechanism [13]. In such an approach, the laser light should be focused on the fiber probe and then, the scattered light is collected by a position-sensitive diode (PSD) which will give a signal

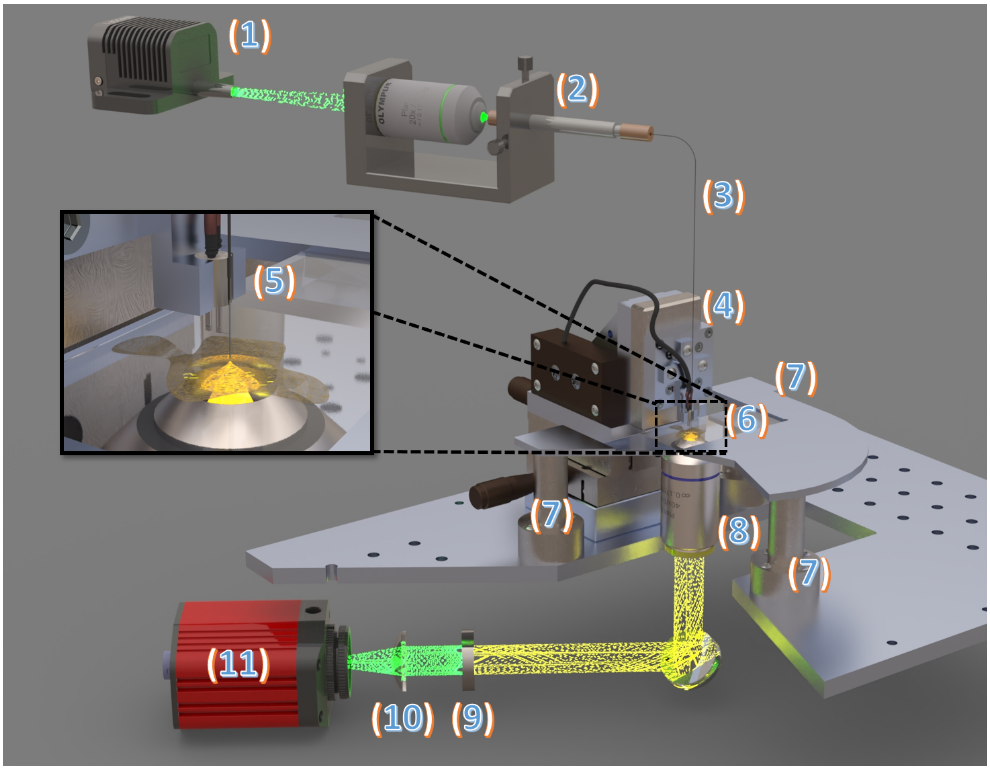

Figure 3: Scheme of typical SNOM setup. (1) - laser; (2) - fiber coupler; (3) - optical fiber; (4) - Z scanner holding a (5) - sharp tip attached to the quartz tuning fork in double-resonance condition; (6) - sample on the cover-glass placed on the (7) - XY scanning system; (8) - signal collecting objective; (9) - optical filter; (10) - focusing lens; (11) - light detector.

proportional to the amplitude of oscillation.

Nowadays, the most popular method of the SNOM tip-sample distance control is the shear force – based feedback employing a fiber attached to the quartz TF first introduced in 1995 [14, 15]. In this method, the tip oscillates almost parallel to the surface of the studied sample with a few nanometers amplitude.

As an alternative, normal force feedback mechanism was realized by the group from Israel [16]. They used the laser light reflected from the cantilever-like fiber towards a PSD. A tiny mirror was attached to the fiber to improve the reflected signal quality.

One should, however, not forget that all these methods are united by one thing:

when the tip is close to the sample surface (tens of nm), the oscillation amplitude (as well as the resonant frequency and quality factor) drops in comparison to the free-standing probe tip. That can be detected and used as a feedback signal for the distance control. The light coming through the aperture interacts with a sample and converts into far-field irradiation which can be efficiently collected by a micro objective and detected via standard devices (e.g. charge-coupled device (CCD) camera, photo-multiplier tube). For convenience, this scheme is usually based on an inverted optical microscope.

0.4 SCANNING NEAR-FIELD OPTICAL MICROSCOPY PROBE

The key element of a SNOM is the probe. It should have a sharp tip with a sub-wavelength aperture, and have some mechanism of keeping this tip at a fixed distance from the sample.

0.4.1 FIBER TIP

For visible light several different apertured tips were developed [9, 17, 18]. However, only the sharpened single mode optical fiber tip coated by aluminum, first realized in 1991 [19] proved to be efficient. According to this concept, the optical fiber should be sharpened in such a manner that it has a flat end face ($20nm$ $<$ diameter $<$ $500nm$) perpendicular to the fiber axis. The resulting tip apex must be coated by shadow evaporation (see Figure 4) with an aluminum layer ($> 100nm$). The key of success of such a tip is the efficiency of light transmission. Note, that the optical resolution of SNOM is limited by aperture size and is typically $50 - 100nm$.

To realize such a tip one must think about two primary steps: the sharpening of the fiber and the coating of the sharpened fiber in the right way.

There exist two ways to prepare a sharp tip: the heating and pulling or the chemical etching method. Both of them have endured till current days. However, they result in different properties of a tip.

The heating and pulling method results into conoid with a smooth surface and almost a flat end face [20]. This means that the metal coating will have an excellent quality. However, such a tip will have a blunt end (which results in poor topography resolution) and low range of available aspect ratios. Furthermore, heating and pulling of the fiber leads to the significant decrease of the light transmittance due to the mixing of the core with the cladding

Chemical etching method initially invented by Turner [21] results in much better tip quality. The formation of the apex occurs due to so-called meniscus etching in hydrofluoric acid. A fiber with a larger radius creates larger meniscus. Thus the etching of the fiber reduces its diameter, and this leads to the reduction of the meniscus. In details, this problem was solved many years ago [22, 23]. Such a method of etching results into sharp reproducible tips (aspect ratio can be varied by adjusting the etching solution). However, the etching procedure usually leads to a rough surface which causes relatively poor metal coating quality. This problem can be solved using the tube etching method developed by Stöckle in 1999 [24]. Convective flow of HF inside of a polymer layer results into a much smoother surface of the tip. Unfortunately, this process remains very hazardous.

The resulting sharp tips must be coated by a metal layer to localize light at the very apex of the tip. To do this, a so-called shadow coating procedure can be used. In this method, the process of the aperture formation occurs as follows. Coating by evaporation of a metal takes place on the fiber rotating around its axis in such conditions that the apex is in the geometrical shadow, see Figure 4. Thus the side walls are coating much faster than the apex which leads to an automatic aperture formation on the apex.

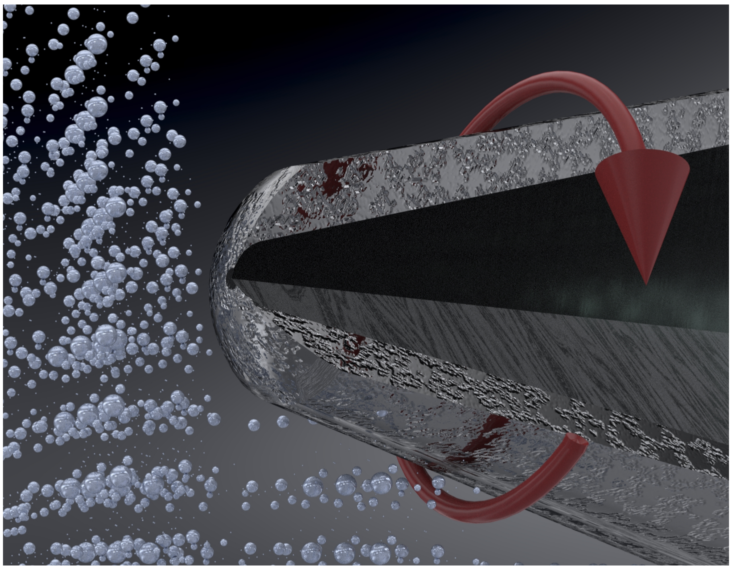

Figure 4: Principle of metal coating by the shadow evaporation

Needless to say that glass fiber probes are incredibly fragile and require very careful handling.

0.4.2 SHEAR-FORCE FEEDBACK MECHANISM

The first shear force feedback mechanism for SNOM was realized by Betzig [15]. In this experiment, he extracted the oscillation amplitude from the light scattered by the fiber. As it was said before, normal force feedback was implemented as an alternative. However, all these methods have one severe disadvantage - additional laser light brings a strong parasitic signal.

In 1995 a tuning fork based shear-force detector was implemented [25]. This method is realized as follows. The prepared probe is glued along one prong of the TF. The system is excited at its resonance frequency (close to $2^{15}Hz = 32768Hz$). Approaching this fiber to the sample surface leads to the drop of the oscillation amplitude, and a shift of the resonance frequency, and Q-factor. As a result, a signal coming from TF is changing, and the shift in frequency can be detected and used as a feedback. As an explanation of the mechanism, different concepts were proposed such as time-varying attractive Van der Waals and capillary forces acting on the tip [14] or actual contact between the fiber and the specimen [26]. But is most important, this method allows to achieve stable operation of the SNOM.

0.4.3 Tuning fork resonator

TF is a quartz Y-shaped resonator (see Figure 5) utilizing piezoelectric effect and mechanical resonance to achieve an electrical signal with a precise frequency. The oscillator's fork is made of quartz crystal. The electrodes are thin metallic stripes realized by a chemical vapor deposition (CVD) or "burning in" method and have a specific orientation to the crystallographic axis. The resonator is fixed in the nodes of working oscillation mode to diminish energy dissipation through the crystal fixation. The use of electrodes allows the electrical excitation of a TF. Due to the stiffness of quartz, the component has a large quality factor and outstanding frequency stability.

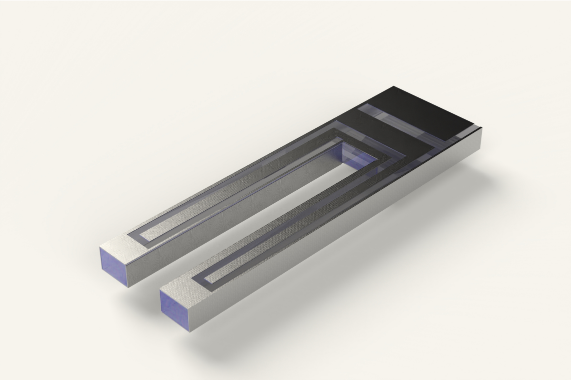

Figure 5: The model of a TF resonator

0.4.4 PROBE MONTAGE MECHANISM

The finished SNOM probes should be attached to the quartz TF. There are two main ways of doing that.

The first method which is in use since the invention of TF as a feedback sensor is a non-resonant set-up. To attach the fiber to the TF one needs to glue the fiber onto TF prong in such a way that the protruding part of the fiber should be $\approx 0.5mm$. This results in the formation of a mechanical system with quite low Q-factor (below 300) enabling, high operation speed but with limited sensitivity.

The second way is to use the double resonant conditions [27, 28]. Such montage requires the matching of the frequencies: the working frequency of the tuning fork (which is close to $32756Hz$) coincides with the second resonant frequency of the lateral dithering of the free-standing part of the fiber beam. It is essential to glue carefully both the fiber onto the metal case of the TF (to create the "hinging point"), and the $40\mu m-$diameter glass driving rod onto the fiber and one of the TF's prongs (see Figure 6). Such a method of attaching of the fiber to the tuning fork results in a quite large quality factor: the initial value of Q is lying in the range of $10000-12000$, which is characteristic for a free unloaded tuning fork in air, and then drops down to values ranging $4000-6000$ after proper gluing of a glass fiber probe onto it.

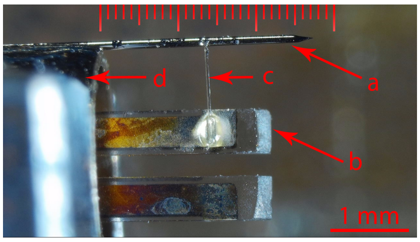

Figure 6: Double-resonant montage of metalized POF (a) onto a TF (b) via thin glass rod (c) connecting fiber and TF. d - metal case.

0.5 FLUORESCENCE RESONANCE ENERGY TRANSFER SCANNING NEAR-FIELD OPTICAL MICROSCOPY

As it was said earlier, the optical resolution of classical SNOM is limited by an aperture size. However, it can be further improved. FRET is one of the most promising ways of SNOM evolution.

FRET is an electrodynamical phenomenon which occurs between a donor molecule (in the excited state) and an acceptor molecule (in the ground state), caused by dipole-dipole interaction [29]. The donor molecule emits light that spectrally overlaps with the absorption of the acceptor. At small distances, such an interaction occurs without the emission of a photon. The transfer rate of energy as a function of donor-acceptor distance r can be expressed as follows:

$$k_T(r) = \frac{1}{\tau_D}(\frac{R_0}{r})^6, \tag{0.5.1}$$

Where τ_D is the decay time of the donor in the absence of acceptor and R_0 is the Förster distance. The R_0 can be determined as the distance at which half of the donor molecules decay by energy transfer and half decay by the usual radiative way. It varies from 20 to 90 Å for typical donor-acceptor pairs.

The idea of FRET SNOM is to use a donor (acceptor) nanoparticles/molecules as local fluorescence centers attached to the tip and measure the fluorescence induced by them in the sample (or vice versa) due to the FRET effect. This idea has been realized at the single molecule level with single $CdSe$ nanocrystals and appropriate dye molecules [30]. Despite the very high spatial resolution (better than $20nm$) attained in this experiment, it remains an isolated one, and this is for a valid reason: albeit rather large, the photostability of dye molecules and semiconductor nanocrystals still enables to use a single fluorescence center exploiting for imaging only a few minutes at best. Fluorescent centers with high photostability should be used to overcome this problem.

0.6 THE ULTIMATE GOAL

This work is focused on the further increase of the resolution of a-SNOM and attempts to simplify the work of researchers utilizing SNOM. In the introduction chapter, the basic principles of SNOM operation were discussed, and several limitations were pointed out. Nowadays most of the biologists prefer to use classical optical microscopes due to their stability and the ease of use, despite their limitations. Still, the extreme sensitivity of SNOM allows performing measurements using ultra-low dyes concentration. Here, we propose avenues to improve the SNOM technique to further enhance its capabilities.

The primary goal was to find out if it is possible to realize stable a FRET SNOM. We report the results of our attempted experiments to use for FRET SNOM NV color centers in ND crystals which are claimed to be extraordinarily photostable and bright. Most of the attempts were unsuccessful, and as a plausible explanation, we propose the absence (instability) of NV centers lying close enough to the ND surface. Prospects of the use of rare earth ions in crystals, which are known to be extremely photostable, are also discussed.

The first step of SNOM technique improvement was to make probes sample-friendly, or in other words, to find the way how to minimize the sample and probe destruction during imaging. We report the realization of a new approach: bent sharpened glass optical fibers. Together with small tip-sample acting forces, bent fibers provide more convenient navigation in microscopic mode (due to saving the space above the tip). We prepared the glass fibers with carefully controlled (and small) sizes of the curved part and the radius of the curvature of the bending to realize tapping mode. The design of these probes has been based on detailed theoretical and numerical studies of the relative tip-sample surface motion. We showed that these same aforementioned small sizes are necessary to achieve the tapping mode; otherwise, the "shear force type" interaction not only persists but very often dominates the whole picture. The SNOM performance with such probes is also discussed.

The next step was to improve the durability of the probes. We developed alternative probes for SNOM made from POF with much less fragility (in comparison to glass one) and greater ease of tip preparation. The work has focused on finding of a proper POF which can be used as a substitute for glass fiber, an appropriate protocol of their preparation and further testing. As a result, we found an ideal (we believe) solution - fibers made of cyclo-olefin polymers which are known as a plastic glass. Thus we can get the same sharpness of the apex (resulting in excellent topography) and optical quality.

There are more applications of the SNOM microscopes. Namely, SNOM is the best tool to study electromagnetic surface waves. The nm-scale of field features requires very high optical resolution. In the frames of the development of plasmonic devices, we started the investigations of surface plasmon polaritons (SPP)-based structures. Since the electromagnetic waves propagating along the surface can be strongly affected by defects of the surface, we decided to study the influence of features of the waveguides on the field distribution. Presumably, the supporting structure gives a significant impact on the behavior of the electromagnetic waves as well. Thus we developed a high quality supporting structure for long-range surface plasmon polaritons propagating along the surface.

0.7 THE STRUCTURE

The thesis is structured into 7 chapters.

Chapter 0 provides the historical overview and the principles of SNOM.

Chapter 1 focuses on the possible realizations of FRET SNOM. The approach of use NV centers in ND crystals is reported.

Chapter 2 discusses in detail tapping mode SNOM.

Chapter 3 proposes a solution of SNOM tips lifetime problems.

Chapter 4 provides an overview of the SNOM performance with fictionalized probes.

Chapter 5 discusses the realization of the first photonic crystal (PC)-supported long-range surface plasmon polaritons (LRSPP) in thin silver nanofilms.

Chapter 6 provides the summarized results and an overview of the field.

Chapter 7 gives an extra information.

1

Fluorescence resonance energy transfer scanning near-field optical microscopy

A few years ago the first true single molecule FRET SNOM images were demonstrated using $CdSe$ semiconductor nanocrystal – dye molecule as donor-acceptor pair [30].

Despite this achievement, more extended experiments revealed the necessity to have much more photostable fluorescent centers if such imaging technique should become a practically used tool. Here we report the results of our experiments which were, attempted to use NV color centers in ND crystals: the ND crystals are claimed to be extremely photostable and have a large optical excitation and emission cross section, for FRET SNOM. All attempts were unsuccessful, and as a plausible explanation we propose the absence (instability) of NV centers lying close enough to the ND surface. Prospects of the use of rare earth ions in crystals, which are known to be extremely photostable are also discussed, for single molecule FRET SNOM.

1.1 Overview

FRET SNOM, which idea is illustrated in Figure 1.1, consists in a division of a donor – acceptor FRET pair between a SNOM tip and a sample[30, 31]. If donor fluorescent centers of the imaging tip are excited and the fluorescence of the acceptor centers of the sample is monitored (or vice versa) when the tip is scanning along the sample surface, the spatial resolution is governed not by the aperture size of the SNOM tip but by the value of a characteristic FRET (Förster) radius R_0. The latter for typical donor – acceptor pairs ranges between $2 - 9nm$ [32–34] and thus the spatial resolution of the SNOM microscope can be ten times improved without the loss of sensitivity: the resolution of a “standard” aperture SNOM is governed by an aperture size which can not be made essentially smaller than $50nm$ due to the very rapid decrease of the light transmission through the tip when the aperture is decreasing [35–37].

To achieve the subtip spatial resolution with this method, we do not need to work with single molecule version: only a cylinder with the radius $r = \sqrt{2RR_0}$ contributes to the signal [30], see Figure 1.1. Here R is the curvature radius of the SNOM probe

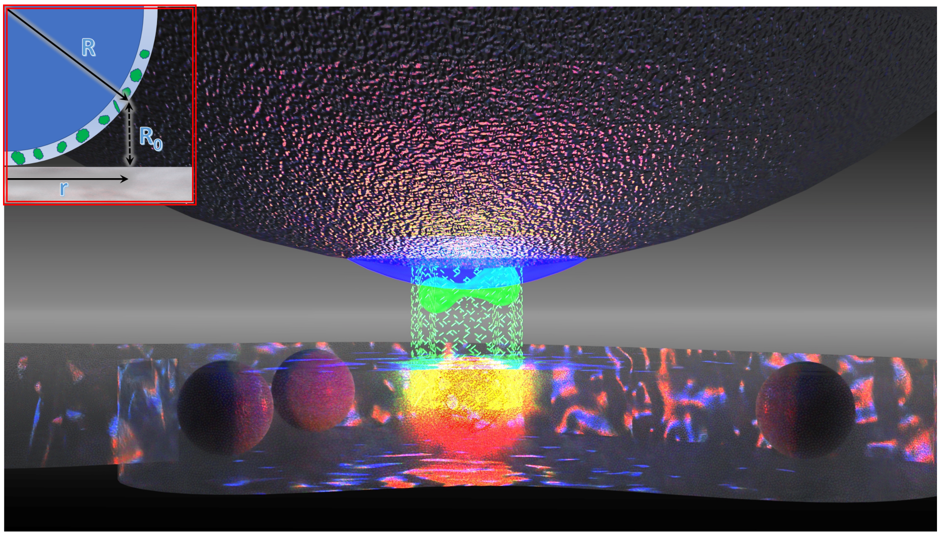

Figure 1.1: Illustration of the FRET SNOM approach, single fluorescent centre case. Schematic is shown on the inset, in the top right corner, where R is a radius of the curvature of SNOM probe apex; R_0 - Förster radius; $r = \sqrt{R^2 - (R - R_0)^2} \approx \sqrt{2RR_0}$ - the cylinder radius that contributes to the signal.

apex which is typically equal to $50 - 100nm$, and usually exactly this radius determines the spatial resolution. It is easy to see that $r << R$.

Immediately after the method has been proposed [31], the corresponding experiments were started and nanolocal FRET SNOM measurements and FRET SNOM images have been reported by a number of research groups using such fluorescent centers like dye molecules [38–41], semiconductor nanocrystals [42–44] and $F-$aggregated color centers in LiF crystals [45]. Finally, in 2008 these efforts lead to observation of true single molecule FRET SNOM images in an experiment where $4.8 - 4.9nm$ $CdSe$ nanocrystals (this is the core diameter; the core was covered with a protective $1 - 2nm$ thick ZnS layer) deposited onto a glass slide and were used as donors the Alexa Fluor 594 dye molecules (Molecular Probes, Oregon, USA) contained inside a thin poly(methyl methacrylate) (PMMA) coating over the SNOM tip apex were used as acceptors [30].

However, the results reported in [30] remained isolated and did not lead to the real appearance of single molecule FRET SNOM imaging methods. The current situation is still more like "towards single molecule FRET SNOM" because of the limited photostability of dye molecules and semiconductor nanocrystals used for imaging. (Our FRET SNOM studies involving $CdSe$ nanocrystals did not confirm that their photostability is much larger than that of rhodamine dyes contrary to what is often stated). The time of life of a fluorescent center is determined by the photostability $N_{phst} \cong 10^7 cycles$ (a good one) and is equal to

$$t = \frac{N_{phst} h\nu}{I\sigma}, \tag{1.1.1}$$

which give us $t \cong 30s$ for a typical single fluorescent center with optical absorption cross section $\sigma \cong 10^{-16} cm^2$, photon energy $h\nu \cong 3 \cdot 10^{-19} J$ and the near-field illumination intensity $I \cong 10^3 \frac{W}{cm^2}$. In practice, this means that to observe single molecule FRET SNOM images, a special construction of microscope enabling quite fast scanning should be exploited, and extreme precautions should be implemented to avoid the premature photobleaching of acting single FRET centre by light (such as opening of light source only after the scanning has already started, etc.). Despite all this, such an observation still requires a certain luck.

The situation would change dramatically provided that (say, two orders of magnitude) more photostable fluorescent centers are used. Naturally, this suggests to attempt the famous NV defect centers in ND crystals, claimed to be extremely photostable [46–49]. FRET SNOM imaging, and related studies were carried out not only in our group but also elsewhere. Still, to the best of our knowledge, these experiments did not result in obtaining of single molecule FRET SNOM images.

Another extremely photostable fluorescent centers are rare-earth ions in crystals, and they should naturally be considered as perspective, active elements for FRET SNOM as well. In particular $LuBO_3(Tb)$ microcrystals, in which FRET was observed in certain conditions before [50].

1.2 From CdSe nanocrystals to color centers in nano-diamond crystals

The limitations of our first single molecule FRET SNOM images brought us to the idea to use ultraphotostable NV color centers in ND crystals. Indeed, these same color centers were considered as prospective from the very beginning of the FRET SNOM research [31], while their first use in SNOM area (as local fluorescence source) goes back to 2000 [51]. The same motivation promotes the use (or attempts to use) of diamond NV fluorescent centers in many other areas. As an example, we can indicate the rather successful application of such an object in STED Microscopy field [52, 53] where exactly the same photostability problem defines the ultimate spatial resolution achievable.

Photophysics of NV color centers is still not fully understood and remains debated. Especially, this is valid when details concerning charge states NV^0 and NV^- of nitrogen vacancy and their inter-transformations (either spontaneous or specially induced) are considered. Nowadays, almost exclusively the NV^- state that is exploited. It was decided not to target certain particular charge state but to search for imaging caused by either NV^0 (luminescence band essentially in $570-700nm$ spectral range) or NV^- $(620-750nm)$ states. Indeed, detailed time-resolved experiments with single NV centers show the photo-switching from neutral to negatively charged state of NV as well as reverse photochromic transformation with the time constant ranging $0.3-3.6\mu s$ ($2.1\mu s$ average) under dark conditions [54]; earlier, photochromism has been shown for bulk samples [55]. There are no two different types of defects but "both fluorescence bands originate from the same defect" and "continuous switching between two charge states exists" [54]. The laser ionization of nitrogen donors present in the vicinity of the NV defect is a plausible mechanism of NV^0 to NV^- conversion, and this means that such a process should be strongly dependent on the concrete properties of colored ND and laser illumination conditions. In a sense, NV^0 state should be considered as a "main" one which is initially present (and consequently, its luminescence should be "always" observed) while NV^- state should first be created by the irradiation so that its observation may be not guaranteed at all.

Following this paradigm, different laser dye molecules to be exploited as acceptors for either NV^0 or NV^- donors were systematically tested in our experiments (oxazine 1, oxazine 750, Rhodamine 800) [56]. This circumstance makes mostly irrelevant still much debated question to what extent the neutral charge state is preferable at small (a few nanometers) distances from the ND particle surface and to what extent (if any) the $\frac{NV^-}{NV^0}$ concentration ratio can be influenced by surface modification or other means [57–60].

Two different sources of bright colored ND crystals were used in our experiments. The first were solutions and powders of ND crystals purchased from Microdiamant AG, Lengwill, Switzerland, with the median size of $25nm$ or $50nm$ and the communicated concentration of the nitrogen vacancies approximately $25 - 100ppm$ In Figure 1.2 we present an AFM image of these particles.

To color them, the powder of these diamonds has been introduced into specially prepared "flat" envelopes made from thin $50\mu m$ thick Al foil and irradiated by $2.4MeV-$energy electron beam in the accelerator ILU-6 (average current $23mA$) of the Institute of Nuclear Physics Siberian Branch of Russian Academy of Sciences,

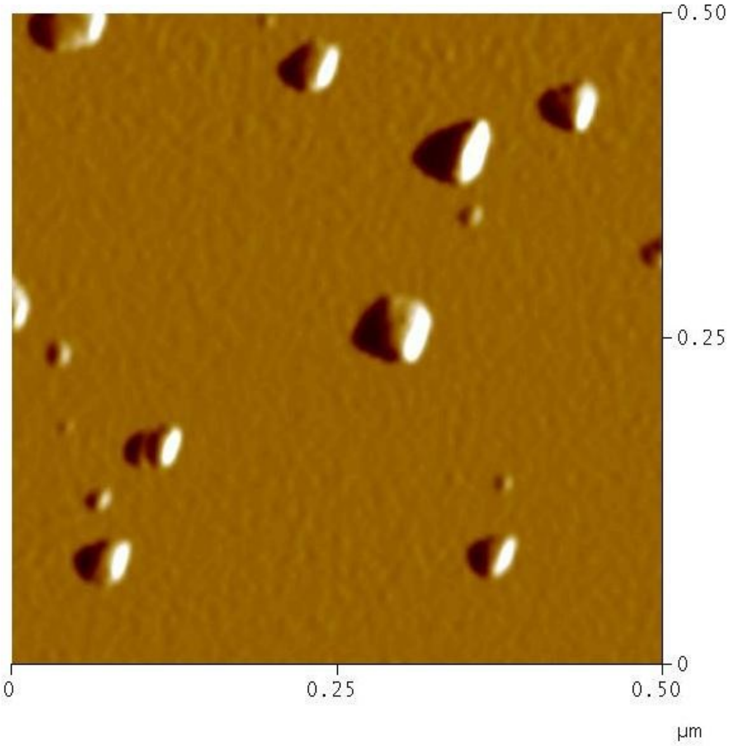

Figure 1.2: AFM (Digital Instrument, Santa Barbara, USA, NanoscopeIII, tapping mode) image of $50nm$-size nanodiamond particles deposited onto aptes-coated mica

Novosibirsk, Russia. The total dose of the irradiation was set to be equal to $1 \cdot 10^{18} \frac{e}{cm^2}$ (for one-half of the sample) and $2 \cdot 10^{18} \frac{e}{cm^2}$ (another half). Afterwards, the irradiated diamond dust has been thermally annealed in technical vacuum (around $1mTor$) at the temperature of $750 - 800$°C during two hours. No further treatment aiming to remove graphite layers possibly covering the irradiated NDs [53, 61] was undertaken. This procedure is more or less similar to those suggested in many other papers. It was reported that for $3 \cdot 10^{17} \frac{e}{cm^2}$ and $1.5MeV$ dose and energy of electron beam, roughly one NV center in a $30nm$ - diameter sphere has been created [62, 63] thus we anticipated somewhat similar results for our case.

The second sample of fluorescent nanodiamonds were commercially available coloured NDs in solution obtained from L. M. Van Moppes & Sons SA, Geneva, Switzerland, (average size of $65nm$, concentration of NV colour centres was not communicated), and Adámas Nanotechnologies, Inc., Raleigh, NC, USA, Companies. For the latter, the content of color centers was indicated as on average $1-4$ NV fluorescent centers in one $40nm-$size ND particle has been indicated.

In Figure 1.3 we present the $3D$ photoluminescence spectra of $40nm$-diameter ND obtained for different excitation wavelengths (results for other solutions of fluorescent ND were similar with appropriate scaling). To prepare the sample, a drop of $5\mu g/ml$ water-based suspension of colored $40nm$-size ND particles was dried on a glass slide.

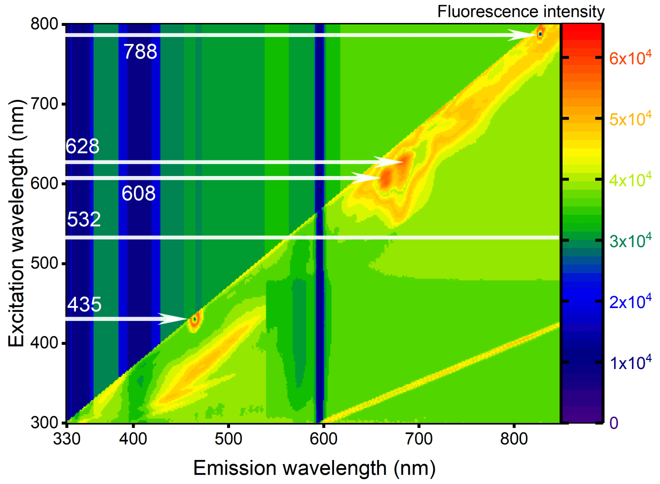

Figure 1.3: 3D Fluorescence spectra of ND with diameter $40nm$ deposited on a glass slide. Y axis corresponds to excitation wavelength, X - to emission, Z – intensity of emission. Fluorescence spectra were recorded via Jasco FP-8500 spectrofluorimeter (Easton, MD, USA) with a detector sensitive in the $200-850nm$ spectral range.

The first conclusion from these data is the very strong presence of all possible types of light "scattering" in the recorded signal. (We use this word as a generic term to describe all observed signal that is not NV luminescence band(s); we did not perform detailed studies to trace out its origin deeming this irrelevant for our purposes to construct FRET SNOM. Unfortunately, existence and importance of this type of optical signal are almost never reported in the literature). The second conclusion is the presence of two bright spots located about $435nm$ and $788nm$ excitation wavelength which we believe correspond to dust particles. Large bright "smeared" spot is observed in the excitation range $\approx\ 590nm - 640nm$, and we believe this is the only appropriate excitation range for the method. (In most papers $532nm$ excitation band as quite strong for NV-vacancies for natural diamonds is reported. However, we did not see noticeable emission at $532nm$ excitation).

The set of fluorescent spectra of ND-water solution, see Figure 1.4, reveals a strong dependence of the "fluorescence" peak position on excitation wavelength. Such a situation is more typical for the Raman scattering of water for example.

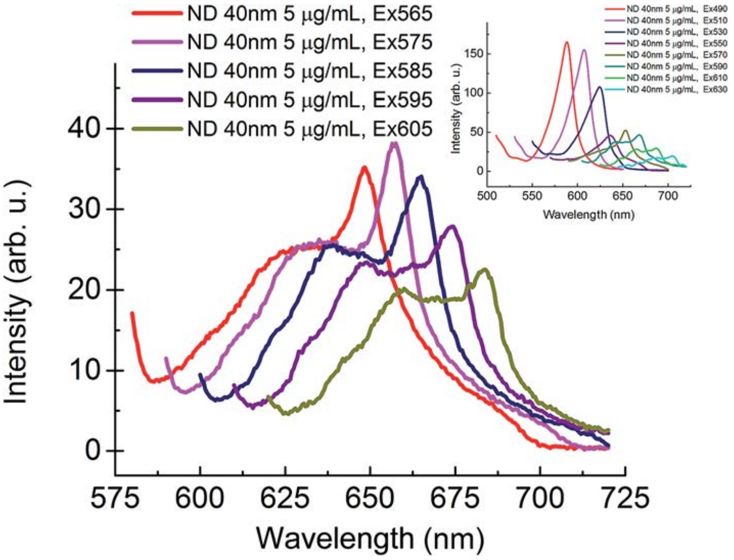

Figure 1.4: Optical signal recorded at different excitation wavelengths for $5\mu g/ml$ water-based suspensions of colored 40 nm-size ND particles. The known NV^0 luminescence band ($590 - 700nm$) is seen when excited in the spectral range $540 - 630nm$ and is not seen when excited at shorter wavelengths, see the inset. The spectra were recorded using a Jasco FP-8500 spectrofluorimeter (Easton, MD, USA) with a detector sensitive in the $200 - 750nm$ spectral range, which may obscure observation of the red part of the NV center's fluorescence.

A direct comparison of the fluorescent signal obtained from a solution of colored $40nm$-diameter ND with that of Sulphorhodamine B ethanol solution [56] excited in the spectral range $530 - 570nm$, was made assuming for both the same quantum yield and optical absorption cross-section of $3 \cdot 10^{-17} cm^2$ at maximum for NV centers [64] (the latter is equal to $6 \cdot 10^{-17} cm^2$ for dye molecules at the wavelength of $532nm$ [56]). This comparison led to the estimation of the average number of NV centers in one ND particle as $0.4 - 0.8$ thus being indeed not too far from the data communicated by the producer. Similar estimations gave for $25nm-$diameter ND colored in Novosibirsk the value approximately $0.2 - 0.4$.

Still to attest the NV luminescence excited by nanosecond pulsed $532nm$ laser, we performed measurments of fluorescence kinetics (see Figure 1.5) which gives a lifetime (intensity weighted) equal to ca. $16ns$, thus quite comparable with the literature data [46–49] (Time Correlated Single Photon Counting module PicoHarp 300, PicoQuant, Berlin, Germany, was used). Such a measurement required incredibly long time of recording (more than 12 hours) due to very weak signal.

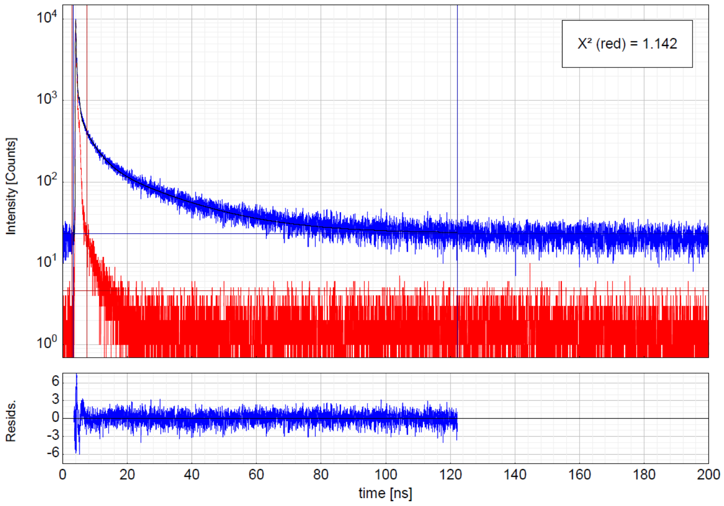

Figure 1.5: Intensity decay of fluorescent $40nm$- NDs in water solution (blue curve on the top). The red curve corresponds to an instrument response function (IRF). The blue curve on the bottom represents χ^2 of de-convolution of the intensity decay with the IRF using two exponential decay model.

Similar kinetics have been observed for ND samples in thin polymer films and thin layers of polymer deposited onto aperture SNOM tip apex. To attach NDs to the sample/probe we used chitosan (CHI) as a matrix. The mixture of $1\mu l$ of ND ($w_{ND} = 0.1\%$, water suspension) and $50\mu l$ of CHI solution ($w_{CHI} = 0.1\%$: $1mg$ of CHI dissolved in $1.0g$ of CH_3COOH 0.8% water solution) give an excellent distribution of particles resulting in isolated particle next to the tip aperture, see (figs. 1.6a and 1.6b).

The efficiency of excitation of the NV centers fluorescence by ns-pulsed $532nm$ laser, with which the most of FRET SNOM experiments employing ND were made, is hard to estimate. Our data suggest for the corresponding cross section the value something like at least one order of magnitude smaller than at maximum, i.e. $\sim 3 \cdot 10^{-18} cm^2$. (Note the value $1 \cdot 10^{-17} cm^2$ used for the optical excitation cross section at this wavelength in [65]).

For FRET SNOM experiments, the distance between donor and acceptor should be smaller than the Förster radius R_0. This adds one more constrain which from the first glance does not look too restrictive: for a spherical particle of radius R, only those color centers which lie at the distances larger than $R - r$ with $r < R_0$ from the center, can contribute. For $R = 12.5nm$ and $r = 3nm$ this signifies that more than one half of all NV centers, provided they are evenly distributed inside a nanocrystal, can be excited.

In brief, the numbers given above show that the task to realize single molecule FRET SNOM with NV color centers in NDs presently available is certainly demanding. With the aim of coating the SNOM probe with NDs, we dipped the probes into solutions containing a polymer (PMMA or chitosan) to attach the NDs to the tips. A suitable solvent for the polymer (acetone, chloroform or ethanol) and different NDs samples were used. We retracted the probes from solutions in different ways and let the solvents to evaporate. In this way, we presented tips coated with NDs of varying sizes and varying concentrations of NV centers. After solvent evaporation, one has at hand an

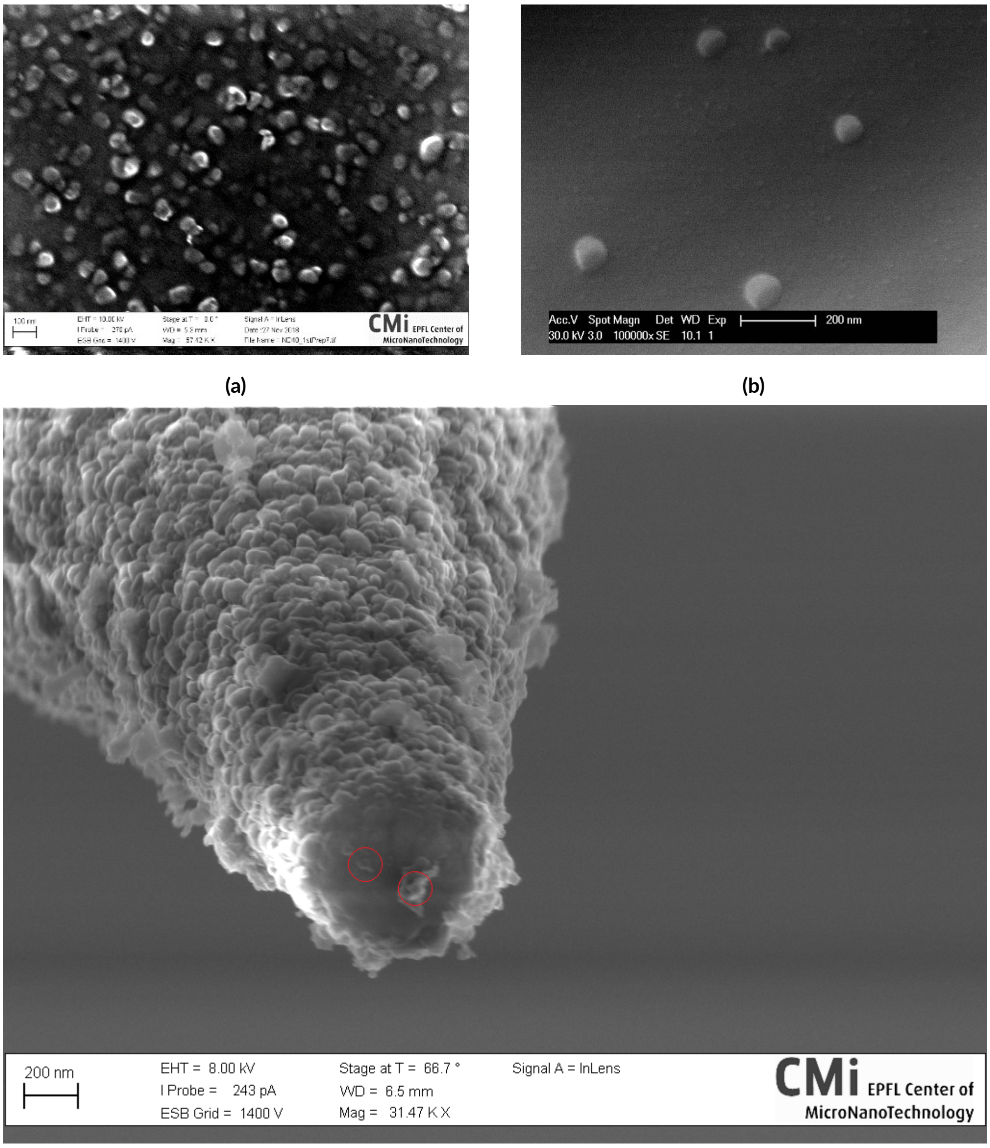

(a) (b)

(c)

Figure 1.6: The SEM image of 5 µl ND-CHI solution dried on freshly cleaved mica. On the 1.6c image, the obtaining of isolated individual ND particles with this approach is illustrated. 1.6c: SEM image of SNOM tip coated with NDs, isolated particles are marked with red circles.

aperture SNOM probe which is covered by thin polymer layer with ND particles; the presence of the latter has been confirmed by fluorescent and kinetic measurements, see Figure 1.6. Previously, we prepared similar probes with dye molecules [41] and $CdSe$ semiconductor nanocrystals [42] (we coined the name "self-sharpening pencil probe" for them).

Nevertheless, despite all these efforts, we were unable to acquire FRET SNOM images with such probes coated with layers of Oxazine 1, Oxazine 750 or Rhodamine 800 dyes [56] (calculated Förster radii range $46nm$) even at the "many molecules" level. (These experiments were performed exploiting the excitation by a nanosecond pulsed $532nm$ laser, $607nm$ continuous wave (CW) laser and CW argon ion laser line at $514nm$; in all cases the necessary Kaiser Optics notch filter and appropriate set of long pass optical filters were exploited.

Results of our experiments show that the fluorescence efficiency of NV center in ND crystals is much smaller than 1. Recently, it was confirmed in [66] that the real quantum yield of NV in ND is much smaller than 1 and typically does not exceed 0.2 with an average value of 0.03, which makes NDs useless for our aims. If one would measure the fluorescence of $100nm$ NDs with concentration of $0.1g/L$, it will be ~ 55 times weaker than the Raman scattering of water [67] (the exact concentration of NV centers in ND in this work is not mentioned). Furthermore, crashing of $100nm$ NDs to a $30-50nm$ size will reduce emission by ≈ 25 times [66, 67]. Taking into account blinking effect [68] which become noticeable when NV-centers are close to the surface, NDs with NV-color centers become practically useless.

It is known and broadly accepted in the area of near field optics (and fully corresponds to our own experience) that, when working with CW laser, light intensity at the subwavelength-size aperture of SNOM probe cannot exceed the value around

$I \cong 10^3 W/cm^2$, and this corresponds to the laser power of ca. $0.5 - 3mW$ at the entrance of the probe made of single-mode glass fiber. For larger values, the probe can be easily damaged and burned by light. Correspondingly, when measuring the signal caused by single fluorescent center, we can expect approximately a counting rate of:

$$n = \eta \frac{I\sigma}{h\nu} \cong 3 \cdot 10^3 - 10^4 cps. \tag{1.2.1}$$

Where η is an overall efficiency coefficient which includes all factors such as fluorescence quantum yield, photon collection- and detector efficiencies. For the above estimation it is taken in the range $0.01 - 0.03$ (a good value indeed) while all other parameters are the same as were used on the page 46. This value is one-two orders of magnitude larger than a typical dark noise level of the single photon detector used. Experimentally it is quite difficult to diminish the parasitic noise signal, caused essentially by unavoidable stray light. However, if the quantum yield will drops by two orders of magnitude, the overall efficiency drops as well, and will result in a signal comparable with the dark noise level.

The FRET phenomenon observation between single approximately $20 - nm$ size ND and infrared IRdye-800CW (the calculated Förster radius is equal to $5.6nm$) has been reported in [69]. An analysis of this paper shows that here the fluorescent center is located somewhere close to the nanocrystal center, and a large number of dye molecules, attached to the surface of this particle, are responsible for an observed FRET. In this research, the authors used ND colored by $40keV\ He^+$ ion irradiation [70]. It is, of course, clear that much more bright particles can be obtained in such a way: we not once attempted to produce such bright sources. Starting from a liquid solution of $50nm$ diamond particles in water with initial concentration $7 \cdot$

$10^{10} - 7 \cdot 10^{12} particles/ml$ prepared by dissolving initial water solutions (with some additives to prevent coagulation) obtained from Microdiamant AG, Lengwill, Switzerland. A $10 \mu l$ droplet of the solution was deposited onto thin quartz plate, spread over the surface $\sim \ 0.5 cm^2$ and dried in air, afterwards these plates were immediately irradiated with He^+ ion beam, either of energy $1 MeV$ and dose $3 \cdot 10^{15} ion/cm^2$ in van der Graaf generator of Sevchenko Institute of Applied Physics Problems Belorussian State University, Minsk, Belarus, or of energy $1.7 MeV$ and dose $10^{15} ions/cm^2$ in tandemtrone accelerator of Indira Gandhi Center of Atomic Research, Kalpakkam, India. After a few days these quartz plates were annealed in technical vacuum at 700°C for two hours. Based on data reported in [70] and other available data concerning defect production in dielectrics by high energy ions, we estimated that in these conditions we should be close to the saturation, i.e. the most part of nitrogen vacancies could be transferred into fluorescent centers. These samples were indeed very bright and single fluorescent nanodiamond crystals were easily seen in our SNOM (in illumination mode) when excited by $514 nm$ line of cw argon ion laser, see Figure 1.7. Corresponding Kaiser notch filter and a set of appropriate glass color filters for cutting fluorescence shorter that $590 nm$ have been used during signal detection. Unfortunately, all attempts to "lift off" bright nanocrystal(s) from the quartz sample by approaching and gentle pressure cycle [71, 72] using bare or modified (for example, coated with thin polylysine layer) SNOM tip to prepare an active FRET SNOM tip grafted with ND crystal failed. The reverse experiment, namely to acquire FRET SNOM images of these ND using "self-sharpening pencil" aperture SNOM probes coated with thin layers of the aforementioned appropriate dyes [41] also were unsuccessful.

Next, besides the NV centers in ND, other types of defects are now considered

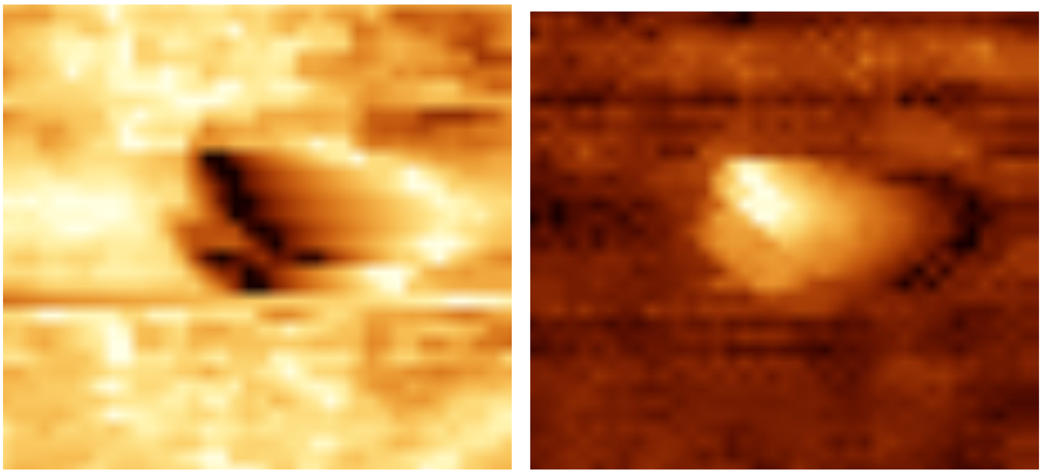

Figure 1.7: Topographical (left) and near-field fluorescent images (right) of $50nm$ - size NDs colored by He ion irradiation in Kalpakkam, India. Scan size: $150 \times 150nm$

to be used in quantum informatics and could be prospective samples for FRET SNOM. Diamond can have more than 500 types of defect centers: some of them look quite suitable, probably even more appropriate than NV centers for the task at hand. Analysis of the literature shows that, for example, chromium-related color centers, which possess narrow a fluorescent line $\sim 750nm$ and for which an enormous quantum efficiency was reported [73] look quite interesting. Similarly, Si-related color centers (narrow fluorescence line $\sim 740nm$) look interesting as well. Recently, precisely the circumstance that the SiV centers, contrary to the NV centers, are stable and bright emitters in particles as small as $1.6nm$ in size, became the main topic of research [74]; note also that these centers are also theoretically predicted to be stable in such small crystals [75]. Similarly, $Xe-$related vacancies [76] can be considered, and so on. However, the questions of their thermodynamic stability when close to the nanoparticle surface, as well as detailed studies of photostability of all these color centers (which is usually claimed to be quite large however, but we failed to find exact data) and their quantum efficiency must be undertaken before further steps in this direction will become possible.

1.3 FUTURE PLANS OF FLUORESCENCE RESONANCE ENERGY TRANSFER SCANNING NEAR-FIELD OPTICAL MICROSCOPY WITH RARE EARTH IONS IN NANOCRYSTALS

The Förster radius of FRET is independent on the donor dipole moment and directly related to parameters of the FRET pair (spectral overlap, orientation) and solution refraction index [32–34]. This is a prerequisite for the use of semiconductor nanocrystals or color centers (weaker than dye molecules) as donors for single molecule FRET SNOM. If one is willing to use rare earth ions in crystals for this purpose (for many of optical transitions in them the quantum efficiency is close to 100% even at room temperatures [77–80]), due to their optical absorption/emission cross sections (dipole forbidden intraband $f - f$ transitions) roughly $two - three$ orders of magnitude smaller than those pertinent for dyes [77–80], one will have instead of thousands $counts/s$, a signal at the level of only of the order of $10 counts/s$ (see Equation 1.2.1). Knowing that for relatively strong transitions of rare earth ions in crystals the fluorescence time ranges between tens to two hundreds of microseconds, the exploitation of $\mu s-$duration laser pulses with a repetition rate around $100 Hz$ (i.e. something similar to what we actually used in our experiments with acousto-optical modulator [27]) looks desirable and can lead to signal – noise ratio improvement that can overcome the dark noise detector limit (again, the total laser power at the SNOM fiber probe entrance should not exceed a few mW). However, of course, in any case such low level of the signal presupposes slow scanning rates, and it's hard to say if such an approach is realizable and might be useful in practice.

Certainly, the optical excitation cross section of rare earth ions can be a few orders of magnitude larger than the corresponding optical absorption/emission cross section if the energy transfer from organic ligands or nanoparticle surrounding this ion is involved [77]. Due to the very nature of FRET, if the donor-acceptor distance is equal to Förster distance R_0, the rate of energy transfer is equal to that of the radiation decay hence the process of imaging at such distances remains slow. Interesting possibilities might appear if we are able to work at donor-acceptor distances, say, twice smaller than the R_0 value. This will lead to roughly $2^6 = 64$ times increase of the FRET rate: consequently, one may observe sufficiently strong FRET signal when the active ion of the SNOM probe is very close to the acceptor, and observe no signal when there is not an appropriate donor in its vicinity. Besides, the scanning rate also might be essentially increased, and all this certainly looks promising for FRET SNOM.

A literature search [50, 81–84] has turned up interesting candidates: for example the following intense optical transition ${}^5D_4 \rightarrow^7 F_5$ (observed in $LuBO_3 : (Tb)$ crystals on the wavelength $\lambda_{max} = 542.3nm$) which was found in Tb^{3+} ions. Thus $LuBO_3 : (Tb)$ nanocrystals should be considered as a candidate for single molecule FRET SNOM. The ${}^5D_4 \rightarrow^7 F_5$ transition excited using standard $280nm$ $Nd : YAG$ pumped ultraviolet (UV) laser is followed by fast and effective decay of the excited state back to ${}^5D_4$ state with the light emission with maximum in the green part of spectrum.

The excitation efficiency of $LuBO_3 : (Tb)$ and certain FRET applications were already reported [50]. We established a collaboration with this group who prepared for us samples of $LuBO_3 : (Tb)$ microcrystals (see Figure 1.8 for an scanning electron microscope (SEM) image of the microcrystals).

The synthesized samples have different morphology, depending on the fractions of Tb^{3+}. A $5\mu L$ drop of water solution of 0.1% $LuBO_3(Tb)$ was deposited on a silicon wafer and then dried in air (see section 7.1). The sample with higher amount

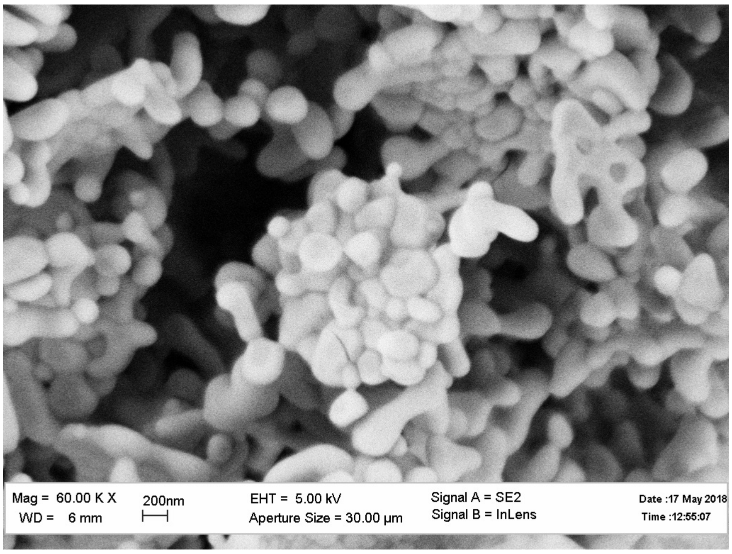

Figure 1.8: SEM image of $LuBO_3 : (Tb)$ microcrystals

of Tb^{3+} had flake-like particles, see Figure 1.9a. The lower portion of Tb^{3+} led to a formation of more compact structures, see Figure 1.9b. In both cases, the particles have microscopic size of the order of 1 to $50\mu m$, which is not convenient for utilizing them as a functional particles. To achieve smaller sized particles we used ultrasonication for a long period - 12 hours. Such a treatment leads to the functioning of the micro-crystals into nano-crystals, see Figure 1.9a and Figure 1.9b. Statistical analysis of multiple SEM images of ultrasonicated particles gives the maximum of the distribution for the radius at $120nm$ for $Lu_{0.925}BO_3 : (Tb_{0.075})$ and $400nm$ for $Lu_{0.85}BO_3 : (Tb_{0.15})$ respectively.

To excite the fluorescence of such crystals we used a LUV-280 laser (Photonic Solutions, United Kingdom) with the wavelength $280nm$ and output power up to $10mW$. The fluorescence spectra of $LuBO_3 : (Tb)$ microcrystals excited with such a laser is presented below (Figure 1.10). Such a laser excite the ${}^4F_8 \rightarrow^4 F_7{}^5D_1$ transition in Tb^{3+} ion, which is following by relaxation and fluorescence at $\lambda max = 542.3nm$

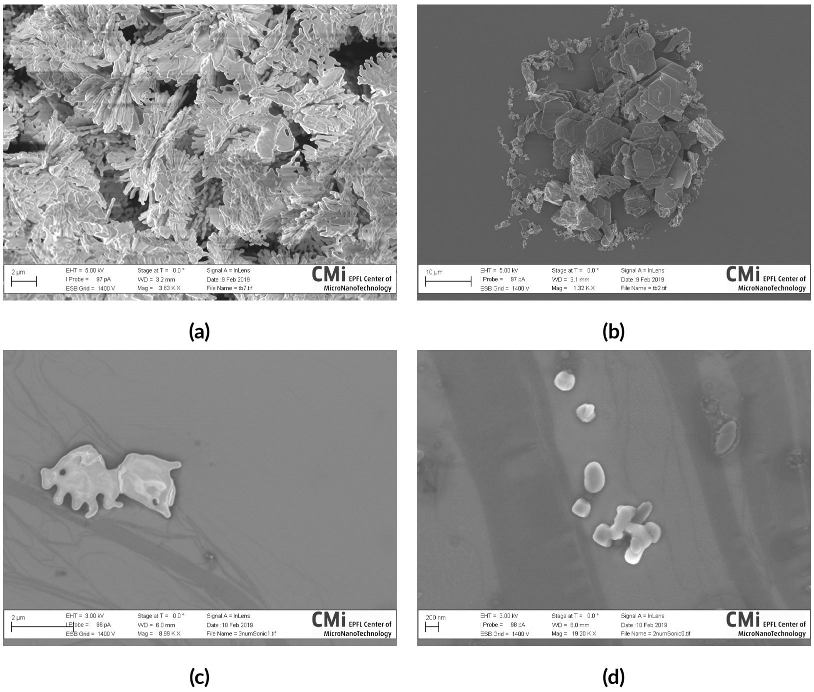

(a) (b) (c) (d)

Figure 1.9: Morphology of $Lu_{1-x}BO_3 : (Tb_x)$ deposited on a silicon wafer.

(a) $x = 0.15$

(b) $x = 0.075$

(c) $x = 0.15$, utlrasonicated for 12 hours

(d) $x = 0.075$, utlrasonicated for 12 hours

(transition $^5D_4 \rightarrow^7 F_5$).

The peak corresponding to this transition is clearly visible on the Figure 1.10. The red and blue curves corresponds to particles in a shape of a flake and have more intense signal at $\lambda_{max} = 542.3nm$ in comparison to the green and purple curves which correspond to a standard, round shape. Apparently, this complicated structure results in a higher value of absorption cross section and gives an increased quantum yield. Such a behavior is described in [66] for fluorescent NDs.

As an addition, the use of the UV laser, working in the UV region requires quartz optics and special fibers for the SNOM. The fiber probes capable of transmitting

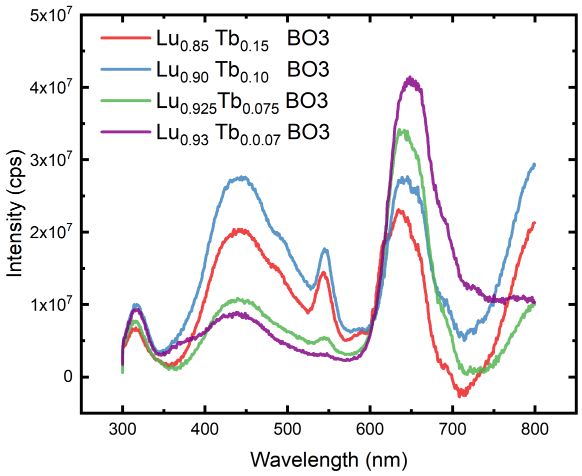

Figure 1.10: Fluorescence spectra of $LuBO_3(Tb)$ microcrystals with different Tb^{3+} fractions. The exciatation wavelength is $280nm$. The spectra were recorded using SpectraPro 2150i Spectrometer (Princeton Instruments, Massachusetts, USA) and LUV-280 laser in a 90° setup, the light was collected using $25mm$ focus $BK7$ lens.

$280nm$ light with high efficiency were prepared for us by NT-MDT company (Zelenograd, Russia). Quartz-made optics is widely commercially available. Hence, the realization of rare-earth based FRET SNOM is possible and is underway in our laboratory.

1.4 CONCLUSION

In the Thesis, the current state of single molecule FRET SNOM was discussed. Despite numerous many years-long efforts, we were unable to observe FRET SNOM images with ND crystals containing NV color centers. The most plausible explanation, we believe, is that the NV color centers in nanodiamond crystals, which are supposed to have ultrahigh photostability and absolute quantum yield, actually have neither of these properties, and the presented in the literature optical characteristics of them seems are overestimated most of the times. With some satisfaction we state that nowadays, in the literature it is already possible to find papers where the authors dare to arrive to the same conclusion, see e.g. aforementioned [66, 67]. At the end of the chapter another object and future plans were proposed. The possibility to utilize this candidate as a FRET donor for microscopy is very prominent. Some FRET application were shown before [50]. The efficiency of fluorescence excitation was approved by us as well.

This chapter is mainly based on the following article:

Sekatskii, S. K., K. Dukenbayev, Mounir Mensi, A. G. Mikhaylov, E. Rostova, A. Smirnov, N. Suriyamurthy, and G. Dietler. "Single molecule fluorescence resonance energy transfer scanning near-field optical microscopy: Potentials and challenges." Faraday discussions 184 (2015): 51-69.

Personal contribution: Detailed studying of the fluorescence of nanodiamond particles under different excitation conditions, searching for the most appropriate excitation conditions and numerous related FRET SNOM experiments. Elaboration of the method NDs attachment onto the SNOM tip, SEM analysis of functionalized probes. Performing the fluorescence lifetime measurements of the NV centers in NDs. Searching for the explanation of very weak fluorescence observed in all these experiments. Selection of nanocrystals with rare-earth ions as next promising material for the FRET SNOM and first experiments with them.

2

Tapping mode Scanning Near-Field Optical Microscopy with bent glass fiber probes

In the field of SNOM, the tapping mode feedback could be preferable to the shear force mode which is the most popular nowadays.

Such an approach can be realized, e.g., using bent fiber probes and it is often claimed that any fiber probe is suitable for this task. Detailed analysis of fiber vibration modes, however, shows that the realization of truly tapping mode of the probe dithering require an extreme caution. In the case of using the second resonance mode, probes vibrate mostly in shear-force mode unless the bending radius is rather small (ca. $0.3mm$) and the probe's tip is short. Otherwise, the shear force character of the dithering persists. Probes having these characteristics were prepared by heating of a tapered etched glass fiber with a CW CO_2 laser. We could show that to achieve a truly tapping character of dithering, short, not exceeding $3mm$, lengths of a free-standing part of bent fiber probe beam should also be used in the case of non-resonant excitation.

2.1 INTRODUCTION

The most popular method of the SNOM tip-sample distance control is the shear force – based feedback employing a fiber attached to the quartz TF first introduced in 1995 [25]. In this method, the tip oscillates (Figure 2.1a) almost parallel to the surface of the studied sample with a few nanometers amplitude. Near-field optics community has very much debated in the nineties and the beginning of XXI century [14, 26, 85, 86] the origins and physical mechanisms of the shear-force interaction. As an explanation, different concepts were proposed such as time-varying attractive Van der Waals and capillary forces acting on the tip [14] or actual contact between the fiber and the specimen. Although, some related debates still sometimes take place, nowadays, it seems established that a real contact between tip and sample surface occur at a certain point [26, 85–88]. In other words, there is no such a significant difference between shear-force and tapping modes. However, when the former is operative, the oscillation occurs at somewhat unfavorable conditions with the angle between the velocity of the movement of the fiber probe tip and the normal to the sample surface approaching ninety degrees. As a result, it appears that the shear-force distance control method is far from the ideal one. The crosstalk between optical and topographical image can degrade the results. The forces between the tip and sample are high and easily might be destructive. In particular, the direct measurement of the interaction force in combined SNOM - AFM device gives the values approximately $100 - 200nN$ [26] for the force perpendicular to the sample's surface [*].

These considerations lead many experimental groups to propose and implement a tapping mode SNOM feedback when the probe tip apparently moves roughly perpendicularly to the sample surface (Figure 2.1b), see, e.g. [89–95]. A few realizations of this approach were based on straight optical fibers or short fragments thereof properly attached to the tuning fork or bimorph [92, 93]. However, the use of long but bent optical fibers attached to the tuning fork in a standard fashion seems was the most popular [94]. Still, the detailed analysis of the relative fiber – sample surface motion in these experiments has not been performed. Herewith the "true tapping" character of this motion (comparable with the motion of AFM cantilever in the tapping-mode regime, see the end of "Simulations" section) was taken for granted.

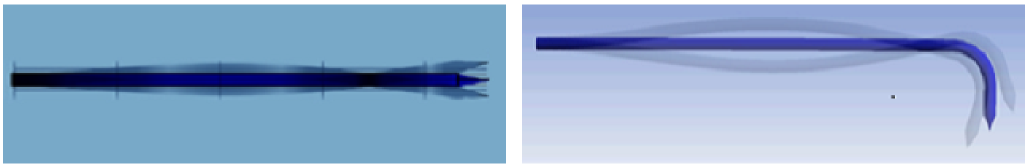

(a) The shear-force mode

(b) The tapping mode

Figure 2.1: The oscillation modes of SNOM probes

Here, we report the realization of a new approach to the problem: bent sharpened

---

[*] We do not discuss here the force parallel to the sample's surface

glass optical fibers with carefully controlled (and small) sizes of the bent part and the radius of the curvature of the bending were prepared and experimentally exploited as SNOM probes. The design of these probes has been based on detailed theoretical and numerical studies of the relative tip – sample surface motion. We showed that these same aforementioned small sizes are necessary to achieve the tapping mode; otherwise, the "shear force type" interaction not only persists but very often dominates the whole picture. In our opinion, there are substantial grounds to suppose that the most of the earlier reported tapping mode SNOMs were not the devices working in tapping mode.

2.2 SIMULATIONS

The commercially available software package ANSYS 17.2 (Canonsburg, PA, USA) was used for the numerical simulations. These simulations are based on the finite-element method [96] exploiting the triangulated models of the tip ("meshing") created via commercially available software package for modeling SolidWorks 2016 (Waltham, MS, USA). The local mesh size of the structure was based on the local curvature to cover all important (and possibly tiny) features of its design. The probe beams were hinged at the base. As a material, pure silicon was chosen for the AFM cantilevers and quartz for the fiber probes. The change of material properties (such as density ρ , elastic modulus E and Poisson ratio) does not impact the mode shape but, of course, strongly influences the absolute values of resonant dithering frequencies, see below.

We introduce the following notation (see Figure 2.2). The local symmetry axis of the probe's tip, see Fig. 1, is taken as Ox while the axis perpendicular to Ox and lying in the same plane as the Ox axis and the symmetry axis of the unbent part of the probe is taken as Oy. (The third axis, Oz, is not important since lateral oscillations in this direction are negligible). The origin of the coordinates was put at the point coinciding with the tip apex. For probe vibrations at the frequency ω, the motion of the tip apex can be expressed as

$$\overrightarrow{r(t)} = A_x \overrightarrow{i} cos(\omega_x t + \varphi_x) + A_y \overrightarrow{j} cos(\omega_y t + \varphi_y), \tag{2.2.1}$$

where at a moment we are not interested in the phases $\varphi_{x,y}$. We normalize the ratio between the amplitudes of the oscillations in Ox and Oy directions as

$$\psi = \frac{A_x^2}{A_x^2 + A_y^2}, \tag{2.2.2}$$

and name this quantity depending only on the probe characteristics and ranging between 0 and 1 “the tapping mode efficiency”: if the sample surface is parallel to the Oy axis, it gives the ratio of “tapping mode - type” and “shear force – type” movements of the probe apex.

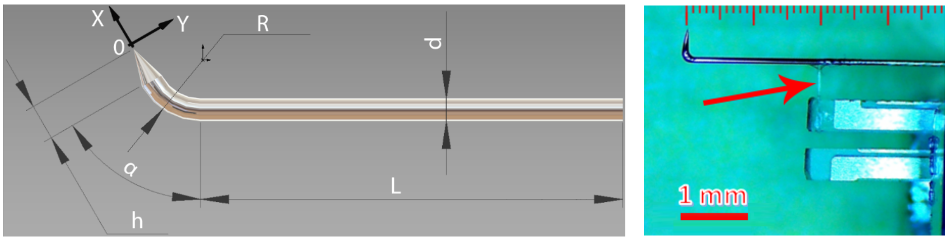

Figure 2.2: Illustrating the geometry of the bent fiber. On the left, the following sizes of the bent fiber probe are shown: α - bending angle, R – bending radius, d - fiber diameter, L - length of the fiber from the point at which it is rigidly fixed until the bent sector, h - length of the probe’s free part after the bending section. On the right, you can see the photo of a real bent fiber attached to the TF, here $\alpha \approx 90°, R \approx 300 \mu m, d = 125 \mu m, L = 4mm, h \approx 300 \mu m$. Thin glass fiber-made driving rod connecting the probe with one of the TF’s prongs is shown with a red arrow.

For straight, unbent glass fiber without a tapered part (i.e., ordinary cylinder), the resonant dithering frequencies can be found from the following equation (see, e.g.

[97]):

$$f_{res,n} = \frac{\Omega_n^2}{L^2}\sqrt{\frac{EI}{\rho S}} = \frac{\Omega_n^2 r}{4\pi L^2}\sqrt{\frac{E}{\rho}} \tag{2.2.3}$$

Here $\Omega_n, n = 1, 2, 3, ...$, are ordered $\Omega_j > \Omega_i$ if $j > i$ solutions of the characteristic equation $cos\Omega_n cosh\Omega_n + 1 = 0$, and we have taken into account the dependencies of the cylinder beam cross-section S and its inertia moment I on the radius $r = d/2 = 62.5\mu m$. Using the known values $\Omega_1 = 1.88, \Omega_2 = 4.69, \Omega_3 = 7.13$ [98] we see that the probe resonantly oscillates at the TF working frequency $32768Hz$ if the lengths of the freestanding part of the probe are equal to 1.7, 4.3 and $6.6mm$ respectively for the first, second and third resonances. For our proprietary so called “double resonant” montage of the SNOM probe onto TF, the exact coincidence of the working frequency of the latter with the second resonant frequency of the fiber probe beam is realized [27, 28]. Thus it leads to the small acting forces and giving possibilities to excellent spatial resolution in the topography channel.

In Figure 2.3, we present the simulation results pertinent to the first and second resonance modes of the fiber probe dithering. These graphs express an idea about the level of impact of different parameters on the tapping mode efficiency (ψ was calculated from amplitudes of the oscillations in Ox and Oy for probes with different parameters according to Equation 2.2.2). The exact values of the resonant frequencies slightly depend on the parameters of the probe being close to the values of $5140Hz$ and $32768Hz$ respectively for the first and second resonances.

The main conclusion following from this simulation is the clear difference between the first and second resonances. While for the first resonance mode and the probe bending angle of $90°$, the tapping mode character of the probe’s tip motion do takes

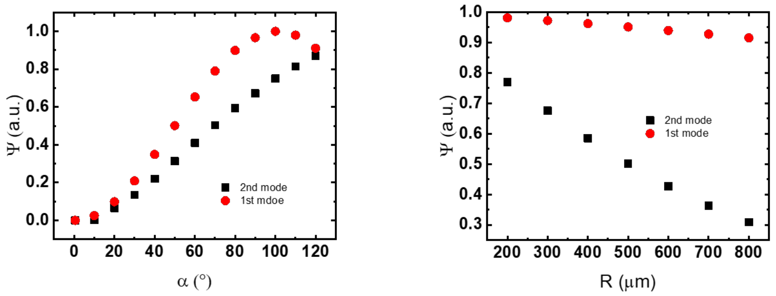

(a) Efficiency on the bending angle dependence $\psi(\alpha)$. $R \approx 300\mu m, d = 125\mu m, L = 4mm, h \approx 200\mu m.$

(b) Efficiency on the radius dependence $\psi(R)$. $\alpha \approx 90°, d = 125\mu m, L = 4mm, h \approx 200\mu m.$

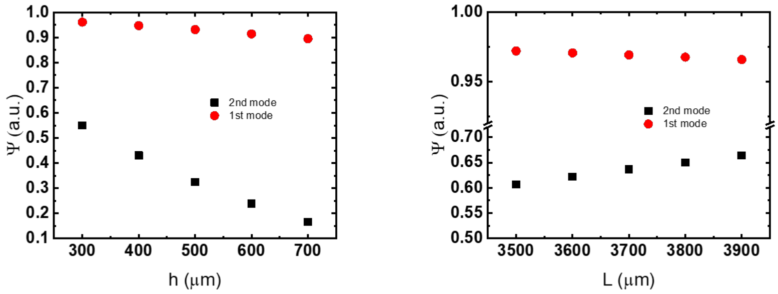

(c) Efficiency on the bending angle dependence $\psi(h)$. $\alpha \approx 90°, R \approx 300\mu m, d = 125\mu m, L = 4mm.$

(d) Efficiency on the bending angle dependence $\psi(L)$. $\alpha \approx 90°, R \approx 300\mu m, d = 125\mu m, h \approx 200\mu m.$

Figure 2.3: Simulation results for the 1^{st} and 2^{nd} resonance mode of the fiber with $125\mu m$ diameter.

place for a rather broad range of the probe parameters (as it seems intuitively evident). To achieve high tapping mode efficiency for the usually used (see above) second resonance mode, careful control of the probe's free part length h and its curvature radius R are needed. Otherwise, the shear-force type motion dominates (which looks somewhat counter-intuitive). Both these parameters should be as small as possible. The length of the probe L does not strongly affect this same efficiency. However, the varying of this length can be used to adjust the resonance frequency of the probe without seriously influencing its other characteristics. The exploitation of the third resonance mode gives the quite poor quality of the tapping mode (data are not shown in Figure 2.3), so it does not seem attractive to work in such configuration.

Indeed, the minimization of both h and R parameters is limited by the very diameter $d = 125\mu m$ of the standard glass optical fiber used to prepare SNOM probes. Moreover, such a minimization presents technical challenges already for the values are two-three times bigger than d. We succeeded to solve these challenges (see below), and in Figure 2.2, right, we present an optical image of one of the fiber probes used in the SNOM experiments reported below. Note that for our experiments we were using 2^{nd} resonance mode.

For the "state-of-the-art" fiber probe (h and R values are as small as possible, viz. $\alpha = 90°, R = 250\mu m, h = 300\mu m$), we calculated the tapping mode efficiency of the second resonance mode according to Equation 2.2.2. The computed efficiency is approximately $\psi = 0.6$: a good value certainly exceeding one half, which enables us to reasonably speak about the tapping mode for the case. But it is still far from the unity. As attested by the Figures presented, simulations show that even a small increase of the aforementioned crucial probe parameters rapidly results in ψ values well below 0.5. One cannot speak of tapping mode character of the probe motion. It can be said that, up to now this was exactly the typical situation in the field. Again, the exploitation of common non-resonance (i.e., characterized by an arbitrary and not well controlled length of the freestanding part) SNOM probe (with classical TF) cannot drastically change the situation with the tapping mode efficiency ψ. It arises from the origins of non-resonance mode - a combination of a few resonances with the main contribution from the second one.

Indeed, by varying an angle τ between the sample surface and Ox, Oy axis (Figure 2.4), the ratio of the "tapping – type" and "shear force type" motions can be changed following the simple geometrical formula, which arises from the rotation matrix,

$$\psi' = (1-\psi)[sin(\tau) - \sqrt{\frac{\psi}{1-\psi}}cos(\tau)]^2. \tag{2.2.4}$$

We illustrate this circumstance on the left of the Figure 2.4 by presenting the data pertinent for our optimized fiber probe with the parameters as above $\alpha = 90°, R = 250\mu m, h = 300\mu m$ ($\psi = 0.6$). Note, however, that the apparent increase of the tapping mode efficiency for negative rotation angles very often is only illusory and cannot be realized in practice due to geometrical limitations, see Figure 2.4 right.

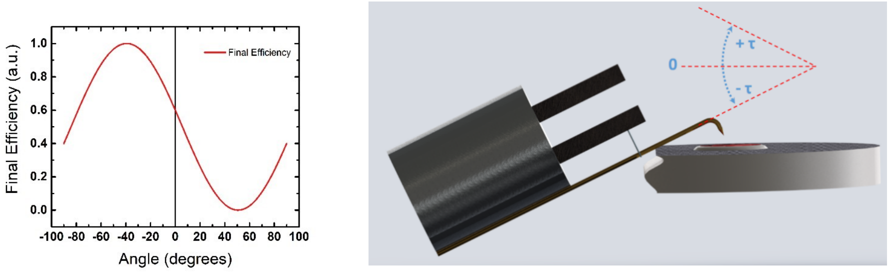

Figure 2.4: Rotation of the tip (initial $\psi = 0.6$) results in the change of the ψ factor. On the right, it can be seen the geometry of problem: bent fiber attached to the TF in double resonance condition is tilted relative to the sample. Rotation angle τ is shown in the figure. One can see that the rotation in the negative direction is limited by the very sample.

Let us now briefly analyze what is the situation with the tapping and shear-force dithering modes when the standard procedure of gluing the fiber directly on one of the TF's prongs is used. This implies the subsequent non-resonant excitation. Such approach does not preserve the initial high-quality factor of the TF electromechanical oscillations, its value diminishes typically down to $\sim 300 - 500$ and often even lower, leading to essentially larger acting forces. It is well known that at conditions of non-resonant excitation of a beam at a frequency ω, the shape of the dithered beam ("deflection curve") is given by the weighted sum of the shapes of the corresponding n-th normal modes of vibration of the beam. In our case, these are the modes pertinent to the dithering of a rod whose one end is hinged and the another is free. The relative weights of the corresponding contributions are proportional to $|\omega^2 - \omega_n^2|^{-1}$, see, e.g. [98]. Indeed, any system having distributed mass and elasticity can be described in this way. Using formula Equation 2.2.3 with the known ratio $\omega_2/\omega_1 = \Omega_2^2/\Omega_1^2 = 6.22$, we immediately see that a severe caution should be paid to the length L of the fiber beam if one wants to realize a tapping mode probe-sample interaction. This situation is illustrated in Figure 2.5: for the values of L smaller than $L = 3mm$, the contribution of the first resonance mode dominates. However, already for this length, the second resonance contributes already for roughly one-third of the total amplitude of a dithering. The contribution of the first resonance mode rapidly becomes negligible for larger values of L. Taking into account the aforementioned performance of the second dithering mode, it can be said that often the claimed tapping mode character of the bent fiber probe dithering is not at all such one. In reality, the usability of the probe with the length L less than $3mm$ is severely limited because of the difficulties to work with short probes.

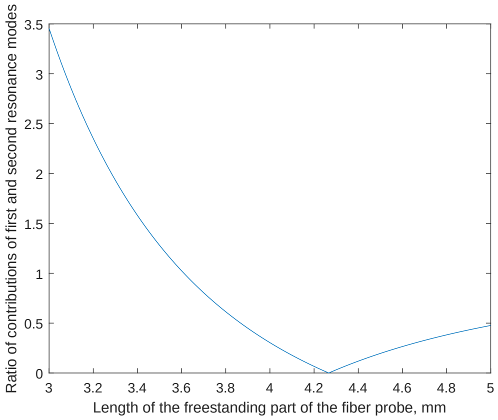

Figure 2.5: The ratio of the contributions of the first and second resonance vibration modes of the fiber probe beam (factor $\frac{|\omega^2 - \omega_2^2|^{-1}}{|\omega^2 - \omega_1^2|^{-1}}$) to the amplitude of the dithering of the probe as a function of the length of the freestanding part of the beam when excited at $32768Hz$.

At the same time, one should keep in mind that with decreasing values of the length

L and keeping a relatively long probe's free part after the bending section h, a new resonance mode will come into play. We studied the most popular scheme of the bent fiber attached to the TF in non-resonant conditions (see Figure 2.6 left, similar parameters of bending were used in [94]). Such a rush method of fiber bending and attaching to the TF can lead to the reduced tapping mode efficiency due to the mode excitation on the probe's free part (see Figure 2.6 Right). The oscillations happen mostly in the Oy direction; the ψ value for this mode is less than 0.05. Additionally, the longer the probe's free part is, the worse the tapping mode efficiency is. In order to improve ψ, short fiber tips should be used, namely, R and h values should be rather small to achieve a true tapping dithering.

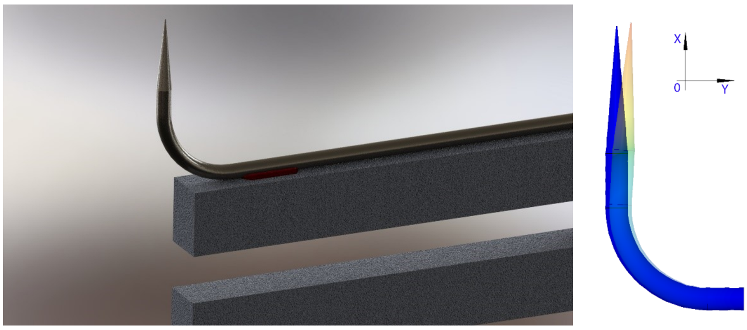

Figure 2.6: Illustrating the typical probe using non-resonant excitation scheme. On the left, the model of such a scheme, here $\alpha = 90°, R = 500\mu m, d = 125\mu m, l = 200\mu m, h = 800\mu m$. On the right, dominant oscillation mode $36kHz, \psi < 0.05$

Finally, let us note that a similar numerical analysis of the standard AFM probes reveals a truly tapping mode character of interaction there: the factor ψ is 0.95 and even more for the case for the first resonance [†]. At the same time, for the most AFM setups the cantilever is tilted by $10 - 15°$ in respect to the normal to the sample surface and leads to the drop of the factor ψ down to ca. 0.75 making it comparable

---

[†] A cantilever $0.5 - 5\mu m$ thick, $50 - 200\mu m$ long and $20 - 50\mu m$ in width rectangular beams with a $10 - 30\mu m$ microns-long pyramid tip "elastically" attached to them is taken as a standard. The whole probe is considered as made from one initially intact piece of material without any gluing.

to the optimized bent SNOM probes discussed below and working in the second resonance mode. Furthermore, for the case of ultrashort cantilevers ($10\mu m$ long) the tapping mode efficiency will be noticeably smaller, especially in multi-frequency (MF) excitation mode. Thus, the cantilevers behavior in MF-AFM regime will be different instead of taken for granted oscillation normal to the surface.

2.3 PREPARATION OF THE BENT GLASS FIBER PROBES

Bent optical fiber-made SNOM probes were prepared as follows. Single-mode glass optical fibers FS-SN-3224 from 3M (Maplewood, MN, United States) with $125\mu m$ diameter were dipped into a ca. 40% HF water solution with vacuum oil overlayer without stripping the polymer coating (so-called tube etching method [24]) and etched for 120 minutes. After the etching, the polymer coating was dissolved in hot concentrated H_2SO_4. The temperature of HF solution was carefully controlled and was maintained at 35 ± 0.05°C.

The bending of the sharpened fibers occurs under the effect of a focused CO_2 laser irradiation that locally heats the quartz nearby the tip up to the melting point. The tip of the fiber is pushed towards the laser beam due to the surface tension forces arising in the area facing the beam where quartz melts faster than on the opposite side. By changing the power of the incident laser radiation and the size of the focal spot, it is possible to control the bending radius and angle.

Next stage of the probe preparation consists in the fabrication of the subwavelength-size aperture for the light transmission onto their apex. Different attempts to realize a known shadow coating procedure [19, 99] for this purpose were undertaken, but they all failed due to the much more complex geometry of our probe in comparison with the straight one. Therefore, the blind metal coating was used together with the subsequent opening of the subwavelength aperture using Focused Ion Beam milling technique; see Figure 2.7a for the SEM image of the metal-coated fiber and Figure 2.7b for the close-up of the very apex of the coated fiber. For the coating, an aluminum layer of $150nm$ thickness was deposited exploiting Alliance-Concept EVA 760 e-beam evaporator. In few cases, the preparation of the subwavelength aperture by simple intensive scratching of the initially obstructed metal-coated probe over an appropriate sufficiently "rigid" sample (e.g., a glass slide) has been used.

The finished bent SNOM probes were glued onto the quartz tuning fork in the double resonant conditions following the procedure outlined on page 37 . To match resonant frequencies of TF and fiber we used following parameters: $L = 3.8 \pm 0.1mm, \alpha = 90°, R = 250\mu m, h = 300\mu m$. The driving rod connecting the probe with one of the TF's prongs should be glued at ca. $2mm$ distance from the fiber hinging point. For illustration, in Figure 2.7c we present a typical Amplitude Frequency Characteristic of the bent fiber attached to the TF in double resonance conditions (the Q-factor is approximately 4300) together with the SEM images of the probe tip.

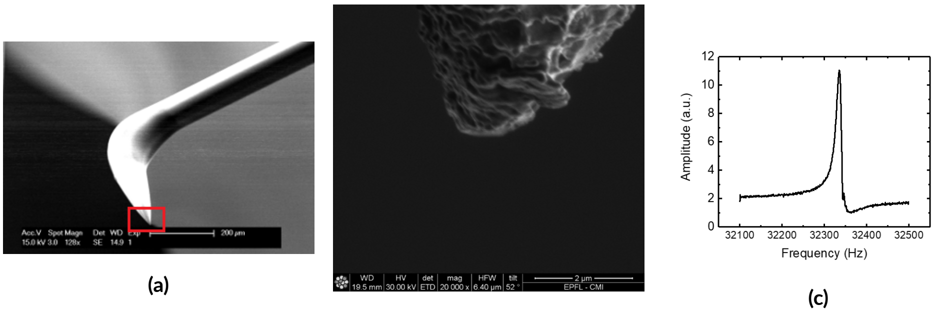

(a)

(b)

(c)

Figure 2.7: 2.7a SEM image of the Al-coated bent fiber tip. 2.7b SEM image of the tip apex marked with a red frame on the Figure 2.7a. 2.7c Amplitude Frequency Characteristic of the bent fiber probe attached to the TF.

2.4 CONCLUSION

We have presented the truly tapping mode Scanning Near-field Optical Microscopy with single-mode glass optical fiber - made bent probes. Extensive numerical simulations enabled to clarify the conditions necessary to achieve a tapping rather than shear force probe-sample interaction and also to quantify the level of tapping mode by the ψ parameter. Based on these simulations, we prepared such probes to be tested in a real SNOM microscope. Tapping mode efficiency of our probes, working in the conditions of second resonance dithering mode, lies in the range $0.6 - 0.7$, which is not too far from the AFM cantilevers efficiency in the case of a standard setting. It is essential to mention that bent optical fiber-based SNOM probes prepared without taking into account the above simulation results indeed often cannot be considered as working in tapping mode.

It was shown [100] that tapping mode SNOM is preferable in studies of soft biological samples. Furthermore, it can operate in liquids with much better performance [95]. Due to the use of our proprietary double-resonant montage of these bent probes onto the tuning fork [27, 28], similarly small acting interaction forces, lying in a few nano-, or even sub nano-Newton range, were achieved. This paves the way to use them for the imaging of fragile biological samples and future work in liquid.

This chapter is mainly based on the following article:

Smirnov, A., V. M. Yasinskii, D. S. Filimonenko, E. Rostova, G. Dietler, and S. K. Sekatskii. "True Tapping Mode Scanning Near-Field Optical Microscopy with Bent Glass Fiber Probes." Scanning 2018 (2018).

Personal contribution: designing and performing simulations of probe's motion; testing of the bent probes; writing and discussion.

3

Long-life plastic optical fiber probes for scanning near-field optical microscope

Nowadays, sharpened glass fiber probes attached to a quartz TF and exploiting the shear force – based feedback are by far the most popular in the field of SNOM. However, these probes are expensive, very fragile and their fabrication is difficult, hard to control and in many cases a hazardous process.

Here we are presenting the first SNOM probes made from plastic optical fibers with a small, submicron size, core diameter and glass-like optical properties.

3.1 1^{st} GENERATION POF

A few years ago, we presented [101] the first SNOM probes made from PMMA optical fibers (A.R.T. Photonics GmbH, Germany) with an initial nominal diameter of $250\mu m$ (with the $200\mu m$ core), generally used for the so-called side illumination purposes.

To prepare sharp tips a two-stages etching procedure was used. In the first stage, the ca. 2 cm-length portion of the fiber was submerged into ethyl acetate for $30-40min$. As a result, the diameter of the fiber was halved, and the external protective polymer film coat of the fiber was destroyed. In the second stage ($20-30min$) the end part of the bare fiber was slowly submerged into the etching solution which was agitated. After etching, the tips were rinsed in de-ionised water [101]. These tips were sharp, much less fragile and of greater ease of preparation than glass made tips. However, the very design of the POF used to prepare the probes naturally limited their performance.

It is known, that multimode fibers lead to higher dispersion and attenuation of the signal in it. That means that the use of such a fiber as a SNOM probe results in a very low transmittance efficiency and significant parasitic signal. Moreover, the end of the tip is no more a dielectric waveguide but a metallic waveguide, which changes drastically the mode structure. That leads to the mods reorganization with attenuation because of the decrease of the diameter inducing a back reflected light. That leads to elimination of all modes except the HE_{11} [102]. Thus, the transmittance coefficient of a probe is determined by the ratio between the energy stored in absorbed modes to the energy of the HE_{11} mode. The energy stored in non-propagating modes is back-reflected or absorbed by the metal layer followed by its heating.

There is the so called V number which determines the fraction of the optical power in a certain mode which is confined in the fiber core [103]. For single-mode fibers, that fraction is low for low V values (e.g. below 1), and reaches $\approx 90\%$ near the single-mode cut-off at $V \approx 2.405$. This number is a dimensionless parameter and it is defined as

$$V = \frac{2\pi}{\lambda} \cdot r_{core} \cdot NA = \frac{2\pi}{\lambda} \cdot r_{core} \cdot \sqrt{n_{core}^2 - n_{cladding}^2}, \qquad (3.1.1)$$

where λ is the vacuum wavelength, r_{core} is the core radius, and NA is the numerical aperture. For V values below ≈ 2.405, a fiber supports only one mode per polarization direction and the mode number can be estimated as

$$M \approx \frac{V^2}{2}, \qquad (3.1.2)$$

Thus, for the 1^{st}-gen POF, we have $r_{core} = 100\mu m$, $NA = \sqrt{n_{core}^2 - n_{cladding}^2} = 0.631$ and for the $532nm$ laser $V \approx 745$ which gives us huge amount of modes according the Equation 3.1.2.

That lead us the development of 2^{nd}-gen POF.

3.2 2^{nd} GENERATION POF

In order to decrease number of allowed modes and bring the use of POF as close to commonly used SNOM single mode optical glass fibers as possible it was decided to change the POF design. We ordered the $125\mu m$ diameter fibers (specially prepared for us by Paradigm Optics Company, USA) with a polystyrene core (diameter is $0.85\mu m$, $n_{core} = 1.59$) and acrylic cladding ($n_{cladding} = 1.49$). They proved to be more easy to prepare and well capable of imaging in both channels: optical and topographical.

The etching protocol which we used earlier for PMMA fibers does not work well for the 2^{nd}-gen POF. Acid vapor coming from the etchant-air interface can result into bubbles on the tip, see Figure 3.1a. On the other hand, the fiber now is made of two different materials, and the use of pure ethyl acetate can lead to the appearance of split ends, see Figure 3.1b. This is due to the difference of dissolution rates for polystyrene and acrylic in pure ethyl acetate (EA) (in the case shown on the Figure 3.1b the core was dissolved faster).

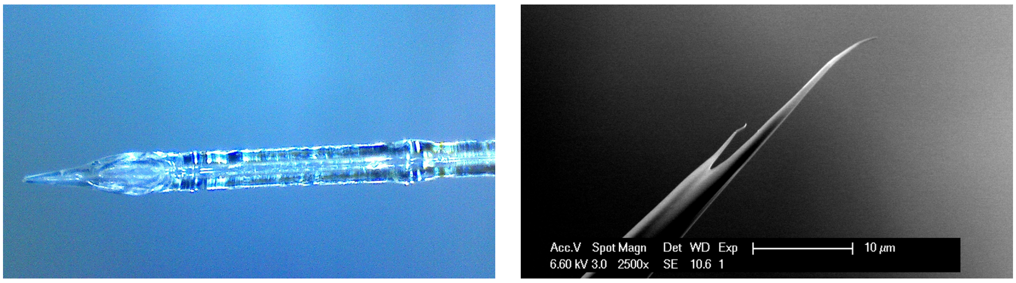

(a)

(b)

Figure 3.1: Illustration of etching defects:

(a) ”bubbles” appear due to the acid vapor coming from the etchant-air interface

(b) non-uniform etching of core and cladding can result into split ends

To avoid the aforementioned problems, we elaborated the following protocol for the POF etching. To protect fiber from acid vapor, the double-layer solution was used (see Figure 3.2). It was a 9:1 mixture of dichlormethane (DCM) and EA with water.

The mixture of DCM and EA provides nearly uniform etching. Moreover, using such an etchant results in a most significant weight loss of POF during the preparation process. The etching of the POF is a quick (tens of seconds) and self-terminating process which results in the formation of the sharp conical tip with the radius of curvature equal to $30 - 150nm$ (see Figure 3.3).

Next stage of the probe preparation consists in the fabrication of the subwavelength-size aperture for the light localization onto the apex. First, the blind

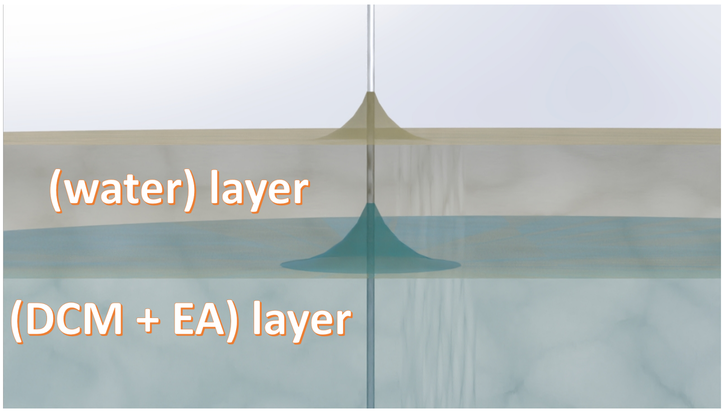

Figure 3.2: The double-layer solution representation

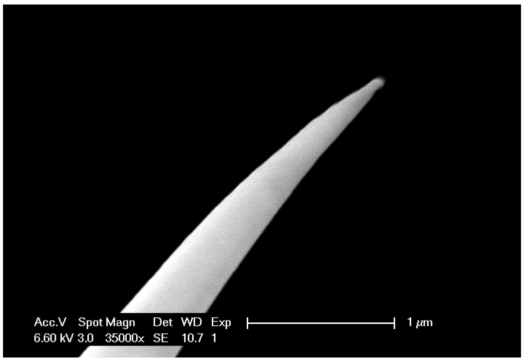

Figure 3.3: SEM image of uncoated plastic tip, curvature radius is below $50nm$.

metal coating was used together with the subsequent opening of the subwavelength aperture by virtue of the Focused Ion Beam milling technique; see Figure 3.4 for the SEM image of the metal-coated fiber. For the coating, platinum layer with $100nm$ thickness was deposited exploiting Alliance-Concept EVA 760 (Cran-Gevrier, France) e-beam evaporator. The tip prepared in such a way was good enough for SNOM, but the reproducibility of this coating procedure is not that high, and it is more expensive also due to using FIB.

As an alternative, shadow coating procedure (see page 35) can be used directly. Since we do not have proper instruments for this, we initiated colloboration with Vladimir V.

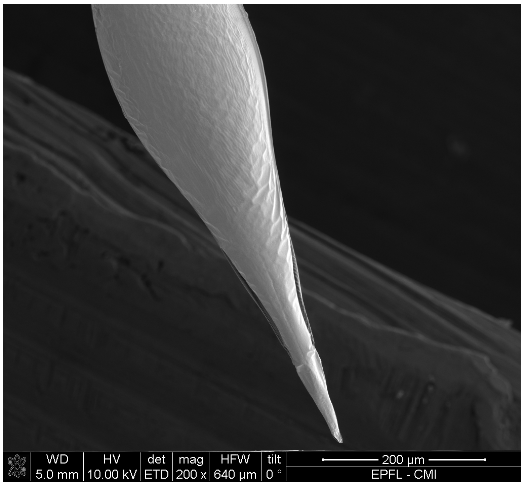

Figure 3.4: SEM image of the etched POF tip coated with Pt by the blind CVD, aperture size is more $500nm$; significant light scattering was observed from such tip.

Rogov (Institute for Physics of Microstructures, Nizhny Novgorod, Russia).

As a result, we obtained sharp metal-coated tips with a clearly visible aperture at the apex (Figure 3.5).

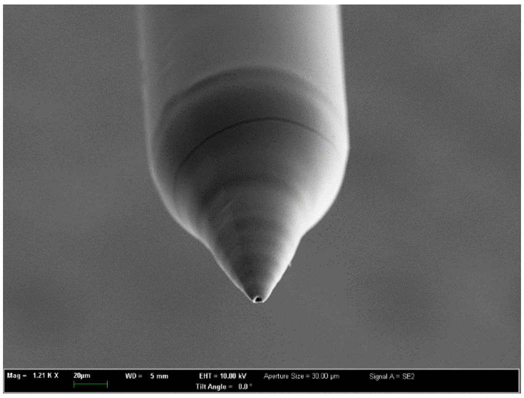

Figure 3.5: SEM image of the etched POF tip coated by the classical shadow evaporation technique.

The sharpened POF SNOM probes were glued onto the quartz TF in the double resonant conditions. To match resonant frequencies of TF and fiber, the length of a free-standing part of the fiber beam should be equal to $2.8 \pm 0.1mm$. The driving rod connecting the probe with one of the TF's prongs should be glued at $1.55mm$ distance from the fiber hinging point.

The performance of such probes is excellent but can be further improved. In particular, even these probes are durable during scanning operations, they require very careful handling. We realized that etching and coating procedure make this fiber very fragile close to the tip apex. Thus, many times fibers very simply broken just before gluing procedure by a ”wind-blow”.

To solve this problem two options were suggested: the partial alignment of the polymer chains (adjusting the tension) during the draw process of the fibers or change of material to more promising one.

3.3 3^d GENERATION POF

Taking into account all previous results, we ordered $250\mu m$ diameter fiber made of cyclo-olefin polymers (specially prepared for us by Paradigm Optics Company, USA) with Zeonex core (diameter is $0.85\mu m$, $n_{core} = 1.535$) and Zeonor cladding ($n_{cladding} = 1.528$).

The V number is estimated to be equal to ≈ 1.47 which determines it as a single mode fiber.

The huge advantage of ZEONEX Cyclo Olefin Polymer are glass-like properties. This new material proved to has an extremely low fluorescence, low birefringence, low water absorption and high optical transmission and claimed as the engineering plastic of tomorrow [104, 105].

The preparation procedure is the following. A mixture $100 : 10 : 13$ of toluene, acetone and propane was chosen as an etchant because the dissolution rate of POF in it proved to be mostly isotropic during the immersion time. The etching of the POF takes approximately 20 minutes and results in the formation of sharp conical tip with the radius of curvature equal to $50 - 150nm$. The shape of the cone can be adjusted by changing the temperature. In order to get aspect ratio corresponding to ca. $25 - 30°$ which is crucial parameter for shadow coating, we maintain the temperature during etching at the level of $18 - 19°$C. After etching, the tip should be rinsed in de-ionized water to ensure that the shape will not be affected by the etchant residuals. The resulting fiber is shown below (Figure 3.6).

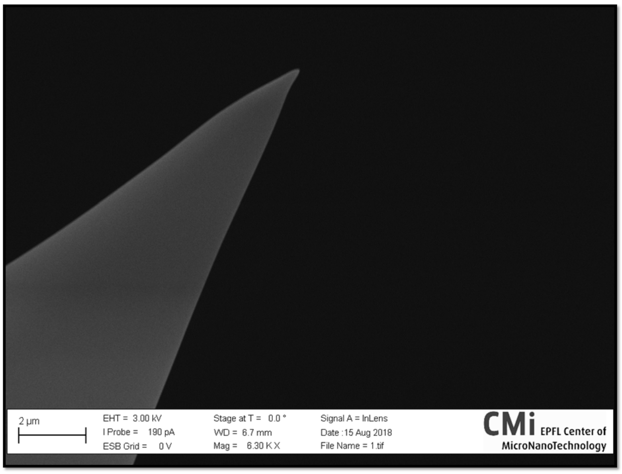

Figure 3.6: Uncoated 3^d-gen POF tip

Taking into account quality and reproducability of shadow coating technique (established for 2^{nd}-gen POF) we used the same technique. As a result we got fibers with good aperture quality (Figure 3.7) similar to those for glass made fiber.

3.4 CONCLUSION

The first SNOM probes made from submicron core-size POF and metalized by shadow coating method were demonstrated. Preparation of these probes is simple and does not require any hazardous materials or procedures.

This chapter is partly based on the following article:

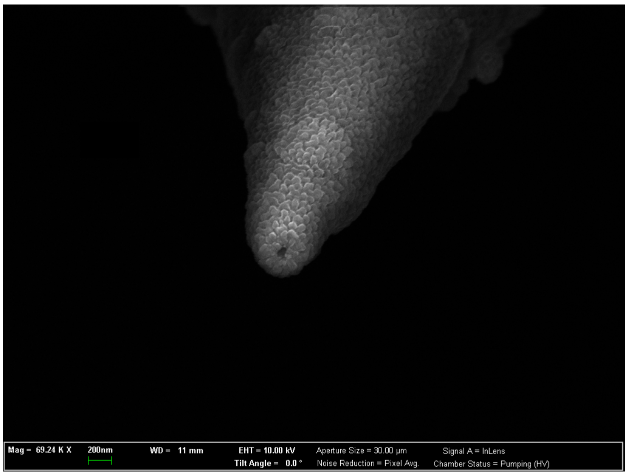

Figure 3.7: Al-coated 3^d-gen POF tip, aperture formed by shadow coating technique

Smirnov, A., E. Rostova, G. Dietler, and S. Sekatskii. "Long-life plastic optical fiber probes for scanning near-field optical microscope." In Biomedical Imaging and Sensing Conference, vol. 10711, p. 107110P. International Society for Optics and Photonics, 2018.

Personal contribution: development and realization of the method of probes preparation; testing of the POF probes; writing and discussion.

4

Scanning near-field optical microscope performance

4.1 INSTRUMENTATION

The SNOM used in our researches is a home-made device which was built few years ago [27]. This microscope is based on the inverted optical microscope Carl Zeiss Axiovert 200 (Carl Zeiss, Germany). It is designed mainly for the illumination mode operation which allows high sensitivity. The SNOM head consists of several key elements typical for almost all modern SNOMs:

- XY scanning system

- Z-distance piezo-positioner
- Topography sensor and preamplifier

Our microscope (Figure 4.1) is capable of fast and precise scanning. The main tools allowing this is the use of sensor utilizing double-resonance conditions (described in subsection 0.4.4). It provides very high quality factor enabling extreme force sensitivity.

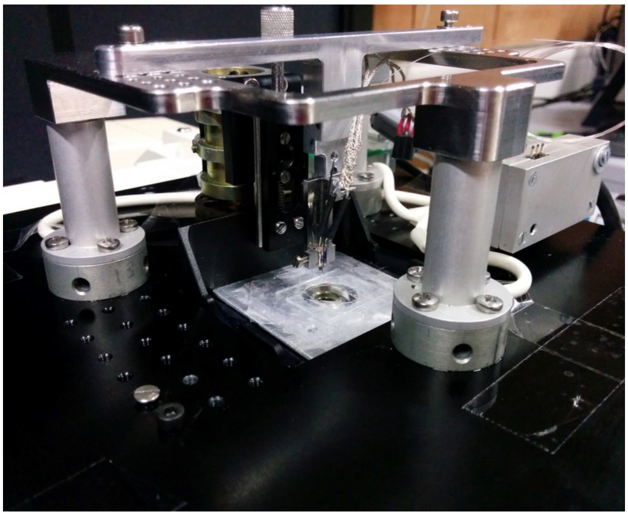

Figure 4.1: Old SNOM scanning design

The original setup presented on the Figure 4.1, had some limitations. The XY scanning is realized for the tip instead of a sample which gives not a consistent position of a light source relative to the collecting objective. Next, Z-position displacement system was based on a single piezo-tube, thus to realize coarse Z-movement the sample carriage was not fixed rigidly but held by friction on the border with sliding. For the time of construction, that system was quite efficient, but it is an unforgiving instrument. A little displacement could ruin the tip and the sample.

Having this in mind, we decided to modify the existing system, see Figure 4.2 (or Figure 3 for the model). First of all, we changed Z-scanning system. We put a modern scanner $ECSx3050$ (attocube systems AG, Germany) with sub-nm fine positioning and $30mm$ coarse travel range. It allows us to safely swap XY scanning part from the tip to the sample. As an addition, we built up XY-positioning for the tip (using linear mechanical stages). Since the original scanner was realized using piezo-tube, it utilized high voltage ($500 - 1000V$) and had a small capacitance (tens of nF) — these parameters allowed to use low-power HV-amplifier. The scanner we used for modernization has much higher capacitance (hundreds of nF) which means it requires more powerful voltage generator. Thus, we used $ENV800$ amplifier module (piezosystem jena GmbH, Germany) to operate with the Z-distance control signal.

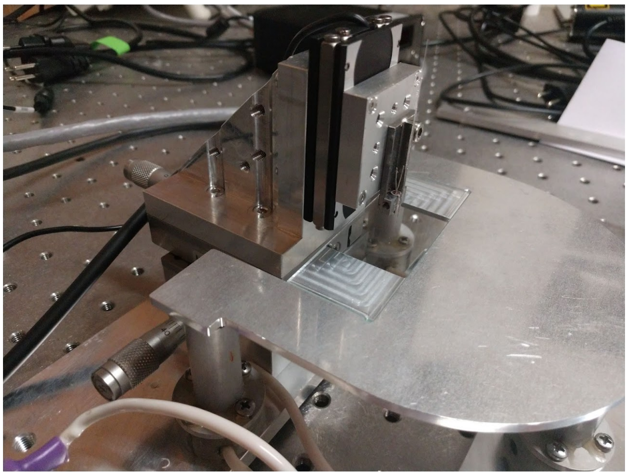

Figure 4.2: New SNOM scanning design

The essential part of any newly developed device is its performance properties. For the new SNOM probes, we test them on reference samples. Properties such as:

- lateral performance in topography channel
- spatial performance in topography channel
- optical performance in near-field mode

- probe light collection efficiency

can be quantitatively determined. Example of samples are calibrating gratings, bio-samples like DNA and others. The probes were prepared according to the procedures outlined in section 2.3 for the bent fiber tapping mode probes; in section 3.2 for the 2^{nd} generation POF and section 3.3 for the 3^{d} generation POF.

4.2 Topography tests

The performance of the aperture SNOM probes has been assessed exploiting them as probes of the slightly modernized customarily made Scanning Near-Field Optical Microscope. The main tool to achieve high sensitivity in topography channel is the use of an original "double resonance principle", see page 37. The use of proprietary low noise, precise and fast electronics measuring the resonance frequency f_{res} and Q-factor of a tuning fork is also important. The double resonant montage enables to routinely achieve the quality factor of the sensor ranging $3500-5500$, and its exploitation results in the force sensitivity as small as $30pN$ in a bandwidth of $300Hz$. All the images presented in this section were obtained in constant $Q-$factor mode.

In Figure 4.3, we present the topographical image of $677-AFM$ calibrating grating, $2000 lines/mm$ (Ted Pella, Redding, CA, USA) obtained exploiting bent fiber probes.

In Figure 4.4, we present the shear force topographical image of the TGX01 calibrating grating (NT-MDT, Zelenograd, Russia) obtained using 2^{nd}-gen POF.

As a more severe test, mica samples containing densely deposited DNA molecules onto $APTES^{*}$-modified surface, see, e.g. [106] for preparation details and AFM images, were used, see Figure 4.5.

---

[*] (3-Aminopropyl)triethoxysilane (APTES) is an aminosilane frequently used in the process of silanization, the functionalization of surfaces with alkoxysilane molecules. It can also be used for co-

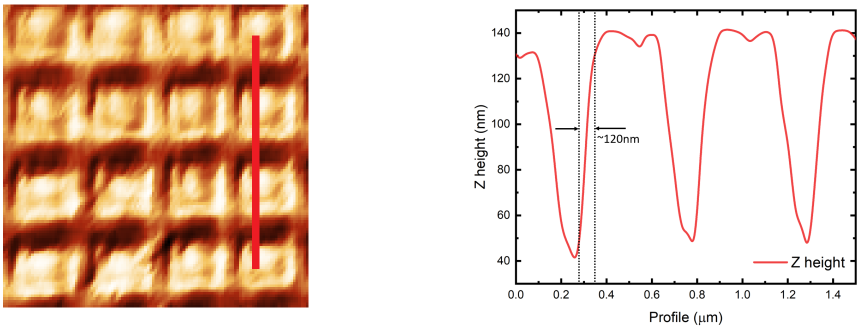

(a)

(b)

Figure 4.3:

(a) The topography of the calibrating grating $2000 lines/mm, 2.0\mu m \times 2.0\mu m$. The image was obtained in constant $Q-$factor mode using bent fiber probe.

(b) The cross-section profile from the left image along the red line

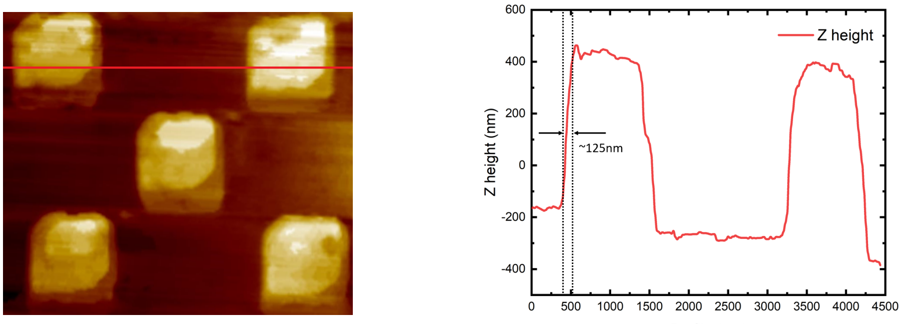

(a)

(b)

Figure 4.4:

(a) The shear-force image of the TGX01 calibrating grating. The image is presented without any filtering and scanner non-linearity compensation and was obtained using 2^{nd}-gen POF probe. Scan size $4.5 \times 4.5 \mu m$.

(b) The cross-section profile from the left image along the red line

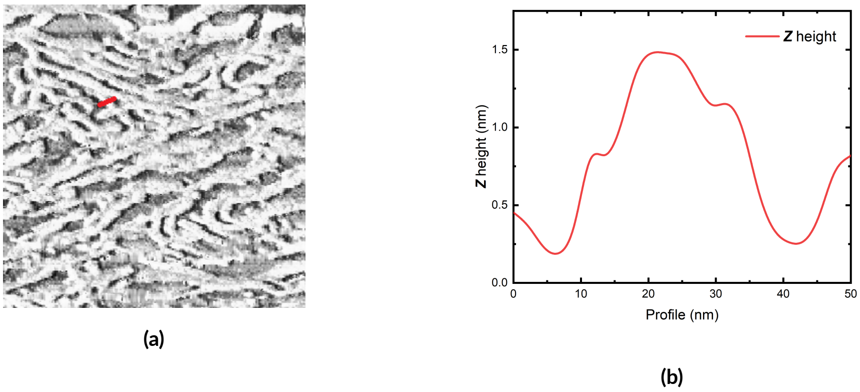

(a)

(b)

Figure 4.5:

(a) The topography image of the close-packed Phi X 174 DNA, $0.7\mu m \times 0.7\mu m$ obtained using bent fiber probe.

(b) The cross-section profile from the left image along the red line

To test the 2^{nd}-gen POF we also used mica samples containing amyloid fibrils deposited onto the surface (see [107, 108] for preparation details), see Figure 4.6.

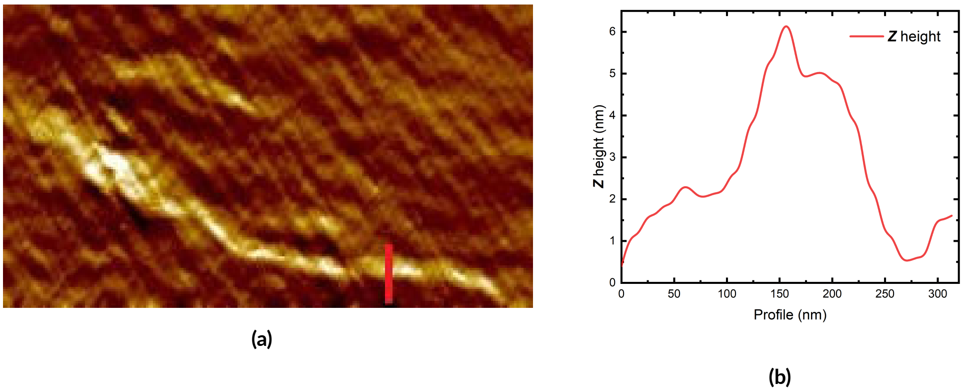

(a)

(b)

Figure 4.6:

(a) The shear-force image of the amyloid fibrils deposited on the mica surface obtained using 2^{nd}-gen POF probe. Scan size $4 \times 2\mu m$.

(b) The cross-section profile from the left image along the red line

The images obtained via 2^{nd}-gen POF presented above were recorded using the tip

---

valent attaching of organic films to metal oxides such as silica and titania which earlier has touched the surface few times. Note that it would be nearly impossible to continue work with glass tips if it would touch something. This fact is one of the direct evidences of POF tips durability.

The lateral resolution can be estimated as the elongation of the edge on the feature. In our cases the elongation was smaller than the pixel size. Thus the resolution is estimated to be not lower than $16nm$ for the bent fiber probes and not lower than $5nm$ for POF probes.

4.3 OPTICAL CHANNEL PERFORMANCE

To the large extent, the near-field performance of any probes can be verified using standard calibrating grating $SNG01$ - rhomb vanadium islands $15 - 30nm$ thick on the quartz substrate (NT-MDT, Zelenograd, Russia) giving the transmission through coating (rhombs) $< 20\%$, UV image of such sample can be found in [109].

To test optical performance, we conducted experiments in illumination mode using the pulsed laser ($\lambda = 532nm$, the repetition rate for all experiments below was equal to $5kHz$) as the light source. The transmitted light was collected via micro-objective ($40x$, $NA = 0.65$) and detected with a photomultiplier tube (dark count rate $< 10cps$).

The image obtained exploiting tapping mode bent probes is presented in Figure 4.7. Since the aperture was formed by a collision of the tip with the rigid surface (quartz plate), it has low resolution $\sim 500nm$.

The optical performance of POF tips is shown below.

For the 2^{nd}-gen POF, see Figure 4.8, it is possible to see some dust particles at the topography image. However these objects are completely transparent in an optical channel, which means there is no crosstalk between topographical and optical channels.

The relatively low (for SNOM) resolution, $170nm$, is most likely due to not clearly

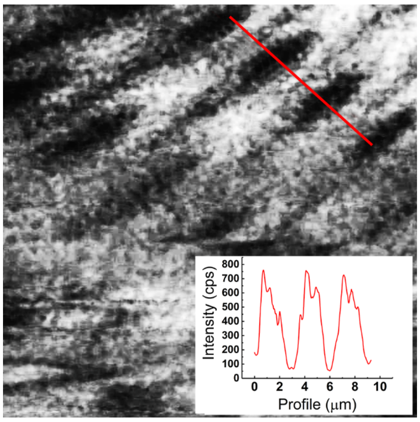

Figure 4.7: The optical image ($20\mu m \times 20\mu m$) of the $SNG01$ SNOM calibrating grating – Rhomb vanadium islands $20-30nm$ in thick on the quartz substrate (NT-MDT, Zelenograd, Russia) obtained in transmission mode using bent fiber probe; cross-section along the red line is shown on the bottom.

formed aperture.

The next, use of the 3^d-gen POF fibers results in better performance, see Figure 4.9.

The resolution is estimated to be $\sim 75nm$, which is comparable with standard glass fiber probes. At the same time the image has better contrast.

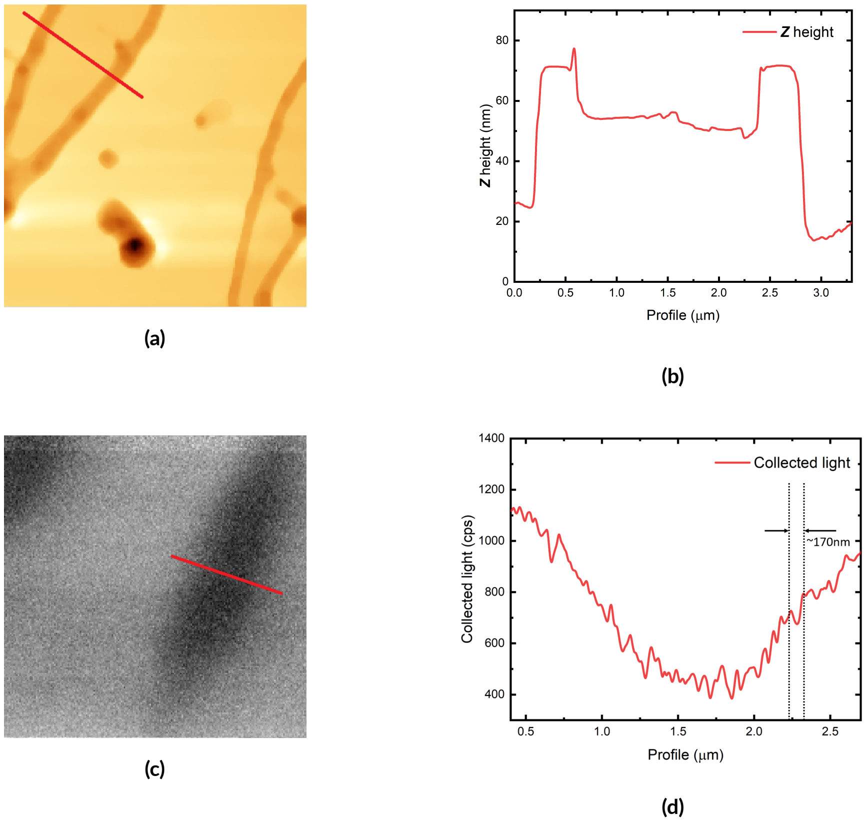

(a)

(b)

(c)

(d)

Figure 4.8:

(a) The shear-force image of the SNG01 (NT-MDT, Zelenograd, Russia) calibrating grating. The image is presented without any filtering and scanner non-linearity compensation.

(b) The cross-section profile from the image (a) along the red line

(c) The near-field optical image of the SNG01 calibrating grating.

(d) The cross-section profile from the image (c) along the red line

2^{nd}-gen POF probe. Scan size $6 \times 6\mu m$. The resolution is estimated to be $\sim 170nm$.

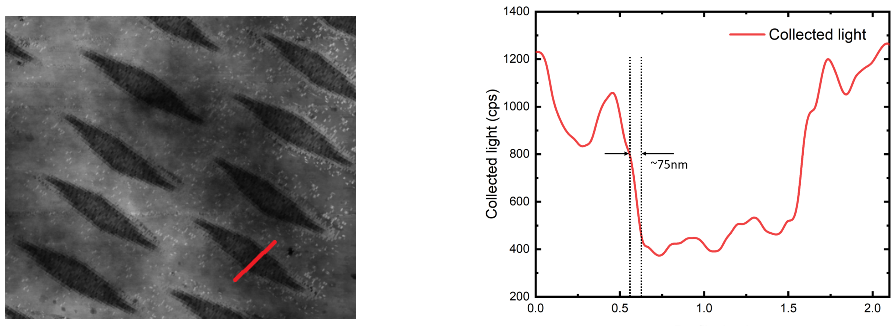

(a)

(b)

Figure 4.9:

(a) The near-field optical image of the SNG01 calibrating grating.

(b) The cross-section profile from the left image along the red line.

3^{nd}-gen POF probe. Scan size $14 \times 12\mu m$. The resolution is estimated to be $\sim 75nm$.

4.4 SNOM COLLECTION MODE

To test probes collection efficiency, we used optical near-field created by frustrated total internal reflection using an auxiliary right angle prism. Such a configuration allows to avoid the use of metal coated tips, what can be useful specially for bent fiber probes.

Taking into account the rising interest to surface wave-mediated sensors and plasmonic devices we attempted to study the propagation of surface electromagnetic waves inside the surface waveguides supported by a PC structure. Together with the group of Sergei Popov (Royal Institute of Technology, Sweden), we designed and developed several types of waveguides: bent waveguide (constant $90°$ angle, variation on the bending radius from $1\mu m$ to $150\mu m$), Y-splitter (variation on the angle from $4°$ to $150\,°$), symmetric $Mach - Zehnder\ interferometers$ (variation on the split angle from $4°$ to $150\,°$) and asymetric $Mach - Zehnder\ interferometers$ (variation on the split angle from $2 + 5°$ to $2 + 45\,°$). The waveguides were made of $SU8$ polymer and had initial width equal to $10\mu m$ and the height equal to $320nm$.

The supporting PC was designed for $p-$polarization and consisted of 10 pairs of layers ($94.0nm$ of Ta_2O_5 / $131.1nm$ of SiO_2) deposited on fused silica plane. The calculated dispersion curve of such a structure with $135nm$ $SU8$ polymer on it is shown on Figure 4.11. To launch the surface electromagnetic waves we used a standard $He - Ne$ laser ($\lambda = 632.8nm$).

Mainly we were interested in the field distribution close to the splitting point. However, our setup is not suitable for this studies due to small scanning ranges ($40 \times 40\mu m$ at maximum), where only the width of the waveguides was $10\mu m$. The results can be seen below (Figure 4.12).

Apart the problems with the search of structures, we realized that system should be

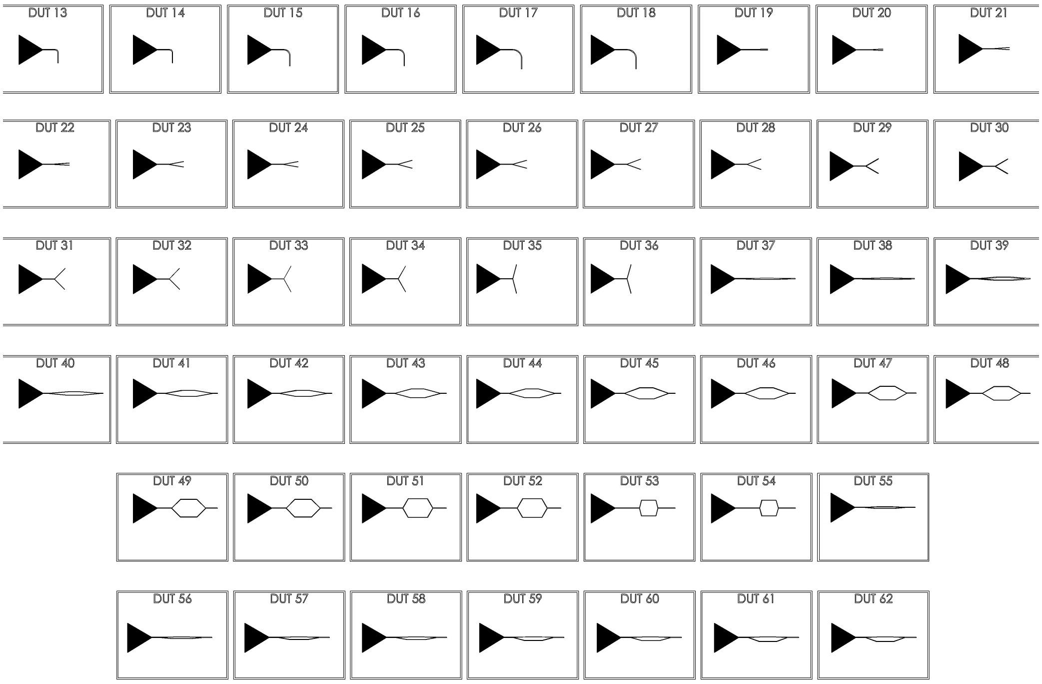

Figure 4.10: The illustration of waveguide structure supported by PC.

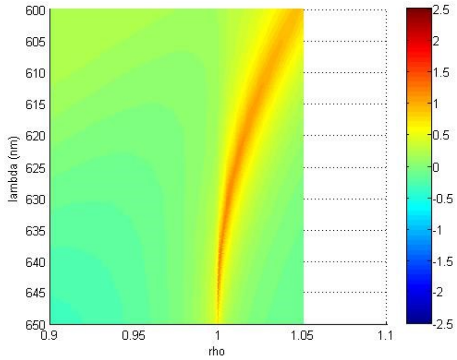

Figure 4.11: The dispersion curve of the structure for surface electromagnetic waves studies. $Z-$bar corresponds to the efficiency of surface waves excitation

much more carefully prepared in comparison to our approach. On the Figure 4.12a one can see the topography defects which results in relatively poor waveguide quality. The Figure 4.12b is only one area on which we succeeded to collect near-field signal, many others consist mostly from noise.

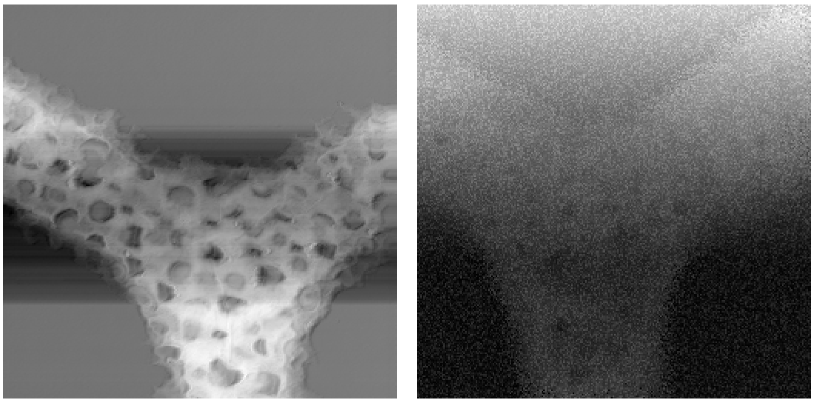

(a) The topography of the node of the Y-splitter in the waveguide

(b) The near-field distribution in the node of the Y-splitter in the waveguide

Figure 4.12: The images were obtained using bent fiber probe. Scan size $10 \times 10\mu m$.

The initial idea brought us to the development of a fine structure able to support surface electromagnetic waves and study them (e.g. propagation length of surface modes can be studied).

4.5 CONCLUSION

We tested bent fiber probes prepared in accordance to the simulations (see page 71). The small acting forces allow to image not only calibration gratings but also mica-deposited DNA molecules.

POF probes do demonstrate quite high "durability" during the exploitation. The images presented in this chapter (Figure 4.4, Figure 4.6 and Figure 4.8) were obtained exploiting the probes, which already have touched the surface a few times.

This chapter is partly based on the following articles:

Smirnov, A., V. M. Yasinskii, D. S. Filimonenko, E. Rostova, G. Dietler, and S. K. Sekatskii. "True Tapping Mode Scanning Near-Field Optical Microscopy with Bent Glass Fiber Probes." Scanning 2018 (2018).

Personal contribution: designing and performing simulations of probe's motion; testing of the bent probes; writing and discussion.

Smirnov, A., E. Rostova, G. Dietler, and S. Sekatskii. "Long-life plastic optical fiber probes for scanning near-field optical microscope." In Biomedical Imaging and Sensing Conference, vol. 10711, p. 107110P. International Society for Optics and Photonics, 2018.

Personal contribution: development and realization of the method of probes preparation; testing of the POF probes; writing and discussion.

5

Long-range surface plasmon-polaritons propagating along silver nanofilms

Starting from the early 20^{th} century researchers are interested in surface electromagnetic waves. Naturally, such waves are very sensitive to the surface defects and that gave rise to bio- and chemical-sensing systems.

In particular, surface electromagnetic waves without any metal layer supported by PC has numerous implications in sensorics, electromagnetic field control at the surface and so forth ([110–118]). Any devices exploiting properties of electromagnetic surface waves requires supporting structure having exceptional quality. Earlier, it was shown that a specially designed PC [119] enabled the launch and use of surface plasmons (in the red spectral region) for such "non-plasmonic" materials as palladium [120–122] and cobalt [123], as well as launch and use blue (at $405nm$ [124]) surface plasmons for gold.

Here, we report the realization of PC-supported long-range surface plasmons for silver at the red wavelength of He-Ne laser, $\lambda = 632.8nm$. Quite narrow plasmon resonances, attesting the ultralong SPP propagation and high quality of silver films, were observed. From one point of view, silver is always considered as the best surface plasmon-supporting metal in the red and near-infrared spectral ranges. However, from another point of view, the difficulties in the preparation of high-quality thin layers of silver and rapid degradation of this material exposed to the atmosphere make its exploitation quite tricky. To the best of our knowledge, up to date LRSPP with thin silver nanofilms have been realized only with the (almost) symmetrical sandwich structures composed of silica and (very) thick layers of an index matching oil or polymer [125, 126], so that their exploitation as sensors seems not possible., see further references therein.

5.1 PHOTON CRYSTAL DESIGN

The following structure (see Figure 5.1) has been designed and prepared to realize LRSPP propagation along $silver - ZnS/air$ interface: $SiO_2/(HL)^{19}/Al_2O_3/ZnS(1)/Ag/ZnS(2)/air$, where SiO_2 are standard

$2.3mm$ thick fused silica plate, $(HL)^{19}$ are 19 pairs of tantalum pentoxide and silicon dioxide layers (that is transparent dielectrics having high and low refraction indices which form a $1D$ PC) with the thicknesses respectively 96.6 and $134.4nm$, Al_2O_3 layer has a thickness of $20nm$, ZnS layers 1 and 2 have the thicknesses respectively 52 and $20nm$, Ag is $12.5nm-$thick silver layer. $SiO_2/(HL)^{19}$ PC on silica substrate has been prepared by magnetron sputtering in one coating run, and afterward all other layers have been deposited on top of this finished structure also in one (but another) coating run.

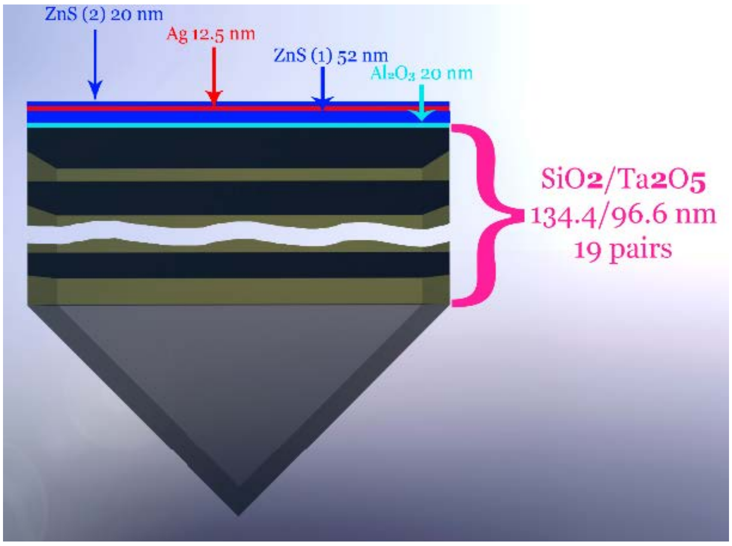

Figure 5.1: 1D PC-based structure, supporting LRSPP propagation along $silver/ZnS/air$ interface.

Through extensive experimentation with ultrathin (sub$-15nm$) Ag layers deposited by either thermal evaporation or sputtering, we have found that one possible solution to improve the thin layer morphology (preventing island-type growth) was to carefully select the underlying layer chemistry, and established that ZnS sublayers (substrate layers for Ag) led consistently to improving the layer morphology. In particular, the near-infrared (IR) reflection/transmission (R/T) spectra of custom-designed low-emissivity multilayer coatings employing them have been systematically studied. It is well-known that when the morphology of layers is compromised (island growth with holes in-between takes place), this unavoidably leads to the insufficient reflection of near-IR light by these layers and the coatings based on them. Only if the R/T spectra of multilayer coatings employing at least two Ag layers of thickness below $15nm$ are fitted very closely with the spectra predicted using the data pertinent for idealized Ag layers (bulk n and k data), we could conclude that the morphology of growth is close to an ideal one. Exactly such a situation takes place in practice, which allows us to claim the quality of ultrathin silver layers when ZnS substrate layer was used. A thickness of $12.5nm$ for the silver layer has been selected as the minimal thickness for which, accroding to our expirience, high-quality of the film is achieved.

For the principles of optimal PC design see [127]. The thicknesses of H and L layers forming PC were selected following the procedure optimizing the extinction per unit length (for a given wavelength and external media, of course), the thickness of the $ZnS(2)$ layer of $d_{ZnS_2} = 20nm$ was selected as "the smallest sufficient" to protect the silver layer from atmosphere. Al_2O_3 layer (of again the smallest reasonable thickness) was used to improve the quality and adhesion of the first $ZnS(1)$ layer. Finally, we optimize the thickness of this same first internal $ZnS(1)$ layer to achieve the most favorable conditions for LRSPP propagation, and optimize the number of pairs of layers in PC to have the maximal amplification of the light wave on the silver$-ZnS$ interface.

An essential difference of the structure at hand in comparison with the earlier used PC supporting LRSPP propagation [119–122, 124] is the appearance of one additional protective $ZnS(2)$ layer which necessitates the following modifications. In impedance representation [127], the condition for the surface wave propagation remains the same: $Z_{left} + Z_{right} = 0$, where Z_{left} is an impedance of the system $SiO_2/(HL)^{19}/Al_2O_3/ZnS(1)/Ag$ calculated using results from [127]; Z_{right} is an impedance of the system $ZnS(2)/air$ which is equal to

$$Z_{right} = Z_{air} \cdot \frac{Z_{ZnS} - iZ_{air} \cdot tan(\alpha_{ZnS2})}{Z_{air} - iZ_{air} \cdot tan(\alpha_{ZnS2})}, \tag{5.1.1}$$

And an impedance of the infinite external media (air) equal to

$$Z_{air} = \frac{\sqrt{1 - \rho/n_{air}}}{n_{air}}, \tag{5.1.2}$$

where $Z_{ZnS} = \dfrac{\sqrt{1 - \rho/n_{ZnS}}}{n_{ZnS}}$, $\alpha_{ZnS2} = \dfrac{2\pi}{\lambda} \cdot n_{ZnS} \cdot d_{ZnS2} \cdot \sqrt{1 - (\rho/n_{ZnS})^2}$, and ρ is a “propagation parameter”, viz., an angular variable equal to $\rho = n_i sin\vartheta_i$. This variable, according to the Snell’s law, remains the same for each layer having the refraction index n_i with ϑ_i being an angle between the propagating light and the normal to all interfaces [127]. This change is not negligible and must be taken into account because already for $20nm-$thick ZnS layer with the refraction index $n_{ZnS} = 2.318$ and $r = 1.017$ we have comparable values of $a_{ZnS2} = 0.41$, $Z_{air} = 0.1285i$ and $z_{ZnS} = 0.39$. At the same time, for many practical purposes, the whole effect of this additional layer can be seen simply as a relatively slight modification of the refraction index of an infinite external medium. Comparing Equation 5.1.2 and 5.1.1 we see that for $r = 1.017$ Equation 5.1.2 gives the same impedance as Equation 5.1.1 if one put $n_{air} = n_{eff} = 1.03$ into Equation 5.1.2.

The results of our calculations are presented in Figure 5.2. It is easy to see that for $He - Ne$ laser wavelength of 632.8 nm we do have a LRSPP wave characterized by the angular variable (propagation parameter) $\rho \cong 1.02$ and possessing quite strong thirty-fold enhancement of the intensity of light.

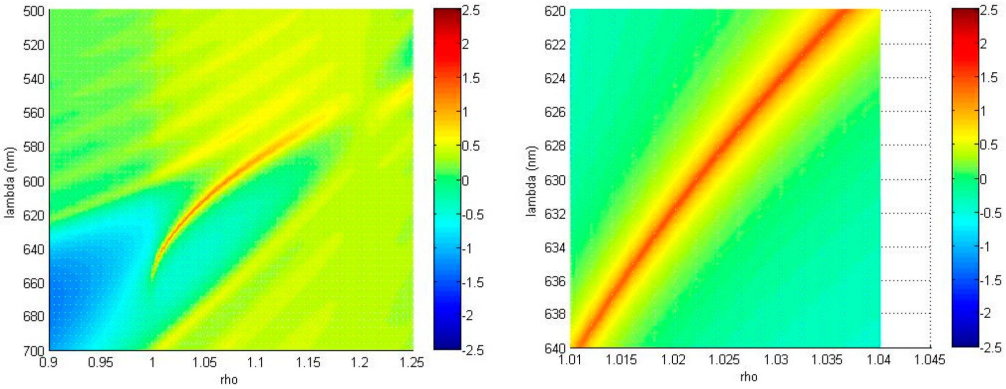

Figure 5.2: On the left, calculated dispersion of the $1D$ PC-based structure, supporting LRSPP propagation along $silver/ZnS/air$ interface is presented. Color scale presents a value of $log10(I_e/I_0)$ where I_e, I_0 are respectively the intensities of light at the interface and at the entrance of the structure. Right picture corresponds to the magnified small part of the dispersion curve.

5.2 EXPERIMENTAL RESULTS

Schematic of an experimental setup together with the data attesting an observation of very narrow angular plasmon resonance in the light reflection from the aforementioned PC + Ag layer structure are presented in Figure 5.3. For the measurements of LRSPP, standard Kretschmann configuration employing quartz right angle prism on which the structure at question has been "glued" via a droplet of phase matching oil has been used [128]. Standard p-polarized $He - Ne$ laser light (beam diameter around 5 mm) has been focused on the structure studied with $100mm$ focal length lens, and the angular structure of the reflected light has been recorded observing the light spots at distances of 1620 and/or $4050mm$ (both recordings of the light intensity with CMOS (complementary metal-oxide semiconductor) camera and processing of color digital photographs of the corresponding light spots were used leading to essentially the same results).

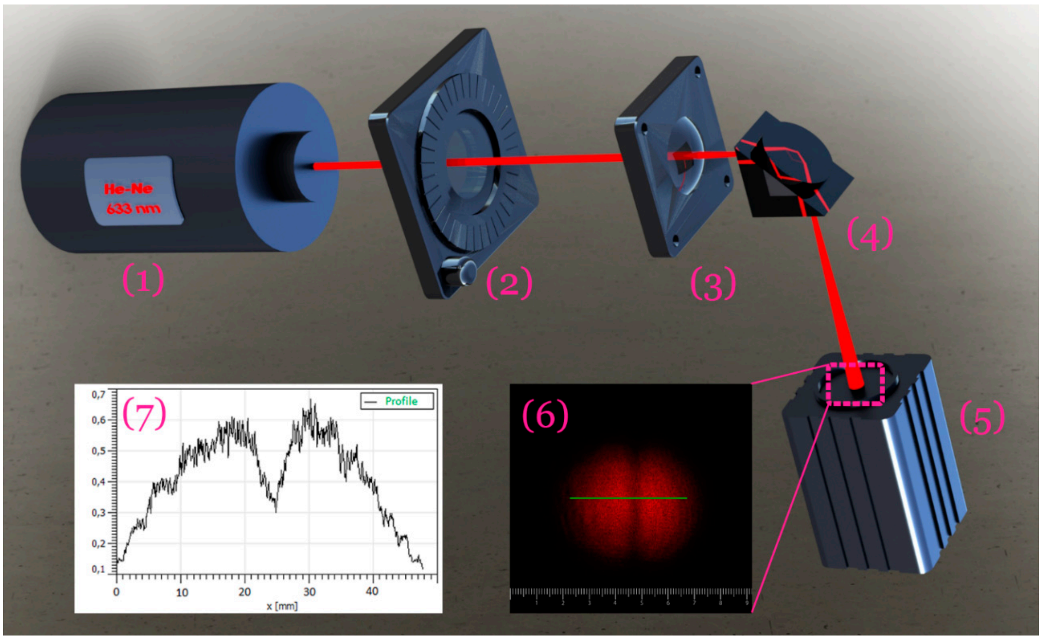

Figure 5.3: Schematic of an experimental equipment (1–5), color photograph of the reflected light spot (6) and intensity profile (7) measured at a distance of $4050mm$. (1) $He-Ne$ laser, (2) polarizer, (3) focusing lens, (4) investigated structure $SiO_2/(HL)^{19}/Al_2O_3/ZnS(1)/Ag/ZnS(2)/air$ glued to silica prism via a droplet of phase-matching oil, (5) CMOS (complementary metal-oxide semiconductor) camera.

Surface plasmon excitation has been observed for conditions quite close to the normal incidence of the incoming light beam onto the prism entrance face: the corresponding angle was equal to $0.3°$C which results in the incidence angle onto the prism hypotenuse $\vartheta = 44.80$ giving the propagation parameter $\rho = 1.04$. Deviation of this value from the theoretical one is due to the deviations of actual refraction indices and layer thicknesses from the (theoretical or "searched for") values used in calculations, and this is quite common for the field.

Another indication of the narrowness of the plasmon resonance in our structure has been obtained when we, in the same configuration, used unfocused $He-Ne$ laser beam: for an optimal adjustment, the intensity of reflected light dropped from $5.9mW$ (out of resonance) to $2.6mW$ (in resonance) thus attesting that more than one half of an incoming radiation power has been transferred into the surface wave.

The same experiment also was used to demonstrate the polarization dependence of the observed reflection minimum: the difference in the intensity of light reflected for out of- and in-resonance conditions well followed the content of the $p-$polarized light in the incoming laser beam (it was changed by the rotation of $He - Ne$ laser having the polarization ratio not smaller than $50 : 1$ without a polarizer), and such a difference was completely undetectable for the pure s-polarization case.

The width of the angular resonance curve in Figure 5.3 is equal to ca. $\Delta\vartheta_{air} = 8 \cdot 10^{-4}$which corresponds to the surface plasmon propagation length l of approximately $180\mu m$. (Standard formula $l = \dfrac{\lambda}{2\pi\Delta\vartheta_{pr}n_{pr}cos\vartheta_{pr}}$ was used. Here, the subscript pr corresponds to the values inside the prism; the value of $\Delta\vartheta_{pr}$ can be recalculated from the experimentally measured ϑ_{air} by applying Snell's law. For our case of almost normal incidence of light onto the prism catet $\Delta\vartheta_{air} \simeq n_{pr}\Delta\vartheta_{pr}$). Comparable, but slightly worse results with the angular width somewhat exceeding 10^{-3} were obtained when using a semiconductor cw fiber Bragg grating laser diode at the wavelength of $636.7nm$ (QPhotonics LLC, Ann Arbor, MI, USA). This is the main result of our research, and it unambiguously attests the first realization of LRSPP for PC-supported silver nanofilms. The long-term stability of the prepared structures was noticed: the reflection parameters remained virtually the same during nine months of observations; the sample has been kept in usual room conditions in a polyethylene packet (not hermetically sealed).

The experimentally observed value $\rho = 1.04$ enables to determine the actual distribution of the square $(EE*)$ of electric field of SPP both inside an external medium (air, for which we take the refraction index equal to unity) and PC. For the former, we have an exponential decrease with the characteristic length $lext = \dfrac{\lambda}{4\pi\sqrt{\rho^2 - 1}} \cong 180nm$, that is much larger than the thickness of the ZnS layer adjacent to the silver nanofilm. Inside the PC, we have a standing wave with an exponentially decreasing envelope e^{Kz}. The value of K can be found applying e.g.,Equation 5.1.1 of [119]. An easy calculation gives $e^{K\Lambda} = 1.163$ which corresponds, for the PC period $\Lambda = 231nm$, to the characteristic decay length of $l_{PC} \cong 1.53\mu m$. (Actually, the same value can be obtained calculating the transmission coefficient for one period of PC, se Section 2.4 of [127]). The precise field distribution inside a metal layer and, correspondingly, inside the dielectric layers immediately adjacent to it, is quite sensitive to the exact thickness of metal layer and its refraction index which define the location of the minimum of an electric field inside the nanofilm, see a detailed discussion in [119, 127].

Discussing the obtained results, we first want to note that the observed LRSPP propagation length in our silver nanofilm-based structures is quite comparable to the value of $160\mu m$ reported in [119] for LRSPP supported by a specially designed PC and ca. $5nm$-thick gold film at the wavelength of $710nm$. This is not surprising given the quite comparable "plasmonic qualities" of gold and silver at the (different) wavelengths at question: according to Palik's book [[129], at $710nm$ we have $\varepsilon_{Au} = -15.723 + 1.3413i$ which gives $Im(\sqrt{\frac{\varepsilon_{Au}}{\varepsilon_{Au}+1}}) = 0.0030i$ for the quantity describing the dissipation for SPP propagating along the interface air—infinitely thick gold layer [128]. For our case, using the experimentally measured (by our group) value of the silver refraction index for a given wavelength, $n_{Ag} = 0.1345 + 3.986i$, that is $\varepsilon_{Ag} = -15.8701 + 1.0722i$, we have $Im(\sqrt{\frac{\varepsilon_{Ag}}{\varepsilon_{Ag}+1}}) = 0.0023i$. However, one should also note more than two times smaller value of the metal layer thickness, ca. $5nm$, in experiments reported in [119]: a very important factor, given the inverse quadratic dependence of the LRSPP dissipation on this same thickness [130–132]. All this, again, should be considered as the demonstration of truly high-quality silver nanofilm in our case.

Indeed, comparable LRSPP propagation lengths have been observed also in experiments with Pd [121] and Co [123] nanofilms deposited onto the properly designed PC. The common characteristic feature here is that in all of these cases, the experimentally measured values, although are impressively large enough and much exceed the propagation lengths for simple metal—dielectric interfaces, turn out to be substantially smaller than those which could be achieved according to the theoretical predictions.

The latter can be estimated approximating the real system by a "symmetrical sandwich structure composed by an infinite medium with the refraction index n_{eff} - thin, with the thickness d_m, metal layer with the refraction index n_m - an infinite medium with the refraction index n_{eff}, using the value $n_{eff} = 1.03$ described above (varying of this value contributes to the result quite slightly). In the so called Leontovich approximation, see formula A3 from Konopsky paper [127] and other details therein, we have:

$$\frac{1}{\lambda} = \frac{1}{2\pi d_m n_m} \cdot arctan(\frac{2n_m n_{eff}^2(\rho^2 - n_{eff}^2)^{1/2}}{n_{eff}^4 + n_m^2 n_{eff}^2 - n_m^2\rho^2}). \tag{5.2.1}$$

As a function of ρ, this is a simple bi-quadratic equation

$$Q^2 n_m^4 \rho^4 - 2\rho^2(Q^2 n_m^2(n_{eff}^4 + n_m^2 n_{eff}^2) + 2n_m^2 n_{eff}^4) + Q^2(n_{eff}^4 + n_m^2 n_{eff}^2)^2 + 4n_m^2 n_{eff}^6 = 0, \tag{5.2.2}$$

where $Q^2 = tan^2 \frac{2\pi d_m n_m}{\lambda}$, and its solution gives $\rho = 1.0033 + 6 \cdot 10^{-6} i$ corresponding to the theoretical propagation length of $\cong \dfrac{\lambda}{2\pi Im\rho} = 17mm$, which is two orders of magnitude larger than the experimentally measured value. Similarly, for gold at $710nm$ and for the thickness of $5nm$, cf. [119], we have $Im\rho \cong 10^{-6}$, for palladium at $739nm$

with $d = 8nm$ and $n_{Pd} = 1.9 + 4.8i$ [121, 127] we have $Im\rho \cong 10^{-5}$, and so forth.

Certainly, for the case of nanofilms, additional damping mechanisms exist and should be taken into account. The most well-known and fundamental one is the collision-induced scattering of conducting electrons at the walls of the nanofilm ("anomalous skin- and size-effects") which has been profoundly discussed starting from the end of the forties (see e.g., [133, 134] and references therein; see also [127]). For our purposes, it is sufficient to present here only the final formula pertinent for the imaginary part of the dielectric constant for a continuous thin film at a frequency ω [134]:

$$\varepsilon'' = \varepsilon''_{bulk} + \frac{3\omega_p^3}{8\omega^3} \cdot \frac{\upsilon_F}{c} \cdot \frac{1 + cosh^2(\omega_p d/c)}{sinh(\omega_p d/c)cosh(\omega_p d/c) + \omega_p d/c} \cdot (1 - p), \quad (5.2.3)$$

where d is nanofilm thickness, ω_p is plasma frequency, υ_F - Fermi velocity and p - the so called "scattering parameter" defined as a fraction of electrons specularly reflected on the walls. (Real part of the dielectric constant is practically non-affected by this same scattering). For a completely diffuse scattering, $p = 0$, Equation 5.2.3 gives the following limit for small thicknesses:

$$\varepsilon'' = \varepsilon''_{bulk} + \frac{3\omega_p^3}{8\omega^3} \cdot \frac{\upsilon_F}{d}, \quad (5.2.4)$$

Taking for estimations for our case of silver nanofilm $\upsilon_F = 1.4 \cdot 10^6 m/s$ [135], $\hbar\omega_p = 9eV$ [136], $d = 12.5nm$ and the frequency corresponding to the $He - Ne$ laser used, we have $\frac{3\omega_p^3}{8\omega^3} \cdot \frac{\upsilon_F}{d} \cong 0.4$. This is non-negligible but still not such a significant change given that $\varepsilon'' = n_{Ag}^2 = -15.87 + 1.07i$, and it results in the new value of an effective refractive index of the "gold in the nanofilm" $n_{film} = \sqrt{\varepsilon''} = 0.1846 + 3.99i$.

Substitution of this value into Equation 5.2.2 instead of $n_{Ag} = 0.1345 + 3.986i$ leads only to a minor change in the dissipation giving $Im\rho \cong 8 \cdot 10^{-6}$. The same conclusion can be drawn applying Equation 5.2.4 for other cases, such as gold and palladium.

This same aforementioned noticeable difference between the experimentally observed and theoretically possible propagation lengths of LRSPP supported by Photonic Crystals should not be considered as surprising, because the ideal matching of the design of the PC and a real structure parameters, as well as ideal quality of all interfaces and materials, are needed (not to mention that in reality we certainly have a finite PC only). In any case, obtained values are already quite impressive and suitable for practical applications. Nevertheless, we should bear in mind that apparently there is still significant room for improvements in this field.

5.3 CONCLUSION

We reported on the first experimental realization of PC - supported LRSPP in thin, $12.5nm$-thick, silver nanofilms. These nanofilms have been deposited onto specially prepared and purpose-optimized for the task $1D$ PC, the design of which included as the most external part a thin ZnS layer earlier proposed as one of the most suitable adjacent layer to make a high-quality silver nanofilm. Another thin ZnS layer has been deposited over this Ag nanofilm, it is in contact with the atmosphere and serves as an indispensable external protective layer. The design of the PC takes into account the necessity of adding this layer, and the structure parameters have been optimized to enable the propagation of surface electromagnetic waves along the combined "thin layer of $ZnS + air$" external media—silver interface. Reasonable long-term stability of the structure has been observed.

The ultranarrow surface plasmon resonance corresponding to the LRSPP propagation length of $180\mu m$ has been recorded. This value is quite large, and enables the practical use of similar structures as sensors, cf. [120–124].

This chapter is mainly based on the following article:

Sekatskii, Sergey, Anton Smirnov, Giovanni Dietler, Nur E. Alam, Mikhail Vasiliev, and Kamal Alameh. "Photonic crystal-supported long-range surface plasmon-polaritons propagating along high-quality silver nanofilms." Applied Sciences 8, no. 2 (2018): 248.

Personal contribution: performed the optical studies of plasmons; writing and discussion.

6

Conclusion

The performance of any SNOM strongly depends on the probe's characteristics. Thus most of the microscopes inherit common problems: the fragility of the tip and the possibility to damage a sample, poor coarse navigation along the sample surface, and limited operation ability in liquids. We explored several ways to enhance SNOM performance.

- Tapping mode SNOM utilizing bent fiber probes. The comprehensive analysis of the probe vibration modes allows the clarifying of conditions essential to realize true efficient tapping mode. (It turned out that most SNOM probes claimed to work in the tapping mode actually do not work in this same mode). Based on the simulations, we prepared such probes and tested them.

Among others, we believe, that the smaller interaction forces between the tip and sample pave the way to operate in liquid. Furthermore, we found that not only SNOM probes, but AFM cantilevers, considered to have exclusively tapping mode dithering, can deviate from this behavior: ultrashort cantilevers encounter shear-force interaction mechanism, which is especially important for the interpretation of Multiple Frequency experiments results.

- SNOM probes made of plastic optical fibers. We realized the first POF SNOM probes with submicron core size and metalized by the shadow coating method. The proven extreme durability of these probes, along with the excellent imaging quality comparable with the performance of classical glass fiber probes, enables to consider them as the "most suitable" probes for SNOM. Furthermore, non-hazardous preparation of these probes greatly facilitates the way of practical applications.

The use of bent POF probe also was considered. Small core size can increase the light transmission efficiency in the bent part. Together with the low weight and small acting forces, this can help to reach an excellent performance.

The central part of the work was devoted to the single molecule FRET SNOM. The numerous efforts to realize such a scheme using NV centers in ND crystals failed. This, together with a number of other recent publications, show that the fluorescence efficiency of this object is quite low, and researchers can not be guided by the results obtained using the fluorescence of bulk diamond samples when exploiting NDs. The quantum yield of NV centers in NDs can be estimated to be $\sim 2\%$ on average, which makes them inappropriate for the FRET SNOM. As an alternative, we proposed and launched the realization of FRET SNOM based on the rare-earth ions in nanocrystals as the fluorescent source.

The current work also includes the study of surface electromagnetic waves propagation along the surface. We reported the realization of the first PC-supported LRSPP in thin silver nanofilms. The structure optimization allows to reach the propagation length of $180\mu m$.

6.1 THE PERSPECTIVE

In the current state SNOM is a powerful and unique technique. The primary concurrent - STED is extremely expensive, cannot link the topography with the optical response and always requires the linkers (dyes). At the same time, SNOM can overcome all these problems and even can study biological objects in alive conditions. However, it is not a popular technique because it is an unforgiving one. Thus it still has a room for the improvement.

In the thesis in hand, we proposed the solution of the main problem: POF probes. It allows to drastically increase the life cycle of probes and make them user-friendly. Now the next step is to put it to mass-production, then it will have the same price as a glass one and also will be able to substitute them for everyday experiments.

Concerning the tapping mode SNOM probes, the situation is complicated: the fiber for this should be bent with careful control of parameters otherwise shear-force will dominate in the oscillation. On the other hand, we realized tapping mode probes, but it seems to be unpractical due to difficulties in coating and huge losses of an optical signal in the bending point.

The realization of stably operating FRET SNOM is still an open question: the photo-stable donor (or acceptor) is yet to be found. The most prominent candidates now are rare-earth ions which have acceptable quantum yield and high photostability.

Another way is to work in liquid (or in other media without the oxygen): thus the standard quantum dots ($CdSe$) could be used and will not be burned due to the absence of strong oxidizers.

Ideally, the SNOM should become a gadget for a standard optical microscope. For example, the condenser can be changed to the SNOM tip. Alternatively, SNOM could have a form a standard micro-objective which can be swapped in seconds.

7

Extra

Chapter 7. Extra

7.1 Appendix A

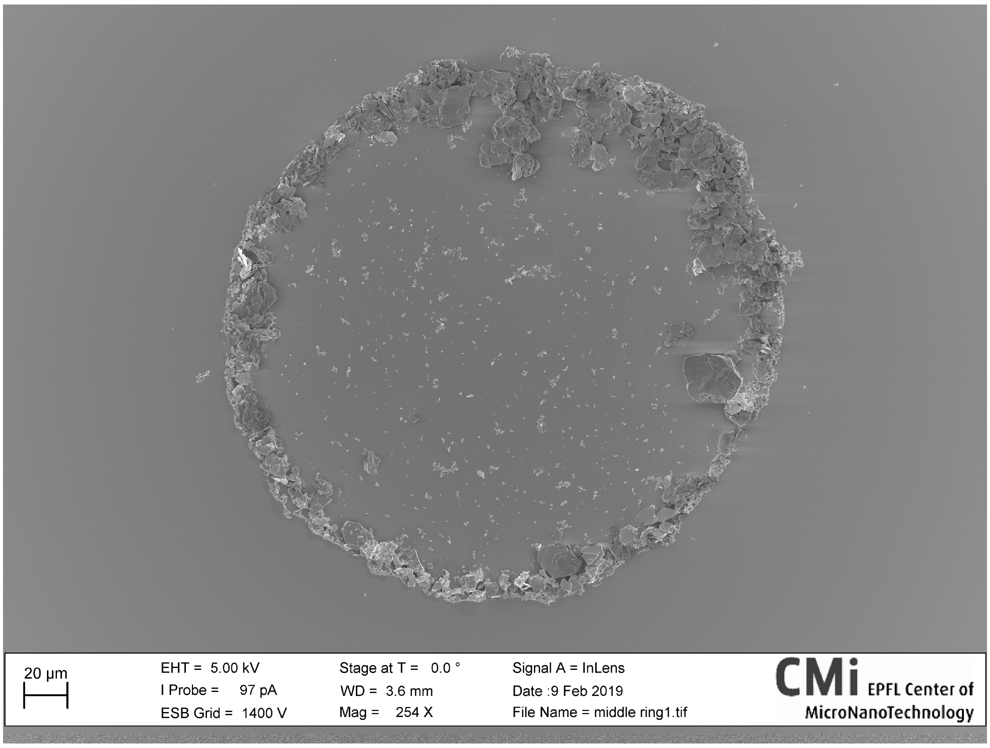

Figure 7.1: The SEM image of $0.1\% \ LuBO_3(Tb)$ drop on the gold substrate dyed on the air. The image demonstrate ”coffee ring” effect caused by a capillary flow.

References

[1] Stefan W. Hell and Jan Wichmann. Breaking the diffraction resolution limit by stimulated emission: Stimulated-emission-depletion fluorescence microscopy. *Optics Letters*, 19(11):780–782, June 1994.

[2] V. A. Okhonin. Method of investigating specimen microstructure. *Patent SU*, 1374992, 1986.

[3] Samuel T. Hess, Thanu P. K. Girirajan, and Michael D. Mason. Ultra-High Resolution Imaging by Fluorescence Photoactivation Localization Microscopy. *Biophysical Journal*, 91(11):4258–4272, December 2006.

[4] Eric Betzig, George H. Patterson, Rachid Sougrat, O. Wolf Lindwasser, Scott Olenych, Juan S. Bonifacino, Michael W. Davidson, Jennifer Lippincott-Schwartz, and Harald F. Hess. Imaging Intracellular Fluorescent Proteins at Nanometer Resolution. *Science*, 313(5793):1642–1645, September 2006.

[5] Michael J. Rust, Mark Bates, and Xiaowei Zhuang. Sub-diffraction-limit imaging by stochastic optical reconstruction microscopy (STORM). *Nature Methods*, 3(10):793–796, October 2006.

[6] E.H. Synge. A suggested method for extending microscopic resolution into the ultra-microscopic region. *The London, Edinburgh, and Dublin Philosophical Magazine and Journal of Science*, 6(35):356–362, August 1928.

[7] E. A. ASH and G. NICHOLLS. Super-resolution Aperture Scanning Microscope. *Nature*, 237(5357):510–512, June 1972.

[8] A. Lewis, M. Isaacson, A. Harootunian, and A. Muray. Development of a 500 Å spatial resolution light microscope: I. light is efficiently transmitted through $\lambda/16$ diameter apertures. *Ultramicroscopy*, 13(3):227–231, January 1984.

[9] Dieter W. Pohl, Winfried Denk, and Mark Lanz. Optical stethoscopy: Image recording with resolution $\lambda/20$. *Applied physics letters*, 44(7):651–653, 1984.

[10] Raymond G. Wilson and Sean M. McCreary. *Fourier Series and Optical Transform Techniques in Contemporary Optics: An Introduction*. John Wiley, May 1995.

[11] Yehuda Leviatan. Study of near-zone fields of a small aperture. *Journal of Applied Physics*, 60(5):1577–1583, September 1986.

[12] D. W. Pohl, U. Ch Fischer, and U. T. Dürig. Scanning near-field optical microscopy (SNOM). *Journal of Microscopy*, 152(3):853–861, December 1988.

[13] E. Betzig, J. K. Trautman, R. Wolfe, E. M. Gyorgy, P. L. Finn, M. H. Kryder, and C.-H. Chang. Near-field magneto-optics and high density data storage. *Applied Physics Letters*, 61(2):142–144, July 1992.

[14] R. Toledo-Crow, P. C. Yang, Y. Chen, and M. Vaez-Iravani. Near-field differential scanning optical microscope with atomic force regulation. *Applied physics letters*, 60(24):2957–2959, 1992.

[15] EPLJS Betzig, P. L. Finn, and J. S. Weiner. Combined shear force and near-field scanning optical microscopy. *Applied physics letters*, 60(20):2484–2486, 1992.

[16] U. Ben-Ami, N. Tessler, N. Ben-Ami, R. Nagar, G. Fish, K. Lieberman, G. Eisenstein, A. Lewis, J. M. Nielsen, and A. Mo/eller-Larsen. Near-infrared contact mode collection near-field optical and normal force microscopy of modulated multiple quantum well lasers. *Applied physics letters*, 68(17):2337–2339, 1996.

[17] KSAR Lieberman, S. Harush, A. Lewis, and R. Kopelman. A light source smaller than the optical wavelength. *Science*, 247(4938):59–61, 1990.

[18] E. Betzig, M. Isaacson, and A. Lewis. Collection mode near-field scanning optical microscopy. *Applied physics letters*, 51(25):2088–2090, 1987.

[19] EJKTDJSRL Betzig, JK Trautman, TD Harris, JS Weiner, and RL Kostelak. Breaking the Diffraction Barrier: Optical Microscopy on a Nanometric Scale. *Science*, 251(5000):1468–1470, 1991.

[20] GA Valaskovic, M Holton, and GH Morrison. Parameter Control, Characterization, and Optimization in the Fabrication of Optical Fiber near-Field Probes. *Applied optics*, 34(7):1215–1228, 1995.

[21] Dennis R. Turner. Etch Procedure for Optical Fibers, September 1984. U.S. Patent 4,469,554.

[22] H Muramatsu, K Homma, N Chiba, N Yamamoto, and A Egawa. Dynamic Etching Method for Fabricating a Variety of Tip Shapes in the Optical Fibre Probe of a Scanning Near-field Optical Microscope. *Journal of microscopy*, 194(2-3):383–387, 1999.

[23] PT Squire. Axisymmetric Meniscus Formation: A Viscous-Fluid Model for Cones. *Journal of Fluid Mechanics*, 129:91–108, 1983.

[24] Raoul Stöckle, Christian Fokas, Volker Deckert, Renato Zenobi, Beate Sick, Bert Hecht, and Urs P. Wild. High-quality near-field optical probes by tube etching. *Applied Physics Letters*, 75(2):160–162, 1999.

[25] Khaled Karrai and Robert D Grober. Piezo-electric tuning fork tip—sample distance control for near field optical microscopes. *Ultramicroscopy*, 61(1-4):197–205, 1995.

[26] D. A. Lapshin, V. S. Letokhov, G. T. Shubeita, S. K. Sekatskii, and G. Dietler. Direct measurement of the absolute value of the interaction force between the fiber probe and the sample in a scanning near-field optical microscope. *Applied Physics Letters*, 81(8):1503–1505, August 2002.

[27] D. V. Serebryakov, S. K. Sekatskii, A. P. Cherkun, K. Dukenbayev, I. V. Morozov, V. S. Letokhov, and G. Dietler. Scanning near-field optical microscope based on a double resonant fibre probe montage and equipped with time-gated photon detection. *Journal of Microscopy*, 229(2):287–292, 2008.

[28] A. P. Cherkun, D. V. Serebryakov, S. K. Sekatskii, I. V. Morozov, and V. S. Letokhov. Double-resonance probe for near-field scanning optical microscopy. *Review of scientific instruments*, 77(3):033703, 2006.

[29] Joseph R. Lakowicz. *Principles of Fluorescence Spectroscopy*. Springer US, 3 edition, 2006.

[30] S. K. Sekatskii, G. Dietler, and V. S. Letokhov. Single molecule fluorescence resonance energy transfer scanning near-field optical microscopy. *Chemical Physics Letters*, 452(1):220–224, February 2008.

[31] S. K. Sekatskii and V. S. Letokhov. Single fluorescence centers on the tips of crystal needles: First observation and prospects for application in scanning one-atom fluorescence microscopy. *Applied Physics B*, 63(5):525–530, November 1996.

[32] Vladimir Moiseevich Agranovich and Michail Dmitrievič Galanin. *Electronic Excitation Energy Transfer in Condensed Matter*, volume 3. North-Holland, 1982.

[33] R. M. Clegg. Fluorescence resonance energy transfer. *Fluorescence imaging spectroscopy and microscopy*, 137:179–251, 1996.

[34] Elizabeth A. Jares-Erijman and Thomas M. Jovin. FRET imaging. *Nature biotechnology*, 21(11):1387, 2003.

[35] Robert C Dunn. Near-Field Scanning Optical Microscopy. *Chemical reviews*, 99(10):2891–2928, 1999.

[36] Motoichi Ohtsu. *Near-Field Nano/Atom Optics and Technology*. Springer Science & Business Media, 2012.

[37] L. Novotny and B. Hecht. *Principles of Nano-Optics Cambridge Univ*. Press, 2006.

[38] Sarah A. Vickery and Robert C. Dunn. Scanning near-field fluorescence resonance energy transfer microscopy. *Biophysical journal*, 76(4):1812–1818, 1999.

[39] G. T. Shubeita, S. K. Sekatskii, M. Chergui, G. Dietler, and V. S. Letokhov. Investigation of nanolocal fluorescence resonance energy transfer for scanning probe microscopy. *Applied physics letters*, 74(23):3453–3455, 1999.

[40] S. A. Vickery and R. C. Dunn. Combining AFM and FRET for high resolution fluorescence microscopy. *Journal of microscopy*, 202(2):408–412, 2001.

[41] G. T. Shubeita, S. K. Sekatskii, G. Dietler, and V. S. Letokhov. Local fluorescent probes for the fluorescence resonance energy transfer scanning near-field optical microscopy. *Applied physics letters*, 80(15):2625–2627, 2002.

[42] G. T. Shubeita, S. K. Sekatskii, G. Dietler, I. Potapova, A. Mews, and Th Basché. Scanning near-field optical microscopy using semiconductor nanocrystals as a local fluorescence and fluorescence resonance energy transfer source. *Journal of microscopy*, 210(3):274–278, 2003.

[43] Y. Ebenstein, T. Mokari, and U. Banin. Quantum-dot-functionalized scanning probes for fluorescence-energy-transfer-based microscopy. *The Journal of Physical Chemistry B*, 108(1):93–99, 2004.

[44] Felix Müller, Stephan Götzinger, Nikolai Gaponik, Horst Weller, Jürgen Mlynek, and Oliver Benson. Investigation of energy transfer between CdTe nanocrystals on polystyrene beads and dye molecules for FRET-SNOM applications. *The Journal of Physical Chemistry B*, 108(38):14527–14534, 2004.

[45] S. K. Sekatskii, G. Dietler, F. Bonfigli, S. Loreti, T. Marolo, and R. M. Montereali. Subwavelength-size local fluorescent sources based on color centers in LiF for scanning near-field optical microscopy. *Journal of Luminescence*, 122-123:362–364, January 2007.

[46] Romana Schirhagl, Kevin Chang, Michael Loretz, and Christian L. Degen. Nitrogen-Vacancy Centers in Diamond: Nanoscale Sensors for Physics and Biology. *Annual Review of Physical Chemistry*, 65(1):83–105, April 2014.

[47] I. Aharonovich, S. Castelletto, D. A. Simpson, C.-H. Su, A. D. Greentree, and S. Prawer. Diamond-based single-photon emitters. *Reports on Progress in Physics*, 74(7):076501, June 2011.

[48] F. Jelezko and J. Wrachtrup. Single defect centres in diamond: A review. *physica status solidi (a)*, 203(13):3207–3225, 2006.

[49] Sébastien Pezzagna, Detlef Rogalla, Dominik Wildanger, Jan Meijer, and Alexander Zaitsev. Creation and nature of optical centres in diamond for single-photon emission—overview and critical remarks. *New Journal of Physics*, 13(3):035024, 2011.

[50] S. Z. Shmurak, V. V. Kedrov, A. P. Kiselev, T. N. Fursova, and O. G. Rybchenko. Spectral and structural characteristics of Lu 1−x−y Ce x Tb y BO 3 orthoborates prepared by the hydrothermal synthesis method. *Physics of the Solid State*, 59(6):1171–1182, 2017.

[51] S. Kühn, C. Hettich, C. Schmitt, J.-Ph Poizat, and Vahid Sandoghdar. Diamond colour centres as a nanoscopic light source for scanning near-field optical microscopy. *Journal of Microscopy*, 202(1):2–6, 2001.

[52] Eva Rittweger, Kyu Young Han, Scott E. Irvine, Christian Eggeling, and Stefan W. Hell. STED microscopy reveals crystal colour centres with nanometric resolution. *Nature Photonics*, 3(3):144, 2009.

[53] Silvia Arroyo-Camejo, Marie-Pierre Adam, Mondher Besbes, Jean-Paul Hugonin, Vincent Jacques, Jean-Jacques Greffet, Jean-François Roch, Stefan W. Hell, and François Treussart. Stimulated emission depletion microscopy resolves individual nitrogen vacancy centers in diamond nanocrystals. *ACS nano*, 7(12):10912–10919, 2013.

[54] T. Gaebel, M. Domhan, C. Wittmann, I. Popa, F. Jelezko, J. Rabeau, A. Greentree, S. Prawer, E. Trajkov, and Philip R. Hemmer. Photochromism in single nitrogen-vacancy defect in diamond. *Applied Physics B*, 82(2):243–246, 2006.

[55] Konstantin Iakoubovskii, G. J. Adriaenssens, and Milos Nesladek. Photochromism of vacancy-related centres in diamond. *Journal of Physics: Condensed Matter*, 12(2):189, 2000.

[56] Ulrich Brackmann. Lambdachrome. *Laser-grade dyes, data sheets. 2nd revised edition. Lambda Physik GmbH, Gottingen, Germany*, 1997.

[57] Charles Santori, Paul E. Barclay, Kai-Mei C. Fu, and Raymond G. Beausoleil. Vertical distribution of nitrogen-vacancy centers in diamond formed by ion implantation and annealing. *Physical Review B*, 79(12):125313, 2009.

[58] L. Rondin, G. Dantelle, A. Slablab, F. Grosshans, F. Treussart, P. Bergonzo, S. Perruchas, T. Gacoin, M. Chaigneau, H.-C. Chang, V. Jacques, and J.-F. Roch. Surface-induced charge state conversion of nitrogen-vacancy defects in nanodiamonds. *Physical Review B*, 82(11):115449, September 2010.

[59] K. Ohashi, T. Rosskopf, H. Watanabe, M. Loretz, Y. Tao, R. Hauert, S. Tomizawa, T. Ishikawa, J. Ishi-Hayase, and S. Shikata. Negatively charged nitrogen-vacancy centers in a 5 nm thin 12C diamond film. *Nano letters*, 13(10):4733–4738, 2013.

[60] Moloud Kaviani, Peter Deák, Bálint Aradi, Thomas Frauenheim, Jyh-Pin Chou, and Adam Gali. Proper surface termination for luminescent near-surface NV centers in diamond. *Nano letters*, 14(8):4772–4777, 2014.

[61] G. Dantelle, A. Slablab, L. Rondin, F. Lainé, F. Carrel, Ph Bergonzo, S. Perruchas, T. Gacoin, F. Treussart, and J.-F. Roch. Efficient production of NV colour centres in nanodiamonds using high-energy electron irradiation. *Journal of Luminescence*, 130(9):1655–1658, 2010.

[62] Alexios Beveratos, Rosa Brouri, Thierry Gacoin, Jean-Philippe Poizat, and Philippe Grangier. Nonclassical radiation from diamond nanocrystals. *Physical Review A*, 64(6):061802, 2001.

[63] A. Gruber, A. Dräbenstedt, C. Tietz, L. Fleury, J. Wrachtrup, and C. Von Borczyskowski. Scanning confocal optical microscopy and magnetic resonance on single defect centers. *Science*, 276(5321):2012–2014, 1997.

[64] Tse-Luen Wee, Yan-Kai Tzeng, Chau-Chung Han, Huan-Cheng Chang, Wunshain Fann, Jui-Hung Hsu, Kuan-Ming Chen, and Yueh-Chung Yu. Two-photon excited fluorescence of nitrogen-vacancy centers in proton-irradiated type Ib diamond. *The Journal of Physical Chemistry A*, 111(38):9379–9386, 2007.

[65] Gordon Davies and M. F. Hamer. Optical studies of the 1.945 eV vibronic band in diamond. *Proc. R. Soc. Lond. A*, 348(1653):285–298, 1976.

[66] Taras Plakhotnik and Haroon Aman. NV-centers in nanodiamonds: How good they are. *Diamond and Related Materials*, 82:87–95, 2018.

[67] Alexey Vervald, Sergey Burikov, Nataliya Borisova, Igor Vlasov, Kirill Laptinskiy, Tatiana Laptinskaya, Olga Shenderova, and Tatiana Dolenko. Fluorescence properties of nanodiamonds with NV centers in water suspensions. *physica status solidi (a)*, 213(10):2601–2607, 2016.

[68] Carlo Bradac, Torsten Gaebel, Chris I. Pakes, Jana M. Say, Andrei V. Zvyagin, and James R. Rabeau. Effect of the Nanodiamond Host on a Nitrogen-Vacancy Color-Centre Emission State. *Small*, 9(1):132–139, 2013.

[69] Yi-Ying Chen, Hualin Shu, Yung Kuo, Yan-Kai Tzeng, and Huan-Chang Chang. Measuring Förster resonance energy transfer between fluorescent nanodiamonds and near-infrared dyes by acceptor photobleaching. *Diamond and Related Materials*, 20(5-6):803–807, 2011.

[70] Yi-Ren Chang, Hsu-Yang Lee, Kowa Chen, Chun-Chieh Chang, Dung-Sheng Tsai, Chi-Cheng Fu, Tsong-Shin Lim, Yan-Kai Tzeng, Chia-Yi Fang, and Chau-Chung Han. Mass production and dynamic imaging of fluorescent nanodiamonds. *Nature nanotechnology*, 3(5):284, 2008.

[71] A. Drezet, Y. Sonnefraud, Aurélien Cuche, O. Mollet, M. Berthel, and S. Huant. Near-field microscopy with a scanning nitrogen-vacancy color center in a diamond nanocrystal: A brief review. *Micron*, 70:55–63, 2015.

[72] Aurélien Cuche, Aurélien Drezet, Yannick Sonnefraud, Orestis Faklaris, François Treussart, Jean-François Roch, and Serge Huant. Near-field optical microscopy with a nanodiamond-based single-photon tip. *Optics express*, 17(22):19969–19980, 2009.

[73] Igor Aharonovich, Stefania Castelletto, David A. Simpson, Alastair Stacey, Jeff McCallum, Andrew D. Greentree, and Steven Prawer. Two-level ultrabright single photon emission from diamond nanocrystals. *Nano letters*, 9(9):3191–3195, 2009.

[74] Igor I. Vlasov, Andrey A. Shiryaev, Torsten Rendler, Steffen Steinert, Sang-Yun Lee, Denis Antonov, Márton Vörös, Fedor Jelezko, Anatolii V. Fisenko, Lubov F. Semjonova, Johannes Biskupek, Ute Kaiser, Oleg I. Lebedev, Ilmo Sildos, Philip R. Hemmer, Vitaly I. Konov, Adam Gali, and Jörg Wrachtrup. Molecular-sized fluorescent nanodiamonds. *Nature Nanotechnology*, 9(1):54–58, January 2014.

[75] A. S. Barnard, I. I. Vlasov, and V. G. Ralchenko. Predicting the distribution and stability of photoactive defect centers in nanodiamond biomarkers. *Journal of Materials Chemistry*, 19(3):360–365, 2009.

[76] Yury Deshko and Anshel Gorokhovsky. Effects of planar geometry on the inhomogeneous broadening of zero-phonon lines of optical centers in diamond. *physica status solidi (b)*, 250(2):278–282, 2013.

[77] G. Liu. *B. Jacquier (Editor)„Spectroscopic Properties of Rare Earths in Optical Materials"*. Springer Series in Materials Sciences and Tsinghua University Press, Beijing, 2005.

[78] Philippe Goldner, Alban Ferrier, and Olivier Guillot-Noël. Rare earth-doped crystals for quantum information processing. In *Handbook on the Physics and Chemistry of Rare Earths*, volume 46, pages 1–78. Elsevier, 2015.

[79] C. W. Thiel, Thomas Böttger, and R. L. Cone. Rare-earth-doped materials for applications in quantum information storage and signal processing. *Journal of luminescence*, 131(3):353–361, 2011.

[80] T. T. Basiev, I. T. Basieva, A. A. Kornienko, V. V. Osiko, K. K. Pukhov, and S. K. Sekatskii. Pre-selection of optical transitions in rare-earth ions in crystals perspective for quantum information processing. *Journal of Modern Optics*, 59(2):166–178, 2012.

[81] SZ Shmurak, VV Kedrov, AP Kiselev, TN Fursova, and IM Shmyt'ko. Spectral and structural features of Lu1- xRExBO3 compounds. *Physics of the Solid State*, 57(8):1588–1600, 2015.

[82] SZ Shmurak, VV Kedrov, AP Kiselev, TN Fursova, and IM Smyt'ko. Spectral characteristics and energy transfer from Ce 3+ to Tb 3+ in compounds Lu 1–x–y Ce x Tb y BO 3. *Physics of the Solid State*, 58(3):578–591, 2016.

[83] Jun Yang, Cuimiao Zhang, Lili Wang, Zhiyao Hou, Shanshan Huang, Hongzhou Lian, and Jun Lin. Hydrothermal synthesis and luminescent properties of LuBO3: Tb3+ microflowers. *Journal of Solid State Chemistry*, 181(10):2672–2680, 2008.

[84] Christelle Mansuy, Jean-Marie Nedelec, Christophe Dujardin, and Rachid Mahiou. Concentration effect on the scintillation properties of sol–gel derived LuBO3 doped with Eu3+ and Tb3+. *Optical Materials*, 29(6):697–702, 2007.

[85] F. Moreno-Herrero, P. J. de Pablo, J. Colchero, J. Gómez-Herrero, and A. M. Baró. The role of shear forces in scanning force microscopy: A comparison between the jumping mode and tapping mode. *Surface Science*, 453(1):152–158, May 2000.

[86] J. P. Ndobo-Epoy, E. Lesniewska, and J. P. Guicquero. Shear force microscopy with a nanoscale resolution. *Ultramicroscopy*, 103(3):229–236, June 2005.

[87] Igor I. Smolyaninov, Walid A. Atia, Saeed Pilevar, and Christopher C. Davis. Experimental study of probe–surface interaction in near-field optical microscopy. *Ultramicroscopy*, 71(1):177–182, March 1998.

[88] M. J. Gregor, P. G. Blome, J. Schöfer, and R. G. Ulbrich. Probe-surface interaction in near-field optical microscopy: The nonlinear bending force mechanism. *Applied Physics Letters*, 68(3):307–309, January 1996.

[89] Hiroshi Muramatsu, Norio Chiba, Katsunori Homma, Kunio Nakajima, Tatsuaki Ataka, Satoko Ohta, Akihiro Kusumi, and Masamichi Fujihira. Near-field optical microscopy in liquids. *Applied Physics Letters*, 66(24):3245–3247, June 1995.

[90] Hiroshi Muramatsu, Norio Chiba, and Masamichi Fujihira. Frictional imaging in a scanning near-field optical/atomic-force microscope by a thin step etched optical fiber probe. *Applied Physics Letters*, 71(15):2061–2063, October 1997.

[91] Din Ping Tsai and Wen Kai Li. Optical fiber structures studied by a tapping-mode scanning near-field optical microscope. *Journal of Vacuum Science & Technology A*, 15(3):1427–1431, May 1997.

[92] N. H. Lu, C. W. Huang, C. Y. Chen, C. F. Yu, T. S. Kao, Y. H. Fu, and D. P. Tsai. Implementation of a short-tip tapping-mode tuning fork near-field scanning optical microscope. *Journal of Microscopy*, 209(3):205–208, 2003.

[93] D. A. Lapshin, V. N. Reshetov, S. K. Sekatskii, and V. S. Letokhov. Contact mode near-field microscope. *Ultramicroscopy*, 76(1):13–20, February 1999.

[94] Sangjin Kwon, Sungho Jeong, and Yongseok Kang. Topography and near-field image measurement of soft biological samples in liquid by using a tuning fork based bent optical-fiber sensor. *Review of Scientific Instruments*, 82(4):043707, April 2011.

[95] F. H. Lei, L. Huang, O. Piot, A. Trussardi, M. Manfait, G. Shang, and M. Troyon. Active bimorph-based tapping-mode distance control for scanning near-field optical microscopy of biological samples in liquid. *Journal of Applied Physics*, 100(8):084317, October 2006.

[96] Mechanical User's Guide,. *ANSYS® Academic Research*, Help System.

[97] Edward B. Magrab. *Vibrations of Elastic Systems*, volume 184 of *Solid Mechanics and Its Applications*. Springer, Dordrecht, 2012.

[98] William F Stokey. Vibration of systems having distributed mass and elasticity. *Shock and vibration Handbook*, pages 7–1, 1988.

[99] VF Dryakhlushin, A Yu Klimov, VV Rogov, and SA Gusev. A Probe for Scanning Near-Field Optical Microscope. *Devices and Technique of Experiment*, 2:138–139, 1998.

[100] A. Naber, H.-J. Maas, K. Razavi, and U. C. Fischer. Dynamic force distance control suited to various probes for scanning near-field optical microscopy. *Review of Scientific Instruments*, 70(10):3955–3961, September 1999.

[101] H Chibani, K Dukenbayev, M Mensi, SK Sekatskii, and G Dietler. Near-Field Scanning Optical Microscopy Using Polymethylmethacrylate Optical Fiber Probes. *Ultramicroscopy*, 110(3):211–215, 2010.

[102] L. Novotny and C. Hafner. Light propagation in a cylindrical waveguide with a complex, metallic, dielectric function. *Physical Review E*, 50(5):4094–4106, November 1994.

[103] Allan W. Snyder and John Love. *Optical Waveguide Theory*. Springer Science & Business Media, 2012.

[104] Masahiro Yamazaki. Industrialization and application development of cyclo-olefin polymer. *Journal of Molecular Catalysis A: Chemical*, 213(1):81–87, 2004.

[105] Kazuyuki Obuchi, Masaaki Komatsu, and Koji Minami. High performance optical materials cyclo olefin polymer ZEONEX. In *Optical Manufacturing and Testing VII*, volume 6671, page 66711I. International Society for Optics and Photonics, 2007.

[106] Jozef Adamcik, Dmitry V. Klinov, Guillaume Witz, Sergey K. Sekatskii, and Giovanni Dietler. Observation of single-stranded DNA on mica and highly oriented pyrolytic graphite by atomic force microscopy. *FEBS Letters*, 580(24):5671–5675, 2006.

[107] Jozef Adamcik, Jin-Mi Jung, Jérôme Flakowski, Paolo De Los Rios, Giovanni Dietler, and Raffaele Mezzenga. Understanding Amyloid Aggregation by Statistical Analysis of Atomic Force Microscopy Images. *Nature nanotechnology*, 5(6):423, 2010.

[108] Francesco Simone Ruggeri, Jozef Adamcik, Jae Sun Jeong, Hilal A Lashuel, Raffaele Mezzenga, and Giovanni Dietler. Influence of the B-Sheet Content on the Mechanical Properties of Aggregates during Amyloid Fibrillization. *Angewandte Chemie International Edition*, 54(8):2462–2466, 2015.

[109] Zhaogang Dong, Ying Zhang, Shaw Wei Kok, Boon Ping Ng, and Yeng Chai Soh. Artifact reduction by intrinsic harmonics of tuning fork probe for scanning

near-field optical microscopy. *Optics Express*, 18(21):22047–22060, October 2010.

[110] WM Robertson and MS May. Surface electromagnetic wave excitation on one-dimensional photonic band-gap arrays. *Applied physics letters*, 74(13):1800–1802, 1999.

[111] Valery N Konopsky and Elena V Alieva. Photonic crystal surface waves for optical biosensors. *Analytical chemistry*, 79(12):4729–4735, 2007.

[112] Valery N Konopsky, Tanya Karakouz, Elena V Alieva, Chiara Vicario, Sergey K Sekatskii, and Giovanni Dietler. Photonic crystal biosensor based on optical surface waves. *Sensors*, 13(2):2566–2578, 2013.

[113] Francesca Frascella, Serena Ricciardi, Paola Rivolo, Valeria Moi, Fabrizio Giorgis, Emiliano Descrovi, Francesco Michelotti, Peter Munzert, Norbert Danz, and Lucia Napione. A fluorescent one-dimensional photonic crystal for label-free biosensing based on Bloch surface waves. *Sensors*, 13(2):2011–2022, 2013.

[114] Angelo Angelini, Elsie Barakat, Peter Munzert, Luca Boarino, Natascia De Leo, Emanuele Enrico, Fabrizio Giorgis, Hans Peter Herzig, Candido Fabrizio Pirri, and Emiliano Descrovi. Focusing and extraction of light mediated by Bloch surface waves. *Scientific reports*, 4:5428, 2014.

[115] Tatiana Kovalevich, Abdoulaye Ndao, Miguel Suarez, Saulius Tumenas, Zigmas Balevicius, Arunas Ramanavicius, Ieva Baleviciute, Markus Häyrinen, Matthieu Roussey, and Markku Kuittinen. Tunable Bloch surface waves in anisotropic photonic crystals based on lithium niobate thin films. *Optics letters*, 41(23):5616–5619, 2016.

[116] Ekaterina Rostova, Carine Ben Adiba, Giovanni Dietler, and Sergey K. Sekatskii. Kinetics of Antibody Binding to Membranes of Living Bacteria Measured by a Photonic Crystal-Based Biosensor. *Biosensors*, 6(4), October 2016.

[117] Tatiana Kovalevich, Djaffar Belharet, Laurent Robert, Myun-Sik Kim, Hans Peter Herzig, Thierry Grosjean, and Maria-Pilar Bernal. Experimental evidence of Bloch surface waves on photonic crystals with thin-film LiNbO 3 as a top layer. *Photonics Research*, 5(6):649–653, 2017.

[118] Richa Dubey, B Vosoughi Lahijani, Elsie Barakat, M Häyrinen, M Roussey, M Kuittinen, and Hans Peter Herzig. Near-field characterization of a Bloch-surface-wave-based 2D disk resonator. *Optics letters*, 41(21):4867–4870, 2016.

[119] Valery N Konopsky and Elena V Alieva. Long-range propagation of plasmon polaritons in a thin metal film on a one-dimensional photonic crystal surface. *Physical review letters*, 97(25):253904, 2006.

[120] Valery N Konopsky, Dmitry V Basmanov, Elena V Alieva, Sergey K Sekatskii, and Giovanni Dietler. Size-dependent hydrogen uptake behavior of Pd nanoparticles revealed by photonic crystal surface waves. *Applied Physics Letters*, 100(8):083108, 2012.

[121] Valery N Konopsky, Dmitry V Basmanov, Elena V Alieva, Dmitry I Dolgy, Eugeny D Olshansky, Sergey K Sekatskii, and Giovanni Dietler. Registration of long-range surface plasmon resonance by angle-scanning feedback and its implementation for optical hydrogen sensing. *New Journal of Physics*, 11(6):063049, 2009.

[122] SM Hamidi, R Ramezani, and A Bananej. Hydrogen gas sensor based on long-range surface plasmons in lossy palladium film placed on photonic crystal stack. *Optical Materials*, 53:201–208, 2016.

[123] Daria O Ignatyeva, Grigory A Knyazev, Pavel O Kapralov, Giovanni Dietler, Sergey K Sekatskii, and Vladimir I Belotelov. Magneto-optical plasmonic heterostructure with ultranarrow resonance for sensing applications. *Scientific reports*, 6:28077, 2016.

[124] EV Alieva, VN Konopsky, DV Basmanov, SK Sekatskii, and G Dietler. Blue surface plasmon propagation along thin gold film–gas interface and its use for sensitive nitrogen dioxide detection. *Optics Communications*, 309:148–152, 2013.

[125] JC Quail, JG Rako, and HJ Simon. Long-range surface-plasmon modes in silver and aluminum films. *Optics letters*, 8(7):377–379, 1983.

[126] P Berini, R Charbonneau, N Lahoud, and G Mattiussi. Characterization of long-range surface-plasmon-polariton waveguides. *Journal of Applied Physics*, 98(4):043109, 2005.

[127] Valery N Konopsky. Plasmon-polariton waves in nanofilms on one-dimensional photonic crystal surfaces. *New Journal of Physics*, 12(9):093006, 2010.

[128] H Raether. Surface plasmons on rough and smooth surfaces and on gratings. 1998.

[129] Edward D Palik. *Handbook of Optical Constants of Solids, Five-Volume Set: Handbook of Thermo-Optic Coefficients of Optical Materials with Applications*. Elsevier, 1997.

[130] Dror Sarid. Long-Range Surface-Plasma Waves on Very Thin Metal Films. *Physical Review Letters*, 47(26):1927–1930, December 1981.

[131] Alan E. Craig, Grieg A. Olson, and Dror Sarid. Experimental observation of the long-range surface-plasmon polariton. *Optics Letters*, 8(7):380–382, July 1983.

[132] J. J. Burke, G. I. Stegeman, and T. Tamir. Surface-polariton-like waves guided by thin, lossy metal films. *Physical Review B*, 33(8):5186–5201, April 1986.

[133] RB Dingle. The anomalous skin effect and the reflectivity of metals I. *Physica*, 19(1-12):311–347, 1953.

[134] Marie-Luce Thèye. Investigation of the optical properties of Au by means of thin semitransparent films. *Physical Review B*, 2(8):3060, 1970.

[135] Neil W Ashcroft and N David Mermin. Solid state physics [by] Neil W. Ashcroft [and] N. David Mermin. 1976.

[136] MA Ordal, LL Long, RJ Bell, SE Bell, RR Bell, RW Alexander, and CA Ward. Optical properties of the metals al, co, cu, au, fe, pb, ni, pd, pt, ag, ti, and w in the infrared and far infrared. *Applied optics*, 22(7):1099–1119, 1983.

Anton Smirnov

Doctoral Assistant

@ asmirnov@mm.st
☎ +41 798822940
🌐 https://www.linkedin.com/in/smirnovanton/

Key skills

• AFM • SNOM • STM • SEM • LEED • CVD • FIB • UHV • Microscopy • Optics • Engineering • Lithography • Laser spectroscopy • Free-space optics • ANSYS • SOLIDWORKS • Matlab • CAD • Origin • Gwyddion • LabVIEW • C++

Language

• English • Russian • French

Education

2015-04 - present
PhD in Physics — EPFL (Ecole polytechnique federale de Lausanne)
Graduating in May 2019

2009-09 - 2014-06
MS — Lomonosov Moscow State University

- Graduated with specialization in solid-state physics
- GPA 4.5 out of 5.0

Experience

2015-04 - present
Doctoral Assistant — EPFL (Ecole polytechnique federale de Lausanne)

- Extensive experience in surface analysis techniques: AFM, SNOM, STM, SEM, LEED, XPS/UPS, optical microscopy, single molecule FRET SNOM
- The repairing, building, testing, and tuning of different optical setups including fiber optics and lasers systems.
- Mechanical design (using CAD: SolidWorks) of devices: heads for the scanning probe microscopes, the rotation system for samples in the chamber of the metal sputtering machine, setup for the fibers etching.
- Vibration analysis (ANSYS)
- Simulation of dispersion of photonic crystal structures (Matlab)
- Engineering of scanning systems for microscopes.
- Software development for the operation of the atomic force microscope
- Experience in clean-room (class 100) SEM/FIB/CVD (operating in an ultra-high vacuum (UHV)), knowledge of lithography process
- Development of polymer fiber tips for microscope

2015-04 - present
Teaching Assistant — EPFL (Ecole polytechnique federale de Lausanne)
Assistance in conducting seminars on general physics for 2nd year bachelor students

2014-08 - 2015-04
Junior Scientist — Institute of Solid State Physics RAS

- Image processing
- Software development: GUI (C++) for current-voltage characteristic analysis and acquisition from a source meter

2012-09 - 2014-06
Junior Scientist — Institute of Solid State Physics RAS

- Extensive experience in surface analysis techniques: AFM, STM, LEED, XPS/UPS
- Experience in surface modification techniques: AFM, ion etching
- Mechanical design (using CAD) of low-temperature scanning tunneling microscope (STM) for UHV
- Engineering of vertical scanning system for the low-temperature UHV STM

2010-02 - 2012-06
Research Assistant — Institute of Solid State Physics RAS

- Microscopy hands-on
- Assembling, repairing and tuning of the Scanning Near-Field Microscope operating at a 4K temperature

Anton Smirnov

Doctoral Assistant

@ asmirnov@mm.st

☎ +41 798822940

🌐 https://www.linkedin.com
/in/smirnovanton/

Key skills

• AFM • SNOM • STM • SEM • LEED • CVD • FIB • UHV • Microscopy • Optics • Engineering • Lithography • Laser spectroscopy • Free-space optics • ANSYS • SOLIDWORKS • Matlab • CAD • Origin • Gwyddion • LabVIEW • C++

Language

• English • Russian • French

Publications

2019	Dukenbayev, K.; Smirnov, A.; Tosi, D.; Dietler, G.; Sekatskii, S. K. Chemically Etched Plastic Optical Fiber Probe for Near-Field Scanning Optical Microscopy in Liquids; *International Society for Optics and Photonics, 2019; Vol. 10881, p 108811U*
2019	Chekmazov, S.V., Smirnov, A., Ksenz, A.S., Bozhko, S.I., Ionov, A.M., Protasova, S.G., Kapustin, A.A., Vilkov, O.Y. and Levchenko, E.A., Nontrivial evolution of the Sb(111) electronic and atomic structure after ion irradiation, *Materials Letters 240, 69-72*
2018	Smirnov, A., Rostova, E., Dietler, G. and Sekatskii, S., 2018, Long-life plastic optical fiber probes for scanning near-field optical microscope, *Biomedical Imaging and Sensing Conference 10711, 107110P*
2018	Smirnov, A., Yasinskii, V.M., Filimonenko, D.S., Rostova, E., Dietler, G. and Sekatskii, S.K., True Tapping Mode Scanning Near-Field Optical Microscopy with Bent Glass Fiber Probes, *Scanning 2018*
2018	Sekatskii, S.K., Smirnov, A., Dietler, G., Nur E Alam, M., Vasiliev, M. and Alameh, K., Photonic Crystal-Supported Long-Range Surface Plasmon-Polaritons Propagating Along High-Quality Silver Nanofilms, *Applied Sciences 8 (2), 248*
2015	Chekmazov, S.V., Bozhko, S.I., Smirnov, A., Ionov, A.M. and Kapustin, A.A., STM/STS study of the Sb (111) surface, *Physics Procedia 71, 323-326*
2015	Smirnov, A., Bozhko, S.I., Ionov, A.M., Protasova, S.G., Chekmazov, S.V. and Kapustin, A.A., Sb (111) abnormal behavior under ion etching, *Physics Procedia 71, 327-331*
2015	Sekatskii, S.K., Dukenbayev, K., Mensi, M., Mikhaylov, A.G., Rostova, E., Smirnov, A., Suriyamurthy, N. and Dietler, G., Single molecule fluorescence resonance energy transfer scanning near-field optical microscopy: Potentials and challenges, *Faraday discussions 184, 51-69*

Ce document a été imprimé au Centre d’impression EPFL,
imprimerie climatiquement neutre, certifiée myClimate.